Epitaxial Growth of Wide Bandgap Compound Semiconductors for Laser Diodes

Ayumu Tsujimura

2012

Epitaxial Growth of Wide Bandgap Compound Semiconductors for Laser Diodes

Ayumu Tsujimura

2012

Contents

General Introduction

Many researches have been done on high-brightness violet, blue and green light-emitting diodes (LEDs) and laser diodes (LDs) for use in full-color displays, light sources for lamps, laser printers, read-write laser sources for high-density optical storage, and sources for undersea optical communications with the characteristics of high efficiency, high reliability and high speed. For these purposes, as shown in Fig. 1, group II-VI compound semiconductors such as ZnSe [1,2], III-nitrides such as GaN [3], and group IV compound semiconductor such as SiC [4] have been investigated intensively for a long time. However, it was impossible to obtain high-brightness blue LEDs with a brightness of over 1 cd and reliable LDs.

The efforts to develop blue-green visible light-emitting devices based on the II-VI compounds commenced at the same time as the longer wavelength III-V devices. While solutions to the materials problems encountered in the development of III-V based optoelectronic devices were found, major barriers emerged early with the II-VI compounds. The problems with the II-VIs could be broadly defined in terms of material quality originating from the intrinsic physical make-up (primarily the strong ionicity) of wide bandgap semiconductors.

In the early 1980s a small number of research efforts were begun to apply the modern non-equilibrium epitaxial growth methods, such as molecular beam epitaxy (MBE), to the synthesis of II-VI compound semiconductors and their heterostructures [5]. The initiation of the epitaxial growth efforts were motivated by several considerations: (a) to provide the II-VI compounds with the reduced-dimensional optoelectronic features associated with the fabrication of quantum-sized heterostructures in the III-V compounds, (b) in an attempt to circumvent the traditional doping problems [6-8] and defect generation/compensation which had plagued the more conventional equilibrium growth techniques for bulk crystals, and (c) to fabricate II-VI device structures in the planar configurations which are compatible with modern semiconductor device technology. By the end of the decade, substantial progress had been made in research on II-VI multilayer structures such as quantum wells and superlattices, including demonstrations of optically pumped lasing action [9,10] and proposals for potential heterostructures for efficient light-emitting applications [11]; at the same time major advances occurred in the control of material purity and defects.
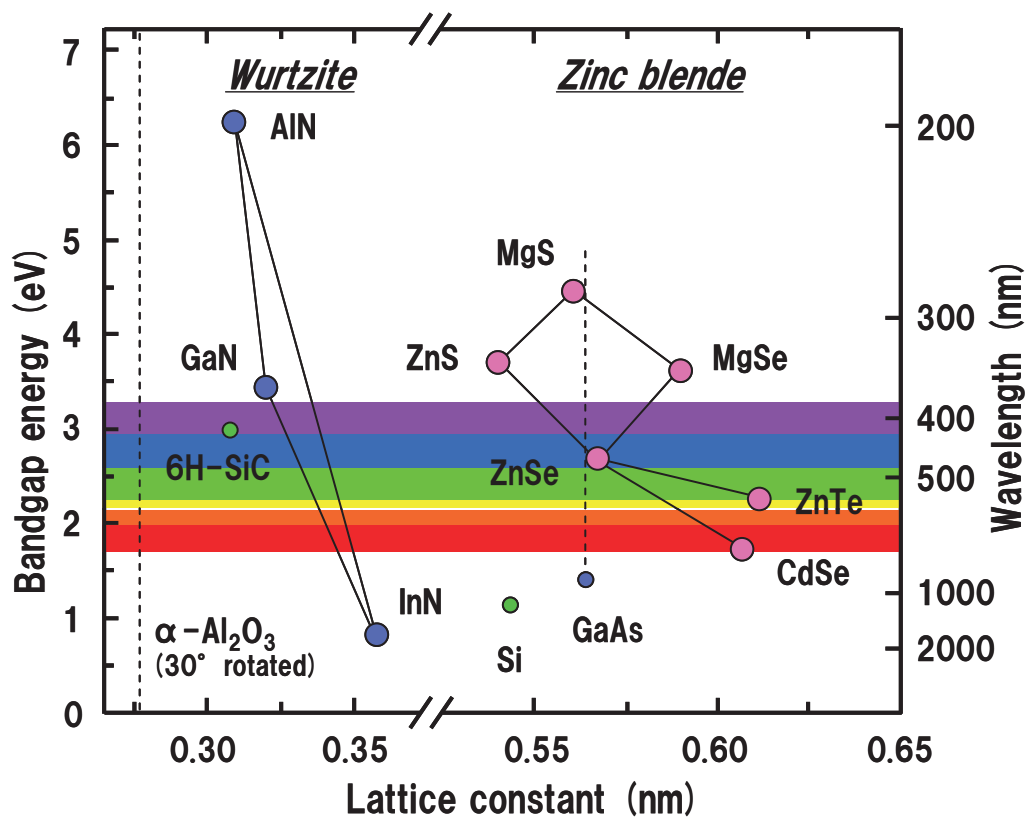
Fig. 1. Bandgap energy at 300 K versus lattice constant for III-nitride semiconductors, II-VI wide bandgap semiconductors and SiC. SiC and Si are indirect bandgap semiconductors.

As a direct consequence of the improved material quality provided by MBE growth, advances were made in the p-type and n-type conductivity control of ZnSe; it is primarily this compound and its alloys which form the basis for today's II-VI heterostructure research. The attaining of p-type doping using nitrogen in particular, first demonstrated in 1990 [12,13], when combined with the knowledge accumulated from research into the physical properties of II-VI heterostructures and the materials advances associated with MBE process, provided an opportunity for attempting the realization of the blue-green LDs. In 1991 a group of 3M Corporate Research Laboratories [14] announced the demonstration of such LDs, first under pulsed excitation at cryogenic temperatures. Following rapid progress, the first demonstration of room-temperature (RT) continuous-wave (CW) operation of ZnCdSe/ZnSSe/ZnMgSSe LD was made in 1993 [15]. The lifetime was reached up to 500h under a constant power of 1 mW [16]. However, the short lifetime prevents II-VI based devices from commercialization at present. It is considered that the short lifetime of these devices is caused by crystal defects at a density of 10^3-10^4 cm^{-2}, because one crystal defect would cause the propagation of other defects leading to failure of the devices.

On the other hand, GaN and related materials such as AlGaInN are III-nitride compound semiconductors with the wurtzite crystal structure and a direct energy band structure which is suitable for light-emitting devices. The bandgap energy of AlGaInN varies between 6.2 and 0.7 eV depending on its composition at room temperature shown in Fig. 1. Therefore, these III-nitride semiconductors are useful for light-emitting devices especially in the short wavelength regions. Sapphire substrates which have a lattice mismatch of 16% between GaN and sapphire have been used mainly for the growth of the III-nitrides based blue LED and LD structure. Major developments in III-nitrides have led to the commercial production of high-brightness blue and green LEDs [17,18]. By combining these LEDs, many kinds of applications, such as LED full-color displays and LED white lamps for use in place of light bulbs or fluorescent lamps, are now possible with characteristics of high reliability, high durability and low energy consumption. Furthermore, the developments in III-nitrides have led to the demonstration of violet laser emission in InGaN/GaN/AlGaN heterostructure of RT-CW operation [19,20]. These developments resulted from the realization of high-quality crystals of AlGaN and InGaN, and p-type conduction in AlGaN by metalorganic vapor phase epitaxy

(MOVPE) [21-25]. Recombination of localized excitons was proposed as an emission mechanism for the spontaneous emission of the InGaN multiple quantum well (MQW) LEDs and LDs [26-28]. The radiative recombination of the spontaneous and stimulated emission of the InGaN MQW was attributed to excitons localized at traps which originated from the In-rich region in the InGaN wells acting as quantum dots.

The present dissertation describes the development of ZnSe-based and GaN-based LDs in which I was engaged from 1991 to 2001. It contains the fabrication and characterization of these LDs, the clarification of gain mechanism, the design of an MOVPE reactor and the development of novel epitaxial growth methods such as compound source MBE (CSMBE) for ZnMgSSe quaternary LDs and air-bridged lateral epitaxial growth (ABLEG) using MOVPE for GaN with low dislocation density. The following issues are studied in this dissertation.

The ZnSe-based LDs previously reported have GaAs buffer layers grown in an extra III-V MBE chamber interconnecting II-VI's via an ultrahigh-vacuum transfer tube in order to suppress the crystal defects at the interface with GaAs substrates [14]. It is interesting to investigate whether the GaAs buffer layer is necessary for the laser action. The cavity parameters of LDs are important to design the LD structure for RT-CW operation. The characterization of these parameters, however, has never been examined for ZnSe-based LDs.

In the ZnCdSe/ZnSe quantum wells, the gain mechanism has been explained in terms of the phase-space filling effect on excitons, which are broadened inhomogeneously due to compositional fluctuation in the wells at cryogenic temperatures [29]. It is essential, however, to demonstrate these effects at room temperature because larger homogeneous broadening may change the situation.

With respect to conventional MBE that employs mainly elemental sources such as Zn, Cd and Se, some difficulty exists in the control of the composition of alloys due to the number of temperatures to be adjusted and to the accuracy of relative intensity of three or more beam fluxes. Since the CSMBE that employs polycrystalline compounds is able to reduce the number of source materials and to stabilize the VI/II beam flux ratio around unity, it is worth proving the CSMBE to improve the uniformity and reproducibility of quaternary alloys of the laser structure.

Metalorganic vapor phase epitaxy is a leading technology for GaN-based devices. This technology, however, is not a satisfactory level for high power commercial LDs from the standpoint of crystalline quality itself and the overall epitaxy process control. Since the crystalline quality strongly depends on the MOVPE growth, it is important to clear guidelines for optimum operating conditions.

InGaN MQW structure has a problem of considerable bandgap inhomogeneity caused by the inherent compositional fluctuation because of highly incomplete solubility [27]. However, the relation between the inhomogeneity and the laser performance has been unclear. In order to clarify the stimulated emission mechanism and to obtain high gain for the LDs, it is necessary to study the origin of optical gain at various temperatures for InGaN alloys with different In contents.

AlGaN has a potential for use in LDs, LEDs and detectors covering nearly the entire deep-ultraviolet (UV) region of the spectrum (200-365 nm). Despite a considerable amount of research directed towards InGaN-based violet LEDs and LDs, very little research has been conducted on AlGaN-based UV LEDs and LDs [30,31]. Although the introduction of MQW structure is promising, the large strain due to the difference in the Al contents between the well layers and the barrier layers causes a significant piezoelectric field resulting in the longer emission wavelength and poorer emission efficiency. Therefore, it is difficult to shorten the emission wavelength simply by narrowing the well thickness or by increasing the Al content in the barrier layers [32].

The lifetime as long as 10,000 h for RT-CW operation of InGaN MQW LDs grown on the lateral epitaxial overgrown (LEO) GaN [33] suggests that reducing the threading dislocation density in GaN is a most promising way in which higher performance of GaN-based LDs can be realized. On the other hand, the wing region of LEO-GaN films have tilt angles of larger than 0.1° related to the strain between the LEO-GaN films and mask materials. Introduction of the air gap between the LEO-GaN and the mask is effective to exclude the strain. A promising method of selective area growth combined with LEO, namely air-bridged lateral epitaxial growth (ABLEG) has been developed for not only reduction in threading dislocation density but also decrease in the influence of mask materials.

As for the correlation between threading dislocation and recombination pathway, it has

been reported that the threading dislocation acts as the nonradiative recombination centers [34]. Furthermore, Nakamura has reported that the difference in the emission efficiency between LEDs grown on sapphire and LEO-GaN substrates becomes smaller with increasing In content in InGaN [35]. Therefore, it is of great significance to investigate the detailed recombination dynamics in GaN and InGaN with different threading dislocation density on ABLEG-GaN films. In addition, the actual correlation between the nonradiative recombination process and the threading dislocation density is still unknown because the direct observation of the nonradiative recombination process has been very difficult.

Summary of each chapter

Chapter 1 presents the fabrication of ZnSe-based LDs, the achievement of lasing and the characterization of the LDs. In section 1.1, laser action of ZnSe-based LDs grown directly on GaAs substrates was demonstrated for the first time at 77 K. The $Zn_{0.7}Cd_{0.3}Se$ single quantum well (SQW) LDs showed very low threshold current density since they have large band offsets. The obtained performance was presumably limited not by GaAs buffer layers but by other LD structure. In section 1.2, the cavity parameters were investigated for ZnCdSe/ZnSe/ZnSSe SQW separate confinement heterostructure LDs at 77 K. The transparency current density was estimated to be 3-4 times larger than that for bulk GaAs. I pointed out that lattice-matched heterostructures would lead to reduction of the operation current. In section 1.3, optical gain spectra were investigated for the laser structure at room temperature. An optical gain of several tens of cm^{-1} was achieved for 100 kW/cm^2 at the exciton tail region. The gain mechanism was discussed in terms of phase-space filling of an inhomogeneously broadened exciton state. In section 1.4, electrically pumped ZnCdSe/ZnSe blue-green vertical-cavity surface-emitting lasers (VCSELs) were demonstrated for the first time. The VCSELs are expected for two-dimensional laser arrays and optoelectronic interconnection modules. In section 1.5, real index-guided blue-green LDs with small beam astigmatism were demonstrated for the first time by using a ZnO buried layer and the electron cyclotron resonance plasma etching technique. Small beam astigmatism is very important for high-density optical disk memories and laser printers to enable effective focusing of the laser beam on the smallest spot.

Chapter 2 presents the fabrication and characterization of GaN-based LDs and LEDs. In section 2.1, three-dimensional fluid simulations were performed in a horizontal reactor for GaN MOVPE. It was found that the gas flow rate rather than the velocity or the pressure was a key parameter which controls the spatial distribution of the gas-phase reaction. In section 2.2, the dependence of amplified spontaneous emission spectra in $In_XGa_{1-X}N$/GaN MQWs (X = 0.07-0.11) suggested that low In content led to small bandgap inhomogeneity. Threshold current density of the MQW LDs decreased with decreasing In content. Room-temperature CW operation was achieved in the MQW LD with X = 0.07. It is important to suppress the bandgap inhomogeneity in the InGaN MQW by optimizing In content. In section 2.3, the origin of optical gain in $In_XGa_{1-X}N$/GaN MQW was investigated. It was found that the alloy inhomogeneity of In content increases the width of the gain spectrum and decreases its value. It is considered that the stimulated emission observed at the high-energy end of spontaneous emission originates from the optical gain due to electron-hole plasma around the mobility edge. In section 2.4, room-temperature UV emission was observed at a peak wavelength of 339nm from $Al_{0.13}Ga_{0.87}N$/$Al_{0.10}Ga_{0.90}N$ double heterostructure LEDs by introducing undoped barrier layers which sandwiched the active layer. The dependence of emission intensity on injection current suggests that the diffusion current for the recombination process was dominant at high injection current level. The suppression of carrier overflow is proposed to decrease longer wavelength emission in UV LD and LED operations.

Chapter 3 presents the development of novel epitaxial growth methods for ZnSe-based LDs and GaN-based LDs presented in the previous two chapters, respectively. In section 3.1, I describe CSMBE that employs binary polycrystalline compounds as source materials instead of elements and can reduces the number of growth parameters for ZnSe-based II-VI materials. The surface of ZnSe during CSMBE is Se-stabilized in spite of the VI/II ratio of unity. The composition modulation was not observed for ZnMgSSe quaternary layers grown by CSMBE. These results are owing to hot and group VI diatomic molecular beam generated from compound sources. Continuous-wave operation of ZnCdSe/ZnSSe/ZnMgSSe LDs grown by CSMBE was demonstrated at room temperature. Since CSMBE has the surface migration enhancement effect at the growth front due to high kinetic energy of source molecules, a high growth rate of 2-3 μm/h was achieved for ZnSe films and related laser structures which had high

crystalline quality comparable to that of the films grown at the conventional growth rate.

Section 3.2 presents the development of a novel promising method of selective area growth namely ABLEG which obtains high-quality GaN films with low dislocation density and low wing tilt of c-axis orientation, using low-pressure MOVPE. The threading dislocation density was $10^6 \, \text{cm}^{-2}$ in the wing region, while $10^9 \, \text{cm}^{-2}$ in the seed region. The tilt angle of the wing region was relatively small compared with other LEO-GaN films because the air-gap between the wing and the mask material is effective in making the ABLEG-GaN free from strain. Recombination dynamics in GaN and InGaN/GaN MQW on ABLEG-GaN was studied by means of spatial and time-resolved photoluminescence spectroscopy and microscopic transient lens spectroscopy for the first time. Comparing the ratio of the difference between PL lifetime at the wing and the seed regions, threading dislocations affect less carrier recombination process in InGaN/GaN MQW than in GaN. This is explained by the model of carrier localization in InGaN QW layers. The origin of localization is considered to be the fluctuation of well width and In content. It was found that the thermal conductivities were not so different at the seed region and the wing region of ABLEG-GaN and InGaN/GaN MQW, however, the amount of heat generated at the wing region was much smaller than that at the seed region. At the wing region, low threading dislocation density should reduce the nonradiative recombination processes of carriers.

References

[1] W. Xie, D. C. Grillo, R. L. Gunshor, M. Kobayashi, H. Jeon, J. Ding, A. V. Nurmikko, G. C. Hua, and N. Otsuka, *Appl. Phys. Lett.* **60**, 1999 (1992).

[2] D. E. Eason, Z. Yu, W. C. Hughes, W. H. Roland, C. Boney, J. W. Cook Jr., J. F. Schetzina, G. Cantwell, and W. C. Harasch, *Appl. Phys. Lett.* **66**, 115 (1995).

[3] J. I. Pankove, E. A. Miller, and J. E. Berkeyheiser, *RCA Review* **32**, 283 (1971).

[4] J. Edmond, H. Kong, and V. Dmitriev, *Inst. Phys. Conf. Ser.* **137**, 515 (1994).

[5] R. L. Gunshor, L. A. Kolodziejski, A. V. Nurmikko, and N. Otsuka, *Semiconductor and Semimetals* **37**, 337 (1991).

[6] G. Mandel, F. F. Morehead, and P. R. Wagner, *Phys. Rev. A* **136**, 826 (1964).

[7] F. A. Kroger, *J. Chem. Phys. Solids* **26**, 1717 (1965).

[8] R. K. Watts, W. C. Holton, and M. de Wit, *Phys. Rev. B* **3**, 404 (1971).

[9] R. B. Bylsma, W. M. Becker, T. C. Bonsett, L. A. Kolodziejski, R. L. Gunshor, M. Yamanishi, and S. Datta, *Appl. Phys. Lett.* **47**, 1039 (1985).

[10] D. A. Cammack, R. J. Dalby, H. J. Cornelissen, and J. Khurgin, *J. Appl. Phys.* **62**, 3071 (1987).

[11] J. Ding, N. Pelekanos, A. V. Nurmikko, H. Luo, N. Samarth, and J. Furdyna, *Appl. Phys. Lett.* **57**, 2885 (1990).

[12] R. M. Park, M. B. Troffer, C. M. Rouleau, J. M. DePuydt, and M. A. Haase, *Appl. Phys. Lett.* **57**, 2127 (1990).

[13] K. Ohkawa, T. Karasawa, and T. Mitsuyu, *Jpn. J. Appl. Phys.* **30**, L152 (1991).

[14] M. A. Haase, J. Qiu, J. M. DePuydt, and H. Cheng, *Appl. Phys. Lett.* **59**, 1272 (1991).

[15] N. Nakayama, S. Itoh, T. Ohata, K. Nakano, H. Okuyama, M. Ozawa, A. Ishibashi, M. Ikeda, and Y. Mori, *Electron. Lett.* **29**, 1488 (1993).

[16] S. Itoh, K. Nakano, and A. Ishibashi, *J. Cryst. Growth* **214/215**, 1029 (2000).

[17] S. Nakamura, M. Senoh, N. Iwasa, S. Nagahama, T. Yamada, and T. Mukai, *Jpn. J. Appl. Phys.* **34**, L1332 (1995).

[18] S. Nakamura and G. Fasol, *The Blue Laser Diode*, 1st ed. (Springer-Verlag, Berlin, 1997).

[19] S. Nakamura, M. Senoh, S. Nagahama, N. Iwasa, T. Yamada, T. Matsushita, Y. Sugimoto, and H. Kiyoku, *Appl. Phys. Lett.* **69**, 4056 (1996).

[20] S. Nakamura, M. Senoh, S. Nagahara, N. Iwasa, T. Yamada, T. Matsushita, H. Kiyoku, Y. Sugimoto, T. Kozaki, H. Umemoto, M. Sano, and K. Chocho, *Jpn. J. Appl. Phys.* **37**, L309 (1998).

[21] S. Strite and H. Morkoç, *J. Vac. Sci. Technol. B* **10**, 1237 (1992).

[22] H. Amano, M. Kito, K. Hiramatsu, and I. Akasaki, *Jpn. J. Appl. Phys.* **28**, L2112 (1989).

[23] S. Nakamura, N. Iwasa, M. Senoh, and T. Mukai, *Jpn. J. Appl. Phys.* **31**, 1258 (1992).

[24] S. Nakamura and T. Mukai, *Jpn. J. Appl. Phys.* **31**, L1457 (1992).

[25] M. A. Khan, J. N. Kuznia, A. R. Bhattarai, and D. T. Olson, *Appl. Phys. Lett.* **62**, 1786 (1993).

[26] S. Chichibu, T. Azuhata, T. Sota, and S. Nakamura, *Appl. Phys. Lett.* **69**, 4188 (1996).

[27] Y. Narukawa, Y. Kawakami, Sz. Fujita, Sg. Fujita, and S. Nakamura, *Phys. Rev. B* **55**,

R1938 (1997).

[28] Y. Narukawa, Y. Kawakami, M. Funato, Sz. Fujita, Sg. Fujita, and S. Nakamura, *Appl. Phys. Lett.* **70**, 981 (1997).

[29] J. Ding, M. Hagerott, T. Ishihara, H. Jeon, and A. V. Nurmikko, *Phys. Rev. B* **47**, 10528 (1993).

[30] H. Hirayama and Y. Aoyagi, *Ext. Abstr. 18th Electronic Materials Symp.* (1999) p.79.

[31] Y. Ohba and H. Yoshida, *Jpn. J. Appl. Phys.* **37**, L905 (1998).

[32] T. Nishida and N. Kobayashi, *Phys. Status Solidi A* **176**, 45 (1999).

[33] S. Nakamura, M. Senoh, S. Nagahama, N. Iwasa, T. Matsushita, and T. Mukai, *MRS Internet J. Nitride Semicond. Res.* **4S1**, G1.1 (1999).

[34] T. Sugahara, M. Hao, T. Wang, D. Nakagawa, Y. Naoi, K. Nishino, and S. Sakai, *Jpn. J. Appl. Phys.* **37**, L1195 (1998).

[35] S. Nakamura, *JSAP International* **1**, 5 (2000).

Chapter 1

Fabrication and characterization of ZnSe-based blue-green LDs

1.1. Fabrication and lasing characteristics of ZnCdSe SQW LDs without GaAs buffer layers

Introduction

ZnSe-related semiconductors are attractive materials for the fabrication of short-wavelength light-emitting devices in the blue and green region. In recent years important techniques have been developed in ZnSe-based II-VI compounds. Yao *et al.* [1] and Matsumura *et al.* [2] developed molecular beam epitaxial (MBE) growth of high-quality ZnSe and ZnSSe layers. Ohkawa *et al.* realized, for the first time, practical Cl doping [3] and N radical doping technique [4-6] to obtain n- and p-type ZnSe, respectively. ZnCdSe quantum well (QW) structures were studied as a laser medium [7,8]. Gunshor *et al.* [9] showed that GaAs buffer layers eliminate the problems in the interface between ZnSe and the GaAs substrate. Based on these techniques, blue light-emitting diodes (LEDs) [6] and blue-green laser diodes (LDs) [10,11] made with ZnSe-based p-n junctions have been demonstrated.

The blue-green LDs previously reported [10,11] have ZnSe-based QW structures on GaAs substrates with GaAs buffer layers grown in an extra III-V MBE chamber interconnecting II-VI's via an ultrahigh-vacuum transfer tube. It is interesting to examine whether the GaAs buffer layer is necessary for the laser action. In addition, knowledge of device parameters [12] is important to design the LDs operating under room temperature continuous-wave condition. In this section, I describe $Zn_{1-X}Cd_XSe$ (X = 0.15-0.3) single quantum well (SQW) LDs without GaAs buffer layers. The LDs emit green to blue-green coherent light at 77 K. I have investigated the Cd composition ratio X dependence of the lasing wavelength and the temperature dependence of the threshold current.

Experimental

The laser structure is similar to that reported by Haase *et al.* [10], as shown in Fig. 1.1, however, there is no GaAs buffer layer on the GaAs substrate. The QW structures were grown
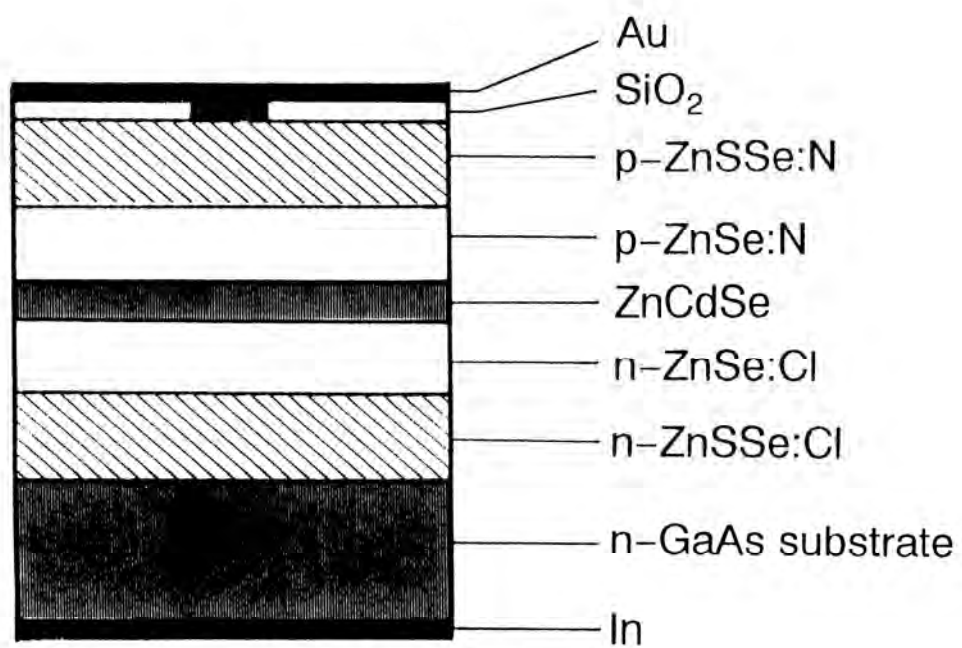
Fig. 1.1. Schematic cross section of a ZnSe-based SQW LD.

directly on n-GaAs (100) substrates by MBE. The substrate was first cleaned in organic solvents, then etched in a mixture of H_2SO_4, H_2O_2 and H_2O. Prior to growth, the substrate was thermally cleaned. The active region of the diodes consisted of an undoped $Zn_{1-X}Cd_XSe$ (X = 0.15-0.3) QW with a typical thickness of 10 nm centered in ZnSe guiding layer with a typical thickness of 0.6 μm. This separate confinement heterostructure (SCH) was sandwiched between typically 1.2 μm-thick $ZnS_{0.07}Se_{0.93}$ cladding layers, which are nearly lattice matched to GaAs substrates at a growth temperature of 325°C. The value of X was determined by photoluminescence and electroluminescence measurements. The conduction band offset ΔE_C and valence band offset ΔE_V in $Zn_{1-X}Cd_XSe$/ZnSe for X = 0.15-0.3 are 140-270 meV and 60-120 meV, respectively. They are calculated by referring the value in Ding *et al.*'s report [13]. Larger ΔE_C and ΔE_V are expected for X = 0.3 compared with other reports [10,11] for X = 0.2. Nitrogen radical doping [4-6] and Cl doping [3] were employed to obtain p- and n-type layers, respectively. Carrier concentrations of p- and n-type layers are 2×10^{17} cm^{-3} and 5×10^{17} cm^{-3}, respectively.

Au and In were used for the contacts to p-type top layers and n-GaAs substrates, respectively. Pt is a promising electrode material for p-type ZnSe [4-6] because its Fermi level is closer to that of p-type ZnSe than that of Au. However, a stripe electrode without stripping off at the edge in cleaving can be fabricated using Au, since Au has smaller shear modulus than Pt. Current confinement was achieved with typically 20μm-wide stripe electrodes defining the top electrical contact by a SiO_2 insulating layer. Mirrors were formed by cleaving facets to make cavities with 700-1300 μm long. Laser devices with both as-cleaved facets and high-reflectivity coated facets were prepared. The devices were mounted on a Cu heat sink with n-GaAs substrates down. Laser action was observed under pulsed current injection at 77 K. The current pulse duration was typically 1 μs and a typical duty cycle was 0.1%.

Results and discussion

Lattice mismatch between the $Zn_{1-X}Cd_XSe$ SQW layer and the ZnSe guiding layer increases with increasing composition ratio X. The values for X = 0.15 and 0.3 are 1.0% and 2.0%, respectively. The critical thicknesses of $Zn_{1-X}Cd_XSe$ layers with X = 0.15 and 0.3 on ZnSe layers are estimated to be 40 and 20 nm, respectively, by assuming that critical thickness is inversely proportional to lattice mismatch and by referring to the critical thickness of the ZnSe layer on a
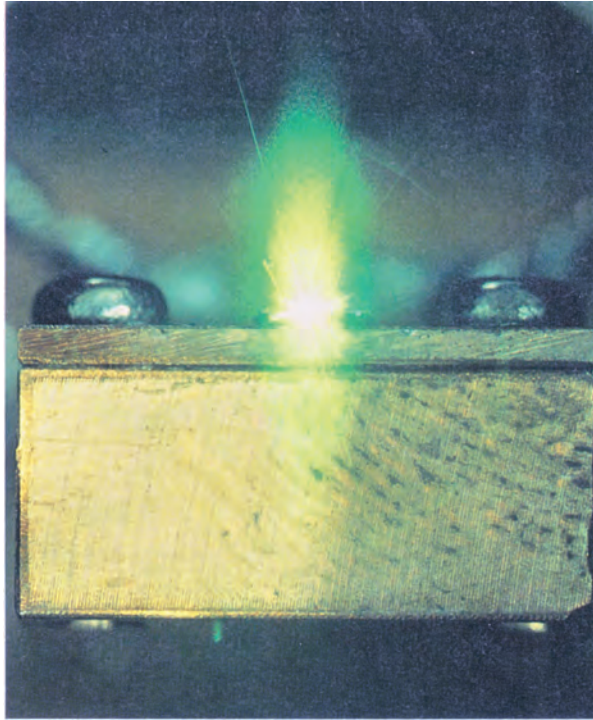
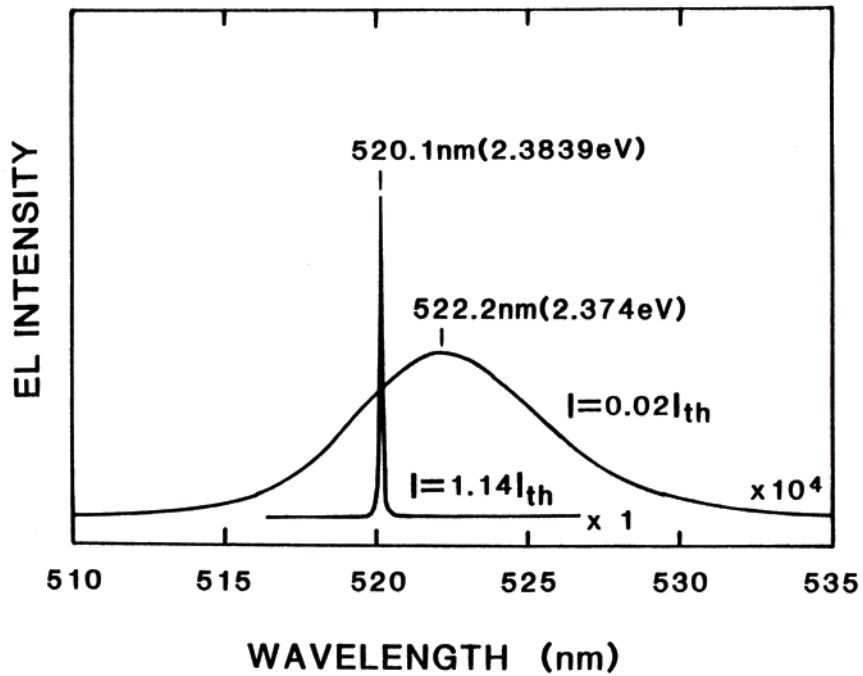Fig. 1.2. Front view of a ZnSe-based SQW LD during lasing at 520 nm.

Fig. 1.3. Spontaneous and stimulated emission spectra for a $Zn_{0.7}Cd_{0.3}Se$ SQW LD under pulsed current injection at 77 K.

GaAs substrate, which is 150 nm with 0.28% lattice mismatch [14]. The thicknesses of the SQWs are less than half the critical thicknesses, thus coherent growth is possible. Double-crystal X-ray diffraction measurement of the LDs shows that the full width at half-maximum (FWHM) of (400) rocking curve for ZnSe guiding layer is about 200 arcsec. The crystallinity is limited mainly by lattice mismatch between the $ZnS_{0.07}Se_{0.93}$ cladding layer and the ZnSe guiding layer, since the same FWHM is observed for ZnSe films on GaAs substrates [3] whose lattice mismatch is the same as for $ZnSe/ZnS_{0.07}Se_{0.93}$.

Figure 1.2 is a photograph showing laser emission from a typical LD during lasing at 520 nm. Spontaneous and stimulated emission spectra shown in Fig. 1.3 were obtained from an LD with $X = 0.3$. In operation at 2% of threshold current I_{th}, the LD emits spontaneous emission and FWHM of the emission is about 5 nm (25 meV). In operation at $1.14I_{th}$, FWHM of stimulated emission is reduced to the limit of the monochrometer, 0.08 nm (0.4 meV). A clear speckle pattern is observed and the laser beam has an elliptical far-field pattern with a divergence of roughly $30° \times 3°$. Figure 1.4 shows lasing spectra at 77 K with various Cd compositions of the active layer. Emission wavelengths are observed from 477 nm (blue) for $X = 0.15$ to 520 nm (green) for $X = 0.3$. The values of I_{th} for these devices were 30-60 mA. The operating voltage at the threshold was typically 30 V, since contact resistance between Au and the p-type layer was high.

Figure 1.5 shows the output power versus injection current (*L-I*) characteristics from one end of a $Zn_{0.7}Cd_{0.3}Se$ SQW-SCH LD with as-cleaved facets at 77 K. The output power exceeded 100 mW. The differential quantum efficiency η_d from both facets is 39%. These values are almost the same with those in the LDs with GaAs buffer layers [10]. In spite of uncoated facets, injected I_{th} was as low as 38 mA, and threshold current density J_{th} was 160 A/cm^2. This J_{th} is half of that in the previous report [10]. On the other hand, the J_{th} for an LD with $X = 0.2$ was 300 A/cm^2. The very low J_{th} of the LDs with $X = 0.3$, therefore, is presumably caused by large band offsets due to the high Cd composition ratio of 0.3. Carrier confinement due to band offset has greater influence on J_{th} than the existence of the GaAs buffer layer.

For as-cleaved devices, the laser action up to 6% in a duty cycle could be achieved at 77 K. Laser action was also observed at temperatures up to 150 K in a duty cycle of 0.1% for an uncoated device.
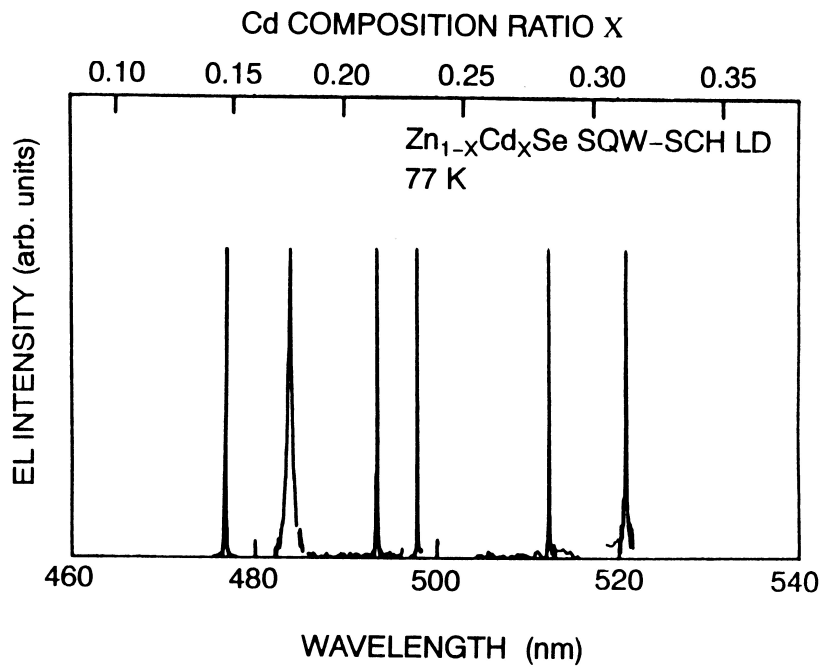
Cd COMPOSITION RATIO X

Fig. 1.4. Lasing spectra at 77 K with various Cd composition ratios of the ZnCdSe/ZnSe SQW-SCH LDs.
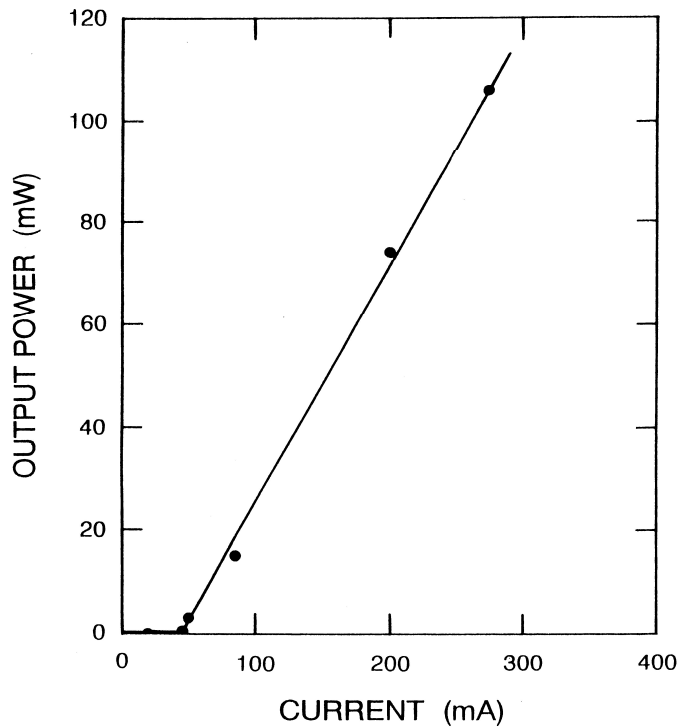

Fig. 1.5. Light output power versus injection current characteristics of a typical uncoated LD under pulsed current injection at 77 K.

Application of a high-reflectivity (HR) coating to as-cleaved facets is able to reduce the threshold current. The reflectivity R for the as-cleaved facet is 26%, using a refractive index of 3.1, for ZnSe around 500 nm at 77 K [12]. The HR facet coating was achieved with dielectric mirrors which consisted of alternating quarter-wavelength layers of SiO_2 and TiO_2. The reflectivity for the HR coated facet was obtained to be 90%. In the case of the as-cleaved device, I_{th} was 56 mA for a device with $X = 0.25$ and with a cavity length L of 760 μm. Its external differential quantum efficiency η_d was 27%. Applying 90%-90% HR coating on both facets, I_{th} drastically reduced to 25 mA and η_d to 12%. The mirror loss $\ln(1/R)/L$ is estimated to be 18 cm^{-1} and 1.4 cm^{-1} for the uncoated and the HR coated devices, respectively. Both of the devices have a low internal loss of 2.0 cm^{-1} determined from the following relation between the η_d and the effective cavity length L_{eff} [15]:

$$\frac{1}{\eta_d} = \frac{1}{\eta_{stim}}\left(1 + \alpha L_{eff}\right),$$
(1.1)

where η_{stim} is the internal quantum efficiency above the threshold, α is the internal loss coefficient and L_{eff} is defined as $L/\ln(1/R)$. A threshold loss, which is the sum of the internal loss and the mirror loss, of 20 cm^{-1} for the as-cleaved device is reduced to that of 3.4 cm^{-1} by applying the 90%-90% HR coating. This results in the clear reduction in the threshold current.

Figure 1.6 shows the temperature dependence of the threshold current I_{th} for the device with 90%-90% HR coating. Laser action is observed at temperatures up to 250 K. An exponential variation of I_{th} with temperature T is observed. The relation is represented by [15]

$$I_{th} = I_0 \exp\left(\frac{T}{T_0}\right)$$
(1.2)

with a characteristic temperature T_0 of 65 K. An excess injection-current component is not observed up to 250 K in Fig. 1.6. It is found that the carrier leakage current from the active layer into the cladding layers is negligibly small. ΔE_C of 230 meV in $Zn_{0.75}Cd_{0.25}Se/ZnSe$ is large enough to prevent the electron overflow which dominates the carrier overflow at a temperature of 250 K.

Furthermore, it is surprising that 90%-90% HR coated devices operated with a current of 350 mA at 250 K although as-cleaved devices burnt out with only 100 mA. The application of HR coating obtained not only higher-temperature operation but also higher-reliability operation
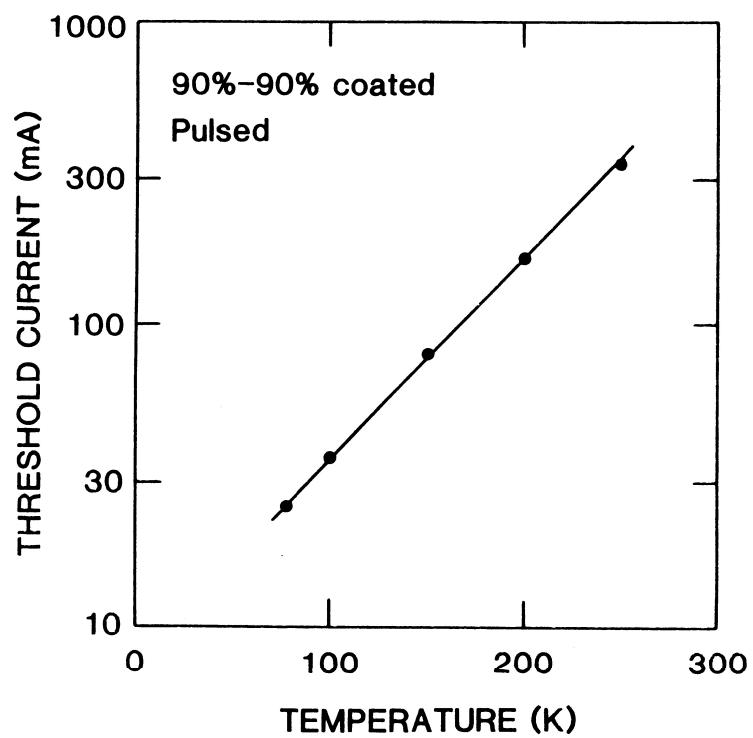
17

Fig. 1.6. Temperature dependence of the threshold current for a device with 90%-90% HR coating under pulsed operation.

under which uncoated devices are incapable to operate.

Conclusion

It was demonstrated, for the first time, that lasing of ZnSe-based LDs without GaAs buffer layers is possible. The $Zn_{1-X}Cd_XSe$ SQW-SCH LDs with $X = 0.3$ showed very low J_{th}, since they have large band offsets. The present performance of ZnSe-based LDs was presumably limited not by GaAs buffer layers but by other factors such as laser structure and contact with the p-type ZnSe. The influence of GaAs buffer layers will be observed for LDs having optimized structure and contact. I investigated the Cd composition ratio X dependence of the lasing wavelength and the temperature dependence of the threshold current. The lasing wavelength varied from 477 nm for $X = 0.15$ to 520 nm for $X = 0.3$ at 77 K. Clear reduction in the threshold current was observed by applying HR facet coating. The 90%-90% HR coated devices with $X = 0.25$ lased without causing the carrier leakage up to 250 K.

References in 1.1

[1] T. Yao, S. Amano, M. Ogura, S. Matsuoka, and T. Morishita, *Appl. Phys. Lett.* **43**, 499 (1983).

[2] N. Matsumura, M. Tsubokura, J. Saraie, and Y. Yodogawa, *J. Cryst. Growth* **86**, 311 (1988).

[3] K. Ohkawa, T. Mitsuyu, and O. Yamazaki, *J. Appl. Phys.* **62**, 3216 (1987).

[4] K. Ohkawa, T. Karasawa, and T. Mitsuyu, *J. Cryst. Growth* **111**, 797 (1991).

[5] K. Ohkawa, T. Karasawa, and T. Mitsuyu, *Jpn. J. Appl. Phys.* **30**, L152 (1991).

[6] K. Ohkawa, A. Ueno, and T. Mitsuyu, *Jpn. J. Appl. Phys.* **30**, 3873 (1991).

[7] H. Jeon, J. Ding, A. V. Nurmikko, H. Luo, N. Samarth, and J. K. Furdyna, *Appl. Phys. Lett.* **57**, 2413 (1990).

[8] Y. Kawakami, S. Yamaguchi, Y.-H. Wu, K. Ichino, Sz. Fujita, and Sg. Fujita, *Jpn. J. Appl. Phys.* **30**, L605 (1991).

[9] R. L. Gunshor, L. A. Kolodziejski, M. R. Melloch, M. Vaziri, C. Choi, and N. Otsuka, *Appl. Phys. Lett.* **50**, 200 (1987).

[10] M. A. Haase, J. Qiu, J. M. DePuydt, and H. Cheng, *Appl. Phys. Lett.* **59**, 1272 (1991).

[11] H. Jeon, J. Ding, W. Patterson, A. V. Nurmikko, W. Xie, D. C. Grillo, M. Kobayashi, and R.

L. Gunshor, *Appl. Phys. Lett.* **59**, 3619 (1991).

[12] A. Tsujimura, S. Yoshii, S. Hayashi, K. Ohkawa, and T. Mitsuyu, *Jpn. J. Appl. Phys.* **32**, L1570 (1993).

[13] J. Ding, N. Pelekanos, A. V. Nurmikko, H. Luo, N. Samarth, and J. Furdyna, *Appl. Phys. Lett.* **57**, 2885 (1990).

[14] H. Mitsuhashi, I. Mitsuishi, M. Mizuta, and H. Kukimoto, *Jpn. J. Appl. Phys.* **24**, L578 (1985).

[15] H. C. Casey Jr. and M. B. Panish, *Heterostructure Lasers* (Academic Press, New York, 1978) chap. 3.

1.2. Cavity parameters of ZnCdSe/ZnSe/ZnSSe SQW-SCH LDs

Introduction

ZnSe-related II-VI semiconductors are attractive materials for the fabrication of short-wavelength light-emitting devices in the blue and green regions. Ohkawa *et al.* reported, for the first time, on Cl doping [1] and N radical doping techniques [2-4] to obtain practical n- and p-type ZnSe, respectively. Breakthroughs in the doping technique have recently led to remarkable success in realizing blue-green laser diodes (LDs) [5-9]. II-VI heterostructures and materials for LDs have also been intensively investigated. However, characterization of the internal device properties such as cavity parameters has never been reported for these devices except a preliminary study on the cavity length dependence of the threshold current density [8]. In this section, I describe the cavity length dependence of the external differential quantum efficiency and the threshold current density for ZnCdSe/ZnSe/ZnSSe single quantum well separate confinement heterostructure (SQW-SCH) LDs.

Experimental

The device structure was grown directly on an n-GaAs (100) substrate by molecular beam epitaxy. The light-emitting region consisted of a 0.018 μm-thick pseudomorphic undoped $Zn_{0.83}Cd_{0.17}Se$ strained quantum well (QW) centered in a 0.7 μm-thick ZnSe guiding layer. The upper and lower cladding layers are 2.0 μm-thick $ZnS_{0.07}Se_{0.93}$, which is nearly lattice-matched to the GaAs substrate at a growth temperature of 325°C. The conduction and valence band offsets in $Zn_{0.83}Cd_{0.17}Se$/ZnSe are calculated to be 150 meV and 70 meV, respectively. N radical doping [2-4] and Cl doping [1] were employed to obtain p- and n-type layers, respectively. Carrier concentrations of p- and n-type layers are both 3×10^{17} cm^{-3} at room temperature.

Au and In were used for the contacts to p-type top layers and n-GaAs substrates, respectively. Polyimide was used as insulating layer to define the current. Finished devices had a stripe width of 10 μm and were cleaved to a cavity length of 400-3460 μm. Neither facet of the diodes was coated. The devices were mounted on Cu heat sinks in the junction-up configuration. The device performance was characterized using 1 μs-long pulses at a duty cycle of 0.1% at 77 K.
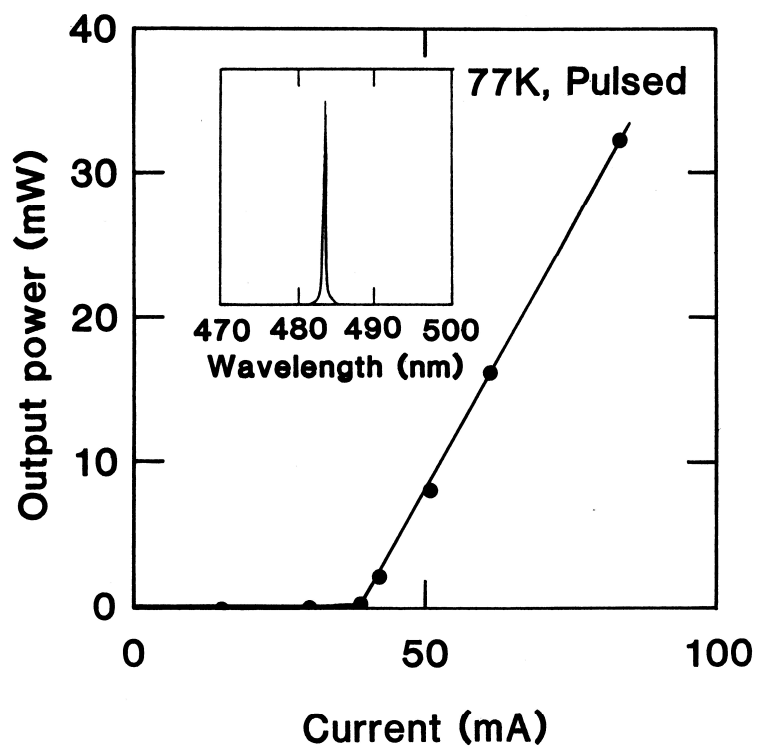
Fig. 1.7. Pulsed output power per facet as a function of injection current for a 690 μm-long SQW-SCH laser diode at 77 K. The inset shows the emission spectrum for this device operating at 45 mA.

Results and discussion

Figure 1.7 shows the output power per facet versus injection current for a 690 μm-long device at 77 K. Threshold current I_{th} is 39 mA, the external differential quantum efficiency η_d from both facets is 57% and the maximum output power is greater than 30 mW. The inset of Fig. 1.7 shows the spectrum for this laser. An emission wavelength of 483.7 nm is observed in operation at a current of 45 mA. The operating voltage at the threshold was typically 29 V, since contact resistance between Au and the p-type layer was high. The temperature dependence of I_{th} was observed. Log I_{th} depended linearly on temperature with a characteristic temperature of 105 K over the temperature range of 77-150 K. This suggests that carrier leakage from the active layer into the cladding layers does not occur at 77 K.

Figure 1.8 shows the inverse external differential quantum efficiency as a function of the cavity length L for eight devices operating at around 484 nm at 77 K. The values of $1/\eta_d$ are observed to satisfy the following relationship [10]:

$$\frac{1}{\eta_d} = \frac{1}{\eta_{stim}}\left\{1 + \frac{\alpha L}{\ln(1/R)}\right\}, \tag{1.3}$$

where η_{stim} is the internal quantum efficiency above the threshold, α is the internal loss coefficient, and R is the facet reflectivity. The equivalent index for the guided mode in the present SQW-SCH is calculated to be 2.73 at a wavelength of 484 nm, using the following refractive indices of 2.73, 2.71 and 2.87 for ZnSe, $ZnS_{0.07}Se_{0.93}$ and $Zn_{0.83}Cd_{0.17}Se$, respectively at 77 K. Then, the reflectivity for an as-cleaved facet of the laser devices is calculated to be 21.5%. The internal loss and the internal quantum efficiency are determined from the slope and the intercept (at $L = 0$) of the linearly extrapolated curve of Fig. 1.8, respectively. This yields $\alpha = 1.5$ cm^{-1} and $\eta_{stim} = 61\%$. The low internal loss results from the low overlap of the optical wave with the active layer as specified by the optical confinement factor Γ. For the present SQW-SCH, Γ is calculated to be 3.8%. The internal loss α is written as [10]

$$\alpha = \Gamma\alpha_{fa} + (1-\Gamma)\alpha_{fc} + \alpha_s + \alpha_c, \tag{1.4}$$

where α_{fa} and α_{fc} are the free-carrier absorption loss in the active layer and in the adjacent cladding layers, respectively, α_s is the scattering loss and α_c is the coupling loss. The free-carrier loss depends on the carrier concentration. When α_{fa} and α_{fc} are assumed to be 10 cm^{-1} for 10^{18} cm^{-3} and 1 cm^{-1} for 10^{17} cm^{-3}, respectively, on analogy with GaAs [10], the sum of the first and
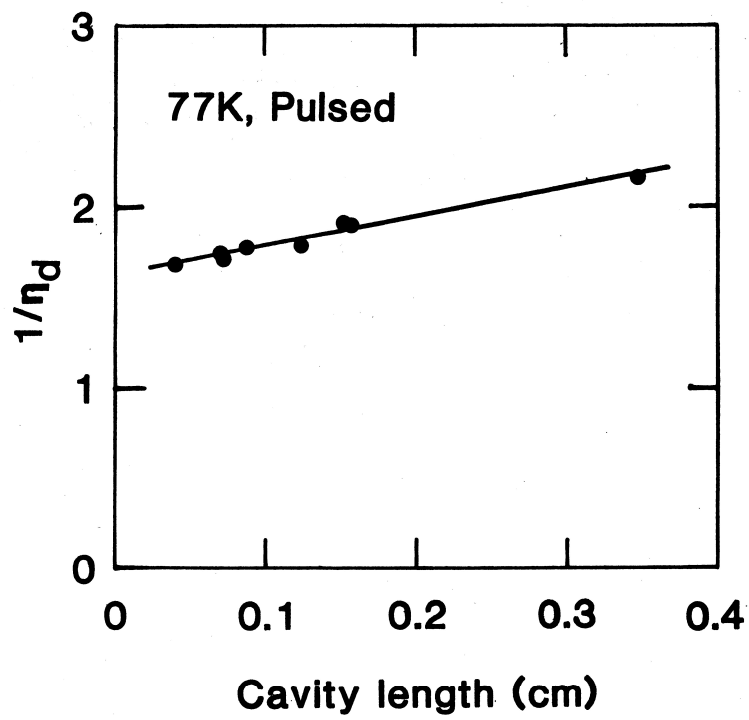
Fig. 1.8. Reciprocal of the external differential quantum efficiency as a function of cavity length under pulsed current injection at 77 K.

the second terms of Eq. (1.4) is 1.3 cm^{-1}; therefore most of the internal loss is attributed to the free-carrier absorption. The internal quantum efficiency of 61% for stimulated emission suggests that spatially effective interaction between carriers and a laser mode is insufficient.

Figure 1.9 shows a variation of the threshold current density J_{th} with the inverse cavity length for the same devices shown in Fig. 1.8. The threshold current density increases proportionally with $1/L$, indicating a linear dependence of the optical gain coefficient on the injected current density. Namely, the threshold current density is represented by [10]

$$J_{th} = \frac{J_0 d}{\eta_{spon}} + \frac{d\alpha}{\beta\Gamma\eta_{spon}} + \frac{d}{\beta\Gamma\eta_{spon}}\frac{\ln(1/R)}{L},$$ (1.5)

where J_0 is the transparency current density, β is the gain factor, d is the thickness of the active layer and η_{spon} is the internal quantum efficiency below the threshold. The value of η_{spon} is assumed to be 12%, estimated by comparing the intensity of photoluminescence from the QW under high excitation density (the carrier density in the QW exceeded 1×10^{17} cm^{-3}) at 77 K with that at 4.2 K, where η_{spon} is considered to be 100%. A transparency current density of 1.8 kA/cm^{2}μm and a gain factor of 0.36 cm^{2}μm/A were obtained from Eq. (1.5) using the following values of d = 0.018 μm, η_{spon} = 0.12, α = 1.5 cm^{-1} and Γ = 0.038. The transparency current density means the value of the nominal current density per 1 μm-thick active layer at which the maximum gain becomes zero. The value of J_0 deduced experimentally for 0.018 μm-thick Zn$_{0.83}$Cd$_{0.17}$Se is 3-4 times larger than that for bulk GaAs at 77 K [11]. This result is consistent with a theoretical calculation of the optical gain [12]. The reduced optical gain in II-VI semiconductors compared with III-V semiconductors is attributed to the larger effective mass of the electron and hole. We are interested in the relationship between optical gain and current density at higher temperature and the relationship with the carrier lifetime. Such information will lead to illumination of the mechanism of the laser action in II-VI semiconductors.

In order to reduce the operation current, it is necessary to improve the value of η_{spon} at present. The dislocation density in the active layer of our LDs exceeds 10^7 cm^{-2}. This is largely due to the mismatch between guiding and cladding layers. Lattice-matched heterostructures with low dislocation density and with good carrier confinement are essential to improved performance. Although J_0 and β are intrinsic material parameters, employment of a well-engineered strained-layer QW enables improvement of the relationship between optical
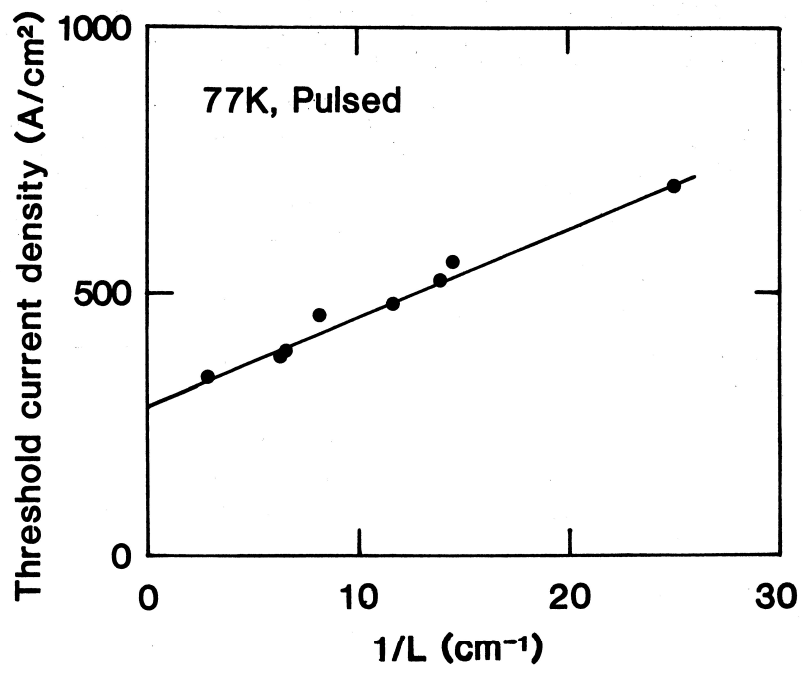
Fig. 1.9. Threshold current density as a function of inverse cavity length under pulsed current injection at 77 K.

gain and current density.

Conclusion

I estimated the cavity parameters of ZnCdSe/ZnSe/ZnSSe SQW-SCH LDs at 77 K. Internal loss of 1.5 cm^{-1} and internal quantum efficiency of 61% for stimulated emission were obtained. A transparency current density of 1.8 kA/cm^{2}μm and a gain factor of 0.36 cm^{2}μm/A were deduced from an internal quantum efficiency of 12% for spontaneous emission which was measured in photoluminescence experiments. The transparency current density is 3-4 times larger than that for bulk GaAs. It is necessary for lattice-matched heterostructures to reduce the operation current.

References in 1.2

[1] K. Ohkawa, T. Mitsuyu, and O. Yamazaki, *J. Appl. Phys.* **62**, 3216 (1987).

[2] K. Ohkawa, T. Karasawa, and T. Mitsuyu, *J. Cryst. Growth* **111**, 797 (1991).

[3] K. Ohkawa, T. Karasawa, and T. Mitsuyu, *Jpn. J. Appl. Phys.* **30**, L152 (1991).

[4] K. Ohkawa, A. Ueno, and T. Mitsuyu, *Jpn. J. Appl. Phys.* **30**, 3873 (1991).

[5] M. A. Haase, J. Qiu, J. M. DePuydt, and H. Cheng, *Appl. Phys. Lett.* **59**, 1272 (1991).

[6] H. Jeon, J. Ding, W. Patterson, A. V. Nurmikko, W. Xie, D. C. Grillo, M. Kobayashi, and R. L. Gunshor, *Appl. Phys. Lett.* **59**, 3619 (1991).

[7] S. Hayashi, A. Tsujimura, S. Yoshii, K. Ohkawa, and T. Mitsuyu, *Jpn. J. Appl. Phys.* **31**, L1478 (1992).

[8] Z. Yu, J. Ren, B. Sneed, K. A. Bowers, K. J. Gossett, C. Boney, Y. Lansari, J. W. Cook Jr., J. F. Schetzina, G. C. Hua, and N. Otsuka, *Appl. Phys. Lett.* **6l**, 1266 (1992).

[9] H. Okuyama, T. Miyajima, Y. Morinaga, F. Hiei, M. Ozawa, and K. Akimoto, *Electron. Lett.* **28**, 1798 (1992).

[10] H. C. Casey Jr. and M. B. Panish, *Heterostructure Lasers* (Academic Press, New York, 1978) chap. 3.

[11] F. Stern, *J. Appl. Phys.* **47**, 5382 (1976).

[12] I. Suemune, K. Nakanishi, Y. Fujii, Y. Kuroda, M. Fujimoto, and M. Yamanishi, *J. Cryst. Growth* **117**, 1068 (1992).

1.3. Optical gain in an inhomogeneously broadened exciton system

Introduction

Since the first demonstrations of blue-green laser diodes (LDs) at cryogenic temperature in 1991 [1,2], many researchers have attempted to achieve room temperature continuous-wave operation of the LDs. One important approach to this goal is in understanding the physics of II-VI LDs. In the ZnCdSe/ZnSe quantum wells, the gain mechanism has been explained in terms of the phase-space filling effect on excitons, which are broadened inhomogeneously due to compositional fluctuation in the wells. Recently, optical gain through quantum wells has been measured at 77 K by means of a time-resolved pump-probe technique to demonstrate the coexistence of an exciton absorption peak and the gain at its tail [3]. It is essential, however, to demonstrate these effects at room temperature, because larger homogeneous broadening may change the situation. Furthermore, it is not the gain perpendicular to the quantum well but the gain along the well that is important for the laser oscillation. In this section, I describe the gain spectra at room temperature obtained with the excitation strip method [4] and discuss the exciton effect on the gain formation.

Experimental

The sample investigated here is the molecular beam epitaxial grown LD structure with a 10 nm-thick $Zn_{0.7}Cd_{0.3}Se$ single quantum well (SQW) sandwiched between n- and p-type ZnSe. $ZnS_{0.07}Se_{0.93}$ layers are utilized as cladding layers to confine the light field effectively. The sample was excited by a tunable dye laser pumped by a nitrogen laser with a pulse width of 2 ns and a repetition rate of 20 Hz. The laser beam was focused on samples to a strip-like shape of varying length. The maximum intensity was around 100 kW/cm^2, which was enough to make the sample lase at room temperature. Photoluminescence was observed from the sample edge and detected by a cryogenic CCD camera. All results described in this section were measured at room temperature.

Results

At room temperature, a green luminescence band is observed at about 2.3 eV with a full
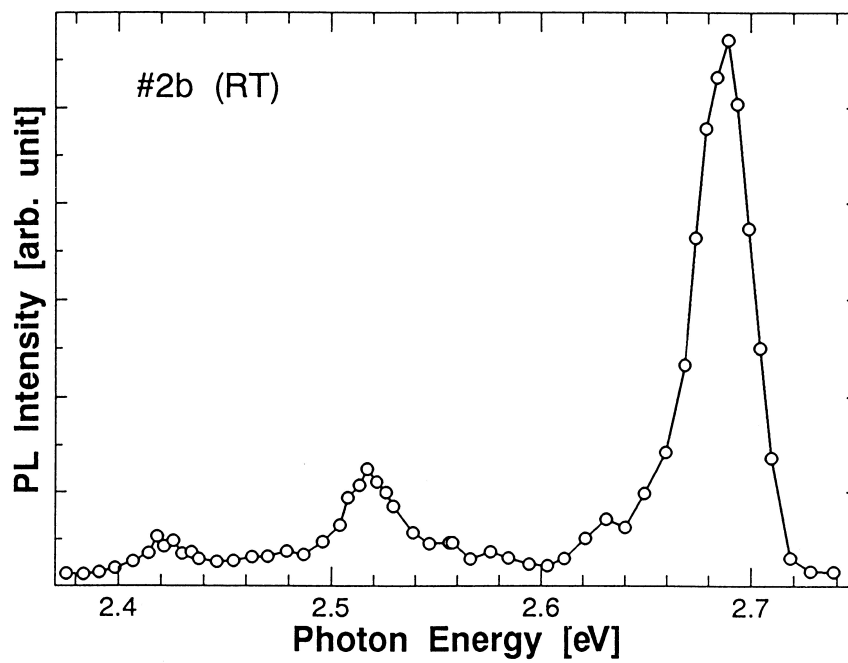
Fig. 1.10. Photoluminescence intensity from a $Zn_{0.7}Cd_{0.3}Se/ZnSe$ SQW laser structure at room temperature as a function of excitation photon energy. Pump laser intensity is around 100 kW/cm^2.

width at half-maximum of 150 meV. The peak energy blue-shifts as the excitation increases. It also depends on the length of excitation l because of the absorption or stimulation process in the course of propagation. Figure 1.10 shows photoluminescence peak intensity as a function of the excitation photon energy. Sharp peaks are observed at 2.42, 2.52 and 2.69 eV. The peak at 2.42 eV is ascribed to the exciton state in a $Zn_{0.7}Cd_{0.3}Se$ SQW, which demonstrates that the exciton effect (electron-hole correlation) is important even at room temperature. The peak at 2.69 eV corresponds to the absorption onset in ZnSe barrier layers, although it is not clear at this stage that it is due to an exciton state: strong absorption due to higher energy of band-to-band transition may block the excitation from reaching the quantum well layer. The peak at 2.52 eV is likely to stem from barrier layers but is not understood at this stage.

Photoluminescence spectra $I(E, l)$ are taken for various excitations of length l. The gain spectrum is given by

$$g(E) = \frac{1}{l}\ln\left\{\frac{I(E, 2l)}{I(E, l)} - 1\right\}. \tag{1.6}$$

Figure 1.11 shows gain spectra for $l = 200$ μm for several pump intensities. The excitation energy was 2.69 eV (the third peak of Fig. 1.10). For the lowest excitation (3%) the gain is negative in the whole range. This negative gain is nothing but the absorption due to the band tail of an exciton state at 2.42 eV. As the excitation increases, the gain shows up and the gain maximum position blue-shifts. A gain of several tens of cm^{-1} is achieved for less than 100 kW/cm^2, which is enough to have laser oscillation for a 1 mm-long cleaved cavity without coating. In fact, for edge-to-edge excitation across the same sample, laser oscillation was observed at 2.32 eV.

From this pump intensity dependence of the peak position of the gain spectrum, the cavity-length dependence of the lasing energy reported in Ref. 3 can be explained: the shorter cavity has a larger loss, which results in a higher energy of the lasing emission.

Discussion

If Coulomb interaction were not important for ZnCdSe/ZnSe quantum well structures, we would not have a sharp peak at 2.42 eV in the excitation spectrum and the gain mechanism would have to be explained in the conventional theory of semiconductor lasers. Now we
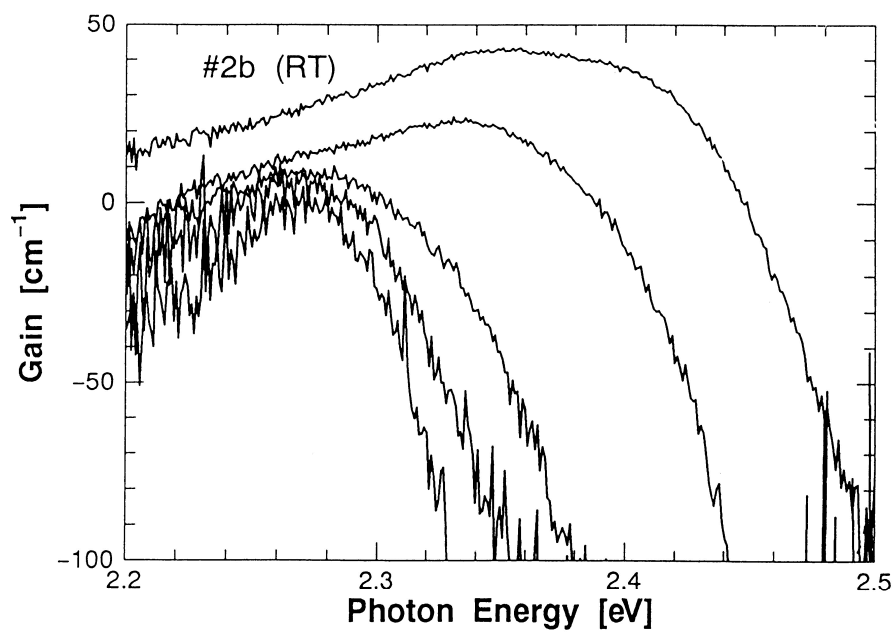
Fig. 1.11. Optical gain spectra of a $Zn_{0.7}Cd_{0.3}Se/ZnSe$ SQW laser structure for different pump intensities (100, 70, 28, 6, 3%), where the maximum intensity is around 100 kW/cm^2.

observe the exciton peak in a ZnCdSe/ZnSe SQW structure which is important even at room temperature. Assuming that the exciton was broadened only homogeneously due to phonon scattering or exciton-exciton collisions, the exciton band should give either only absorption or only gain throughout the full spectral region, depending on the excitation intensity. Since the gain region develops for higher excitation, it is conclude that the inhomogeneous broadening effect plays an important role even at room temperature. On the other hand, if there were no homogeneous broadening at all, one could expect a gain as large as the absorption coefficient for the unexcited material for the region below the chemical potential. Again, this is not the case as we can see in the gain curve for the highest excitation, where the chemical potential exceeds the exciton absorption peak. I would like to emphasize, however, that laser oscillation occurs 100 meV below the exciton absorption peak for a 1 mm-long cavity. It shows the coexistence of gain and absorption in an inhomogeneously broadened exciton band.

Conclusion

Gain formation was confirmed at the exciton tail region, which can be explained in terms of the phase-space filling effect on an inhomogeneously broadened exciton state.

References in 1.3

[1] M. A. Haase, J. Qiu, J. M. DePuydt, and H. Cheng, *Appl. Phys. Lett.* **59**, 1272 (1991).

[2] H. Jeon, J. Ding, W. Patterson, A. V. Nurmikko, W. Xie, D. C. Grillo, M. Kobayashi, and R. L. Gunshor, *Appl. Phys. Lett.* **59**, 3619 (1991).

[3] J. Ding, M. Hagerott, T. Ishihara, H. Jeon, and A. V. Nurmikko, *Phys. Rev. B* **47**, 10528 (1993).

[4] K. L. Shaklee, R. E. Nahory, and R. F. Leheny, *J. Lumin.* **7**, 284 (1973).

1.4. Electrically pumped ZnCdSe/ZnSe vertical-cavity surface-emitting lasers

Introduction

Vertical-cavity surface-emitting lasers (VCSELs) have recently attracted much attention because of their surface-normal operation, potential for extremely low threshold currents, and the ease with which they may be fabricated in closely spaced and two-dimensional arrays and integrated with other devices such as transistors for photonic switching applications [1-5]. Output characteristics such as narrow divergence beams and operation in a single longitudinal mode, due to the large mode spacing in a short cavity, are additional advantages.

ZnSe-based wide bandgap II-VIs are promising materials for use in blue laser diodes. Starting with the first demonstration of blue-green laser diodes, further developments have led to continuous-wave operation at room temperature and low-threshold-current pulsed operation [6-9]. Recently, fabrication of a ZnSe-based vertical cavity using SiO_2/TiO_2 reflectors was reported [10]. Optically pumped operation of the blue-green VCSEL has also been achieved [11], however, current injection has not been reported. This study is the first results of the characterization of blue-green II-VI VCSELs by electrical pumping techniques.

Device structure and fabrication

The VCSEL structures were composed of a ZnCdSe/ZnSe multiple quantum well (MQW) active layer, n- and p-ZnSe cladding layers and two SiO_2/TiO_2 distributed Bragg reflectors (DBRs). The detailed schematic diagram of the fabricated VCSEL structure is shown in Fig. 1.12. The ZnCdSe/ZnSe epitaxial layers were grown by molecular beam epitaxy. The II-VI heterostructures were grown on a (100) n-GaAs substrate and consisted of an n-ZnSe cladding layer (1.5 μm), an MQW of quadruple 6 nm-thick $Zn_{1-X}Cd_XSe$ ($X = 0.2$) quantum wells and 50 nm-thick ZnSe barriers, and a p-ZnSe cladding layer (1.5 μm). Nitrogen radical doping and Cl doping were employed to obtain p- and n-ZnSe layers, respectively. Carrier concentrations of both p- and n-ZnSe layers are about 2×10^{17} cm^{-3}. The growth temperature was 270°C. The composition X of the $Zn_{1-X}Cd_XSe$ alloy was determined by assuming a linear variation of the lattice constant with X (Vegard's law).
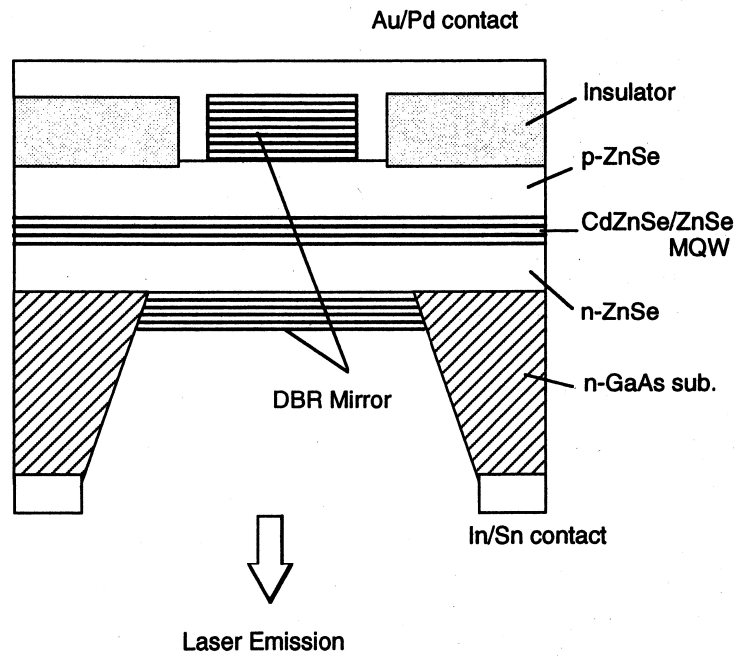
Fig. 1.12. Schematic diagram of a ZnCdSe/ZnSe blue-green vertical-cavity surface-emitting laser structure.
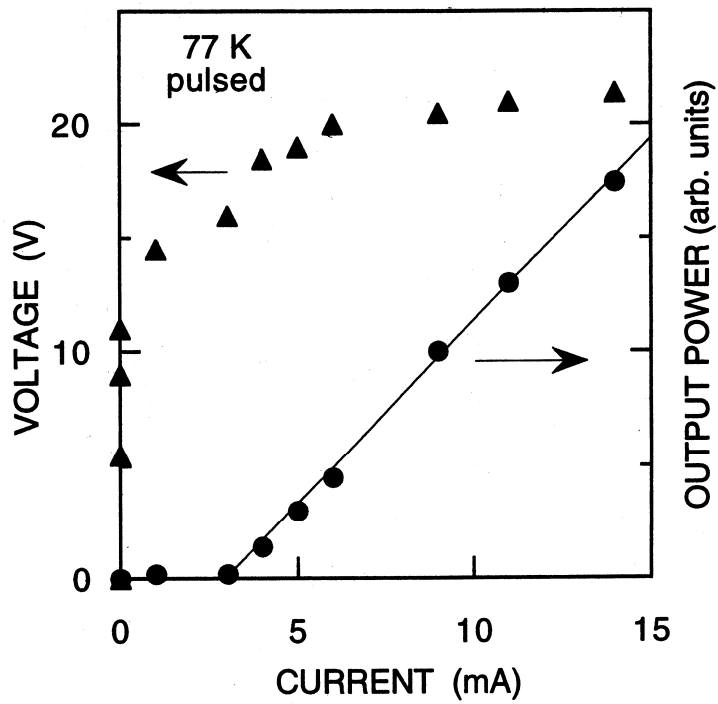

Fig. 1.13. *L-I* and *V-I* characteristics for a blue-green VCSEL at 77 K under pulsed operation.

The DBRs were fabricated from SiO_2/TiO_2 quarter-wave ($\lambda/4$) layers by rf sputtering. The SiO_2/TiO_2 multilayers were deposited on both the light output and opposite sides. The first circular DBR (8 periods, 10 μm in diameter) was deposited on the top p-ZnSe layer using lift-off. Next, an insulator was used to define the annulus contact area of Pd/Au evaporated on the top p-ZnSe layer. The outer diameter of the annulus Pd/Au p-contact around the circular DBR was 14 μm. Since the GaAs substrate is only transparent for wavelengths longer than 900 nm, the light output windows were opened in the GaAs substrate side by selective wet etching using $NH_4OH-H_2O_2$ solution with approximately 20:1 selectivity between GaAs and ZnSe. After the n-GaAs substrate side was polished and etched to 150 μm in thickness, the circular light output windows (100 μm in diameter) were formed by this selective wet etching technique and photolithography. Then, a second SiO_2/TiO_2 DBR (5 periods) mirror was deposited on the n-ZnSe layer through the windows. In/Sn was used as the n-metal contact to the n-GaAs substrate. Finally, the wafer was diced to form the laser chips.

The reflectance spectra were measured in the DBR structure. The measured reflectivity of the SiO_2/TiO_2 dielectric mirrors with 8 pairs was greater than 99%. The measured mirror center near 480 nm and the Fabry-Perot resonance were in good agreement with the calculated results assuming that the refractive indexes of SiO_2 and TiO_2 are 1.46 and 2.73, respectively.

Electrical pumping characterization

The VCSEL devices were characterized at 77 K under pulsed operation. The devices were tested by clamping the samples to a copper heat sink and directly probing the laser chips. The pulse width was 0.5 μs with a repetition rate of 1 kHz. The light output versus current (*L-I*) and voltage versus current (*V-I*) characteristics are shown in Fig. 1.13. The steep rise of the emission indicates lasing. A very low threshold current of 3 mA was obtained in the VCSEL. The threshold current density of these devices is 3.9 kA/cm^2, which is as low as the value for the edge-emitting ZnCdSe/ZnSe lasers. The operating voltage is 17 V, which should be greatly improved with an optimized contact structure. Figure 1.14 shows the emission spectra obtained in the vertical direction below and above the threshold at 77 K. Spectral narrowing was observed due to lasing. The full width at half-maximum of the lasing spectrum is about 0.9 nm above the threshold. Single-longitudinal-mode operation was obtained. The lasing wavelength is
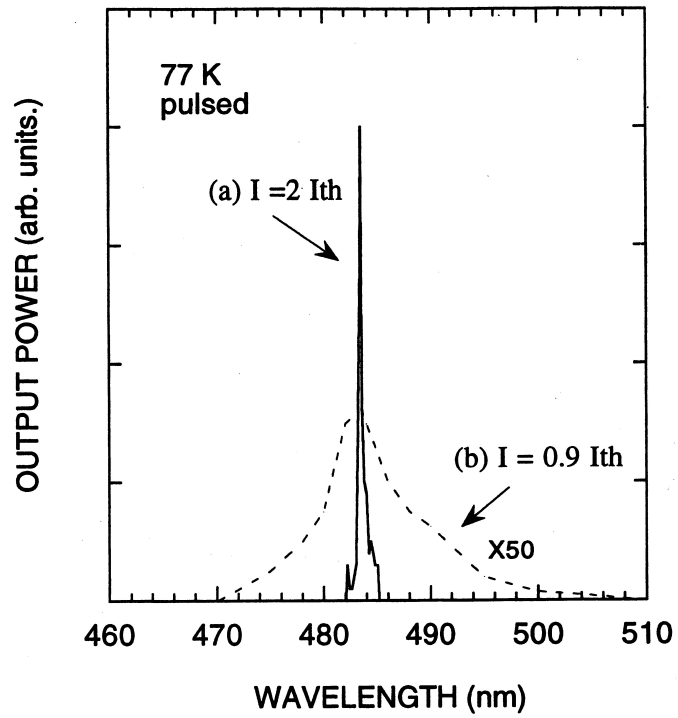
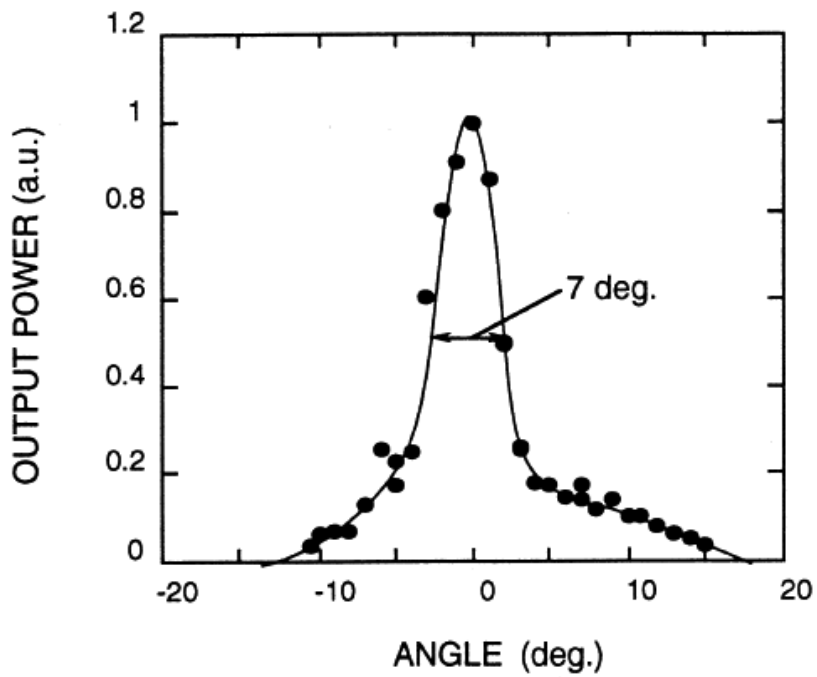Fig. 1.14. (a) Lasing and (b) spontaneous emission spectra at 77 K under pulsed operation.

Fig. 1.15. Far-field pattern of the blue-green VCSEL with 10 μm-diameter.

36

484 nm under pulsed operation.

The far-field pattern of the lasing mode obtained at 77 K is shown in Fig. 1.15. The far-field radiation angle is as narrow as 7° above the threshold, which is in good agreement with the calculated results [5] and indicates the spatial coherence expected for VCSEL emission.

Conclusion

Electrically pumped lasing from a ZnCdSe/ZnSe blue-green VCSEL was demonstrated for the first time. Lasing was achieved at a wavelength of 484 nm at 77 K with a very low threshold current of 3 mA. The far-field radiation angle was as narrow as 7° above threshold, which indicates the spatial coherence expected for VCSEL emission. This work opens the door to a broad range of new device applications of II-VI materials.

References in 1.4

[1] J. L. Jewell, J. P. Harbison, A. Scherer, Y. H. Lee, and L. T. Florez, *J. Quantum Electron.* **QE-27**, 1332 (1991).

[2] J. L. Jewell, A. Scherer, S. L. McCall, Y. H. Lee, S. Walker, J. P. Harbison, and L. T. Florez, *Electron. Lett.* **25**, 1123 (1989).

[3] R. S. Geels, S. W. Corzine, and L. A. Coldren, *J. Quantum Electron.* **QE-27**, 1359 (1991).

[4] C. Lei, T. J. Rogers, D. G. Deppe, and B. G. Streetman, *Appl. Phys. Lett.* **58**, 1122 (1991).

[5] H. Soda, Y. Motegi, and K. Iga, *J. Quantum Electron.* **QE-19**, 1035 (1983).

[6] M. A. Haase, J. Qju, J. M. DePuydt, and H. Cheng, *Appl. Phys. Lett.* **59**, 1272 (1991).

[7] J. M. Gaines, R. R. Drenten, K. W. Haberern, T. Marshall, P. Mensz, and J. Petruzzello, *Appl. Phys. Lett.* **62**, 2462 (1993).

[8] N. Nakayama, S. Itoh, H. Okuyama, M. Ozawa, T. Ohata, K. Nakano, M. Ikeda, A. Ishibashi, and Y. Mori, *Electron. Lett.* **29**, 1488 (1993).

[9] A. Salokatve, H. Jeon, J. Ding, M. Hovinen, A. V. Nurmikko, D. C. Grillo, L. He, J. Han, Y. Fan, M. Ringle, R. L. Gunshor, G. C. Hua, and N. Otsuka, *Electron. Lett.* **29**, 2192 (1993).

[10] T. Honda, K. Yanashima, J. Yoshino, H. Kukimoto, F. Koyama, and K. Iga, *Jpn. J. Appl. Phys.* **33**, 3960 (1994).

[11] P. D. Floyd, J. K. Furdyna, H. Luo, J. L. Merz, Y. Yamada, and T. Yokogawa, *Appl. Phys.*

Lett. **66**, 2929 (1995).

1.5. Real index-guided blue-green LDs with small beam astigmatism fabricated using ZnO buried structure

Introduction

Short-wavelength laser diodes (LDs) have attracted much attention regarding applications for high-density optical disk memories and laser printers. Small beam astigmatism in laser characteristics is very important for these applications to enable effective focusing of the laser beam on the smallest spot. The real index-guiding effect in buried ridge structure is useful for realizing a smaller beam astigmatism and stable fundamental transverse mode oscillation.

ZnSe-based wide-bandgap II-VI compounds are promising materials for use in blue-green LDs. Since the first demonstration of II-VI blue-green LDs [1] further development has led to continuous-wave operation at room temperature [2,3]. Recently, some efforts were made to reduce the threshold current using index-guided structure [4,5]. However, there are no reports on lateral far-field characteristics and beam astigmatism in real index-guided II-VI LDs. Zinc oxide with low refractive index and high resistivity is useful as a buried material in real index-guided ridge LDs. ZnO also has higher thermal conductivity compared with conventional insulators such as SiO_2 or SiN_X. In this section, a real index-guided blue-green LD with small beam astigmatism has been demonstrated for the first time by using a ZnO buried layer and the electron cyclotron resonance (ECR) plasma etching technique. Stable fundamental transverse mode oscillation was also obtained.

Experimental

The laser structures were composed of a ZnCdSe/ZnSSe/ZnMgSSe separate confinement heterostructure (SCH). The epitaxial layers were grown by compound-source molecular beam epitaxy on a GaAs (100) substrate [6] and consisted of an n-ZnMgSSe cladding layer (1.2 μm), an n-ZnSSe guiding layer (0.12 μm), an active layer of 6 nm $Zn_{0.8}Cd_{0.2}Se$ quantum well, a p-ZnSSe guiding layer (0.12 μm), and a p-ZnMgSSe cladding layer (0.74 μm). Nitrogen radical doping and Cl doping were employed to obtain p- and n-type layers, respectively. The p-doping levels of p-ZnMgSSe, p-ZnSSe and p-ZnSe were 2×10^{17} cm^{-3}, 4×10^{17} cm^{-3} and 5×10^{17} cm^{-3}, respectively. The n-doping level was 5×10^{17} cm^{-3}. The growth temperature was 270°C. The
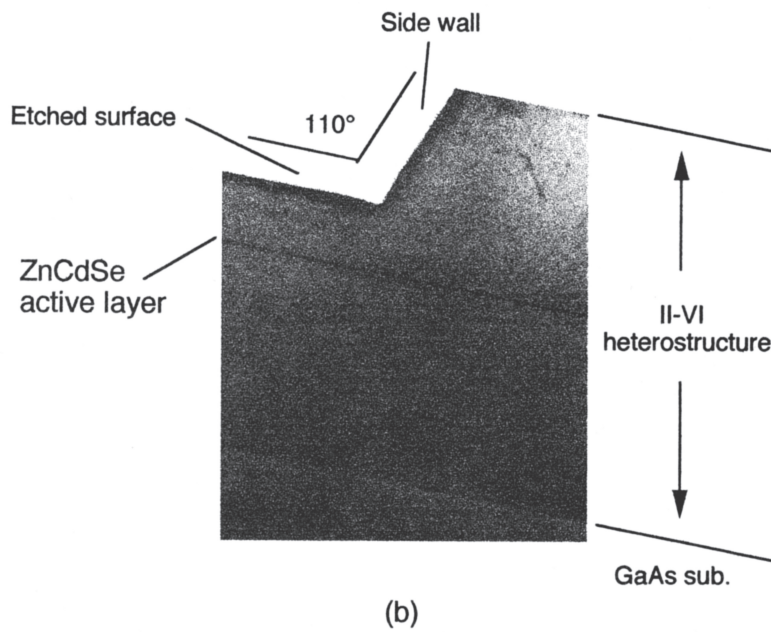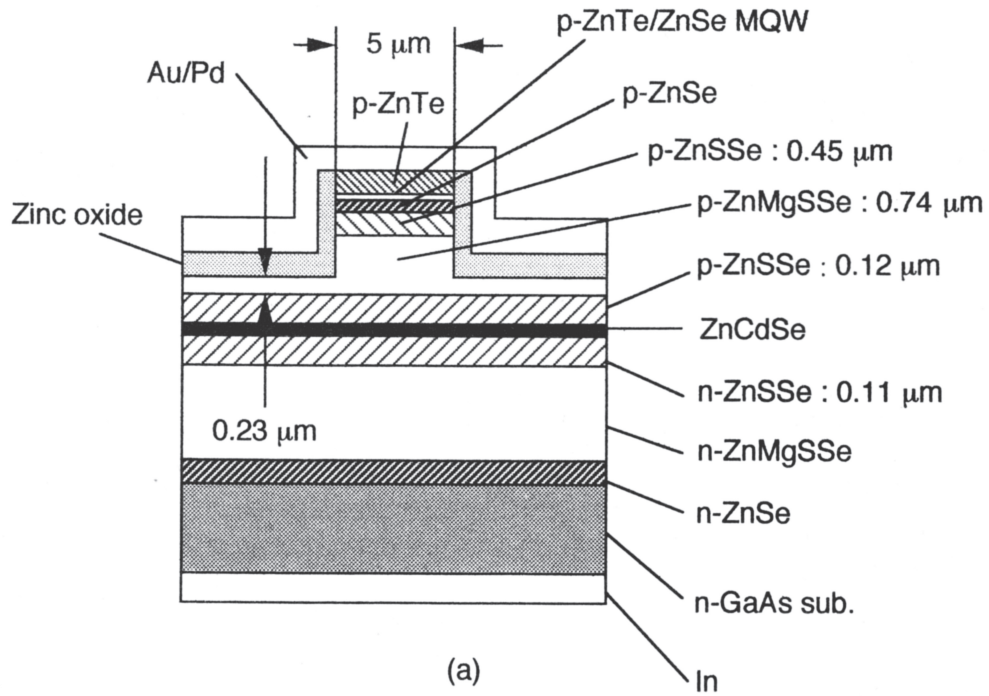
Fig. 1.16. (a) Schematic structure of the ZnCdSe/ZnSSe/ZnMgSSe SCH index-guided LD.
(b) Bright-field cross-sectional view TEM micrograph of the etched laser structure.

40

schematic structure of the ZnCdSe/ZnSSe/ZnMgSSe SCH ridge waveguide laser is shown in Fig. 1.16(a).

Ridge stripe structures were fabricated using a load-locked ECR plasma etching system. Cl_2/H_2 discharge was used for dry etching of the laser structure. Typical flow rates of Cl_2 and H_2 were 5 sccm and 4 sccm, respectively. The total gas pressure was 1×10^{-3} Torr. The applied microwave power was 200 W, and the applied bias voltage was 300 V.

Results and discussion

Figure 1.16(b) shows a bright-field cross-sectional view transmission electron microscopy (TEM) image of the etched ridge waveguide laser. The anisotropic etching behavior under the above condition enabled us to achieve a nearly vertical mesa side wall (20° incline from the surface normal) and a smooth surface, as shown in Fig. 1.16(b). The II-VI layers were etched to the 0.23 μm thickness of p-ZnMgSSe. No dislocations and no stacking faults were observed in the etched surface of p-ZnMgSSe. The depth of the damaged region was estimated to be less than 30 nm by this TEM analysis. With increasing applied bias voltage, the inclination of the mesa side wall from the surface normal approached 0° (a vertical mesa), but the depth of damaged region increased. Therefore, the applied bias voltage of 300 V was used in this study. The 30 nm-thick damaged region was removed by wet etching using HCl-H_2O solution.

The zinc oxide buried layer with the refractive index of 2.05 was used for the lateral mode and carrier confinement. The ZnO layer was deposited at room temperature by rf sputtering and had resistivity higher than 1×10^6 Ωcm. The total pressure of Ar was 1×10^{-2} Torr and a low rf power of 50 W was used to suppress damage to the II-VI material by ion bombardment. The buried ridge structure was formed by depositing ZnO on the etched p-ZnMgSSe region using the lift-off process, as shown in Fig. 1.16(a). The typical thickness of the ZnO layer was 0.2 μm. Pd/Au and In were used as p-metal contact to p-ZnTe and n-metal contact to n-GaAs substrate, respectively.

Gain-guided lasers were also fabricated using the same laser wafer for comparison with the ridge waveguide laser. In the gain-guided laser, only the top p-ZnTe contact layer (30 nm thick) and the p-ZnTe/ZnSe MQW were chemically etched off, leaving a 5 μm-wide contact stripe region to reduce the current spreading. A ZnO layer was used as an insulator to define the
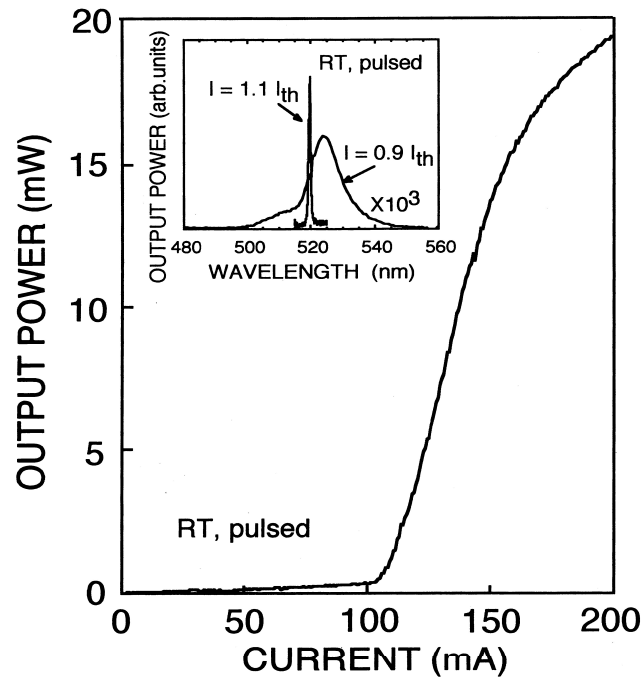
Fig. 1.17. Light output power versus injection current characteristics for the ZnO buried ridge waveguide laser at room temperature under pulsed operation. The inset shows stimulated and spontaneous emission spectra.
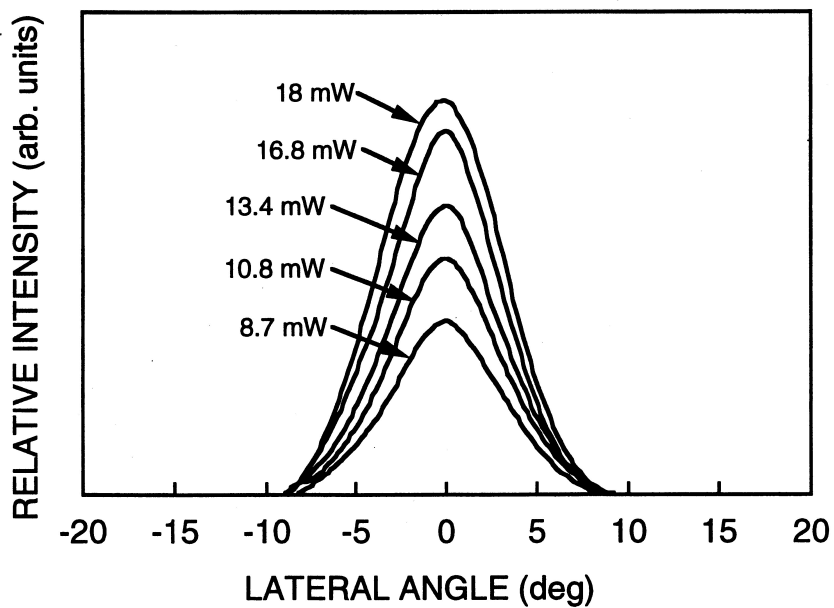

Fig. 1.18. Lateral far-field characteristics for a ZnO buried laser with a 5μm-wide ridge.

contact area of the Pd/Au electrode.

The devices were characterized at room temperature under pulsed operation. The pulse width was 700 ns with a repetition rate of 1 kHz. The light output versus current (*L-I*) and emission spectra are shown in Fig. 1.17. The *L-I* curve was kink-free to greater than 200 mA, and the threshold current was 100 mA. The inset shows stimulated and spontaneous emission spectra. Lasing wavelength was 520 nm above the threshold. The far-field pattern of the lasing mode was investigated. The pulsed lateral far-field characteristics for the laser with a 5 μm-wide ridge are shown in Fig. 1.18. The output beam was anastigmatic and had constant far-field full angle at half-maximum for a wide range of injected currents, indicating real index guiding in the lateral direction. The consistent shape of the lateral curves for the various injected currents implies single lateral mode operation at up to 18 mW for this device. The lateral far-field radiation angle was as narrow as 7° above the threshold.

Figure 1.19 shows beam spot size near the laser mirror facet in the direction parallel to the junction plane measured at an output power of 3 mW. The beam astigmatism is the distance between the beam waist and the facet position. The beam astigmatism value for the ridge waveguide laser was measured to be less than 0.5 μm as a result of the real index-guided structure, in contrast to 25 μm for the gain-guided laser. This small beam astigmatism is evidence for the index-guided blue-green laser.

Conclusion

A real index-guided blue-green LD with small beam astigmatism of less than 0.5 μm was demonstrated for the first time. The laser showed stable fundamental transverse mode oscillation with beam divergence of 7° in the direction of the junction plane.
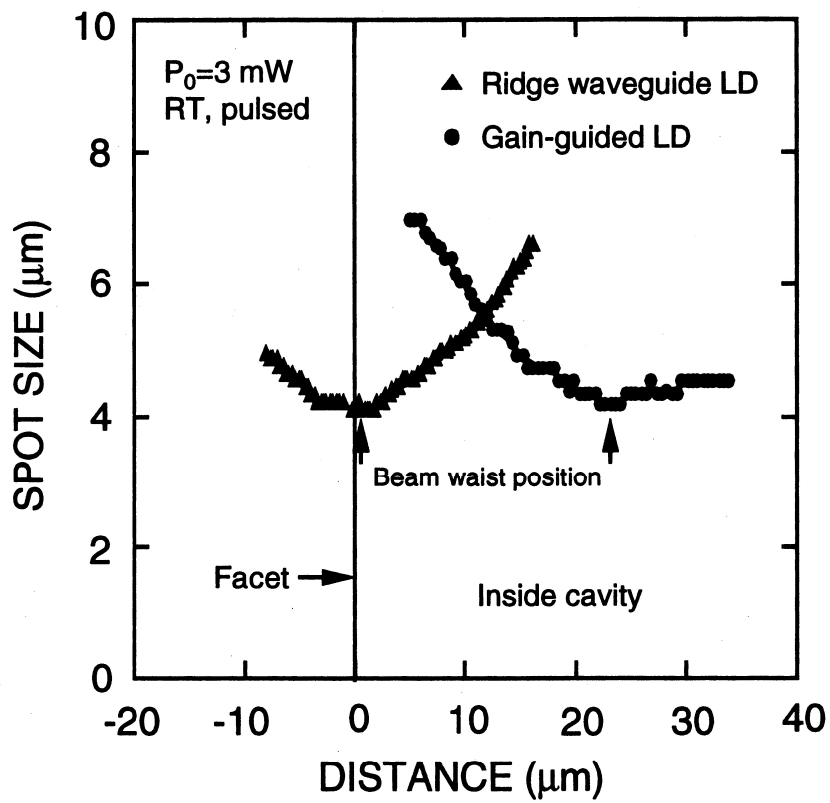
Fig. 1.19. Beam spot size near the LD mirror facet in the direction parallel to the junction plane measured at an output power of 3 mW. The beam astigmatism is the distance between the beam waist and the facet position. It was measured to be less than 0.5 μm for the ridge waveguide LD.

References in 1.5

[1] M. A. Haase, J. Qju, J. M. DePuydt, and H. Cheng, *Appl. Phys. Lett.* **59**, 1272 (1991).

[2] N. Nakayama, S. Itoh, H. Okuyama, M. Ozawa, T. Ohata, K. Nakano, M. Ikeda, A. Ishibashi, and Y. Mori, *Electron. Lett.* **29**, 1488 (1993).

[3] A. Salokatve, H. Jeon, J. Ding, M. Hovinen, A. V. Nurmikko, D. C. Grillo, L. He, J. Han, Y. Fan, M. Ringle, R. L. Gunshor, G. C. Hua, and N. Otsuka, *Electron. Lett.* **29**, 2192 (1993).

[4] M. A. Haase, P. F. Baude, M. S. Hagedorn, J. Qiu, J. M. DePuydt, H. Cheng, S. Guha, G. E. Hofler, and B. J. Wu, *Appl. Phys. Lett.* **63**, 2315 (1993).

[5] T. Kawasumi, N. Nakayama, A. Ishibashi, and Y. Mori, *Electron. Lett.* **31**, 1667 (1995).

[6] K. Ohkawa, S. Yoshii, H. Takeishi, A. Tsujimura, S. Hayashi, T. Karasawa, and T. Mitsuyu, *Jpn. J. Appl. Phys.* **33**, L1673 (1994).

Chapter 2

Fabrication and characterization of GaN-based LDs and LEDs

2.1. Simulation of crystal growth for GaN metal organic vapor phase epitaxy

Introduction

Gallium nitride (GaN) has been confirmed as a key material for achieving violet laser diodes (LDs) through recent splendid development [1,2]. Metalorganic vapor phase epitaxy (MOVPE) is a leading technology for this purpose. This technology is, however, not a satisfactory level for high power commercial LDs from the standpoint of crystal quality itself and the overall epitaxy process control. Numerical calculation is one of the powerful tools for analyzing the physical and chemical mechanism and finding the pathway to an optimal process condition. In this section, three-dimensional simulations of gas flow and chemical reactions are made in a horizontal reactor for GaN MOVPE. Attention is paid to the effect of the gas flow velocity and gas pressure on the spatial distribution of both streamlines and the surface reaction rate.

Simulation Model

Figure 2.1(a) shows a bird's-eye view of the model reactor geometry. Figure 2.1(b) shows the cross-sectional view of the reactor around the susceptor portion on the symmetry plane of $y = 0$ m, where gas flow vectors are also shown as an example. This is a two-split-flow reactor with a linear expansion entrance region of 10.4° tapering angle. The length (x-direction), the width (y-direction) and the height (z-direction) of the reactor are 0.6 m, 0.1 m and 0.014 m, respectively. The reactor wall is made of quartz. The quartz wall has a uniform thickness of 2 mm. The gas inlet and the flow channel in the expansion region are composed of upper and lower parts with each 4mm in height. The channel height in the reaction region is 10 mm. From the upper and the lower inlets, trimethylgallium (TMG, *i.e.* Ga(CH$_3$)$_3$) diluted by mixed N$_2$-H$_2$ carrier gas and NH$_3$ are fed, respectively. They are confluent at the mixing plane. Both the molar ratios of N$_2$: H$_2$ and N$_2$-H$_2$: NH$_3$ are 1:1. The V/III ratio is 10000. The rectangular susceptor is
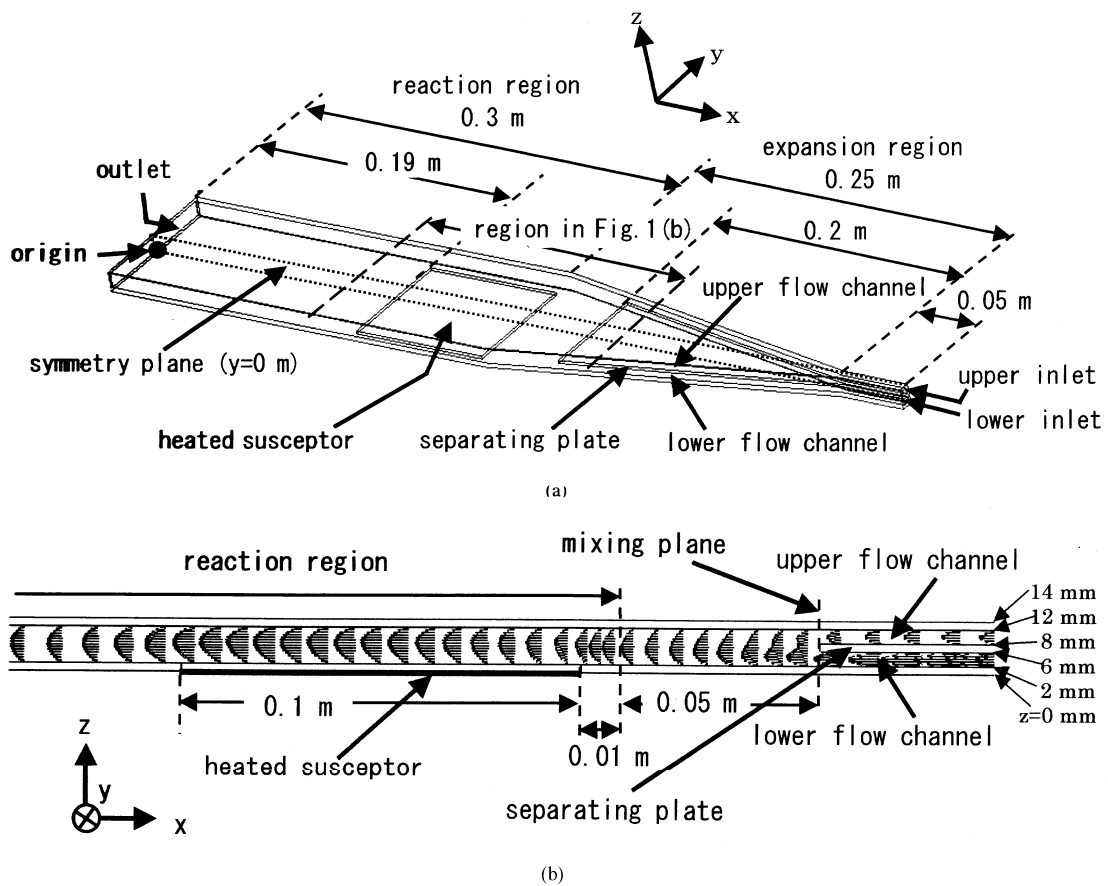
Fig. 2.1. (a) Bird's-eye view of the model reactor geometry. The "origin" denotes $x = 0$ m, $y = 0$ m and $z = 0$ m. (b) Cross-sectional view of the reactor around the susceptor portion on the symmetry plane of $y = 0$, where gas flow vectors are also shown as an example. The region shown in this figure is specified in Fig. 2.1(a).

placed on the bottom in the reaction region.

The formulation consists of conservation equations for the total mass, momentum, energy and individual gas-phase species under a laminar and compressive fluid model. These equations are approximated by a control volume based finite element method with a collocated mesh. At the inlet, uniform flow velocity v_x parallel to the x direction is assigned. At the outlet, the gas pressure is specified. Constant temperatures of 1300 K and 310 K are given across the susceptor surface and on the cold wall, respectively.

Transport properties of viscosity, thermal conductivity and diffusion coefficient for the gas mixture are modeled as a function of the local values of temperature and mole fraction [3,4].

The surface reaction mechanism for GaN growth is summarized in Table 2.1 [5]. The mechanism consists of chemisorption reactions [S1]-[S6] and growth reactions [S7]-[S8]. Two kinds of gas-phase radicals, Ga* and GaN*, are responsible for epitaxy. We assume that NH$_X$ is in excess and Ga* itself becomes molecular Ga-N just above the surface. Table 2.2 shows the mechanism modified for the present use by combining one of chemisorption reactions ([S1]-[S6]) and corresponding growth reaction ([S7] or [S8]). The growth reaction proceeds along the c-axis in wurtzite structure, that is, perpendicular to the (0001) surface. There is one dangling bond per either surface atom (Ga or N) whose total concentration S_0 is 1.135×10^{19} m^{-2}. Firstly, the surface coverage $\theta = \{[\text{GaN}]^{\text{Ga}} + [\text{GaN}]^{\text{GaN}}\}/S_0$ must be determined by equating consumption and generation rates of free sites. Here $[\text{GaN}]^{\text{Ga}}$ and $[\text{GaN}]^{\text{GaN}}$ (m^{-2}) are the concentration of adsorbed molecular Ga-N on the surface originated from Ga* and GaN*, respectively. The consumption rate C of free sites by collision and adsorption of Ga-N originated by Ga* or GaN* is given in the following form:

$$
\begin{aligned}
C^{\text{Ga}} &= (1-\theta)(R_1^* + R_2^* + R_3^*); \\
C^{\text{GaN}} &= (1-\theta)(R_4^* + 3R_5^*)
\end{aligned}
\tag{2.1}
$$

with

$$
R_j^* = \sqrt{\frac{RT}{2\pi M_j}}\, Y_j \sigma_j .
\tag{2.2}
$$

Here, R_j* is the chemisorption reaction rate for $\theta = 0$, R the gas constant, T the gas temperature, M_j the molecular weight of incoming species, Y_j the mole concentration, and σ_j the sticking coefficient. Index j corresponds to the modified surface reaction of type [Sj'] in Table 2.2. The

Table 2.1. Original surface reaction mechanism of GaN growth from TMG and NH_3 by Mihopoulos [5]. Here, S denotes the free site.

reaction		σ	k_0 $(m^2/mol\ s)$	E_a (kcal/mol)
[S1] $Ga(CH_3)_3 + S$	$\rightarrow$ $Ga^* + 3\ CH_3$	0.1	–	0.0
[S2] $Ga(CH_3)_3 : NH_3 + S$	$\rightarrow$ $Ga^* + 3\ CH_3 + NH_3$	0.1	–	0.0
[S3] $GaCH_3 + S$	$\rightarrow$ $Ga^* + CH_3$	1.0	–	0.0
[S4] $Ga(CH_3)_2NH_2 + S$	$\rightarrow$ $Ga^* + 2\ CH_4$	1.0	–	0.0
[S5] "Ga–N" $+ S$	$\rightarrow$ GaN^*	1.0	–	0.0
[S6] $[Ga(CH_3)_2NH_2]_3 + 3S$	$\rightarrow$ $3\ GaN^* + 6\ CH_4$	1.0	–	0.0
[S7] Ga^*	$\rightarrow$ $[GaN]_s + S$	–	1.0×10^6	37.0
[S8] GaN^*	$\rightarrow$ $[GaN]_s + S$	–	2.0×10^4	22.0

Table 2.2. Modeled surface reaction mechanism of GaN growth for the present use modified from Table 2.1.

reaction

[S1'] $(1/2)N_2 + Ga(CH_3)_3$	$\rightarrow$ $[GaN]_s + 3CH_3$
[S2'] $(1/2)N_2 + Ga(CH_3)_3 : NH_3$	$\rightarrow$ $[GaN]_s + 3CH_3 + NH_3$
[S3'] $(1/2)N_2 + GaCH_3$	$\rightarrow$ $[GaN]_s + CH_3$
[S4'] "Ga–N"	$\rightarrow$ $[GaN]_s$
[S5'] $[Ga(CH_3)_2NH_2]_3$	$\rightarrow$ $3[GaN]_s + 6CH_4$

k_0 $(m^2/mol\ s)$	E_a (kcal/mol)	(J/mol)	σ_j	R_j^*	R_j	remarks
1.0×10^6	37.0	1.55×10^5	0.1	R_1^*	R_1	[S1] + [S7]
1.0×10^6	37.0	1.55×10^5	0.1	R_2^*	R_2	[S2] + [S7]
1.0×10^6	37.0	1.55×10^5	1.0	R_3^*	R_3	[S3] + [S7]
2.0×10^4	22.0	9.21×10^4	1.0	R_4^*	R_4	[S5] + [S8]
2.0×10^4	22.0	9.21×10^4	1.0	R_5^*	R_5	[S6] + [S8]

generation rate G of free sites by the growth reaction due to Ga* or GaN* is given in the following form:

$$G^{\text{Ga}} = \theta\, k_0^{\text{Ga}} \exp\left(-\frac{E_a^{\text{Ga}}}{RT}\right)[\text{GaN}]^{\text{Ga}} ;$$

$$G^{\text{GaN}} = \theta\, k_0^{\text{GaN}} \exp\left(-\frac{E_a^{\text{GaN}}}{RT}\right)[\text{GaN}]^{\text{GaN}} .$$

$$(2.3)$$

The coverage θ is then determined by the following equations:

$$C^{\text{Ga}} = G^{\text{Ga}} ; \qquad C^{\text{GaN}} = G^{\text{GaN}} .$$

$$(2.4)$$

Secondly, the growth reaction rate R_j [mol/sm^2] for modified reaction [Sj'] (see Table 2.2) is calculated by

$$R_j = \sqrt{\frac{RT}{2\pi M_j}}\, Y_j \sigma_j (1-\theta).$$

$$(2.5)$$

Finally, the total growth rate R_t (m/s) for GaN is evaluated by

$$R_t = \frac{M_{\text{GaN}}}{\rho_{\text{GaN}}} \sum_{j=1}^{5} R_j ,$$

$$(2.6)$$

where M_{GaN} (kg/mol) and $\rho_{\text{GaN}} = 6095$ kg/m^3 are the molecular weight and the density of GaN crystal, respectively.

Results and discussion

Four combinations of flow velocity v_x at inlets and pressure P in the reactor are examined: (a) 5.0 m/s, 40 kPa; (b) 2.5 m/s, 40 kPa; (c) 5.0 m/s, 80 kPa; (d) 2.5 m/s, 80 kPa. The average flow velocity above the susceptor and the gas flow rate Q for these cases are: (a) 0.433 m/s, 3.339 slm (standard liter per minute); (b) 0.216 m/s, 1.670 slm; (c) 0.433 m/s, 6.679 slm; (d) 0.216 m/s, 3.339 slm.

Figure 2.2 shows the plan view of the spatial distribution of growth rate R_t on the susceptor for the four cases. It is seen that the growth rate distribution is strongly dependent on Q. At an optimum Q in Fig. 2.2(a), the distribution is spatially uniform. Figure 2.2(b) is the case of low Q whose value is the half of that in Fig. 2.2(a). The peak position of the growth rate shifts in the upstream direction. That is, radicals Ga* and GaN* are largely consumed there. Figure 2.2(c) is the case of high Q whose value is twice of that in Fig. 2.2(a). The distribution is a split one with
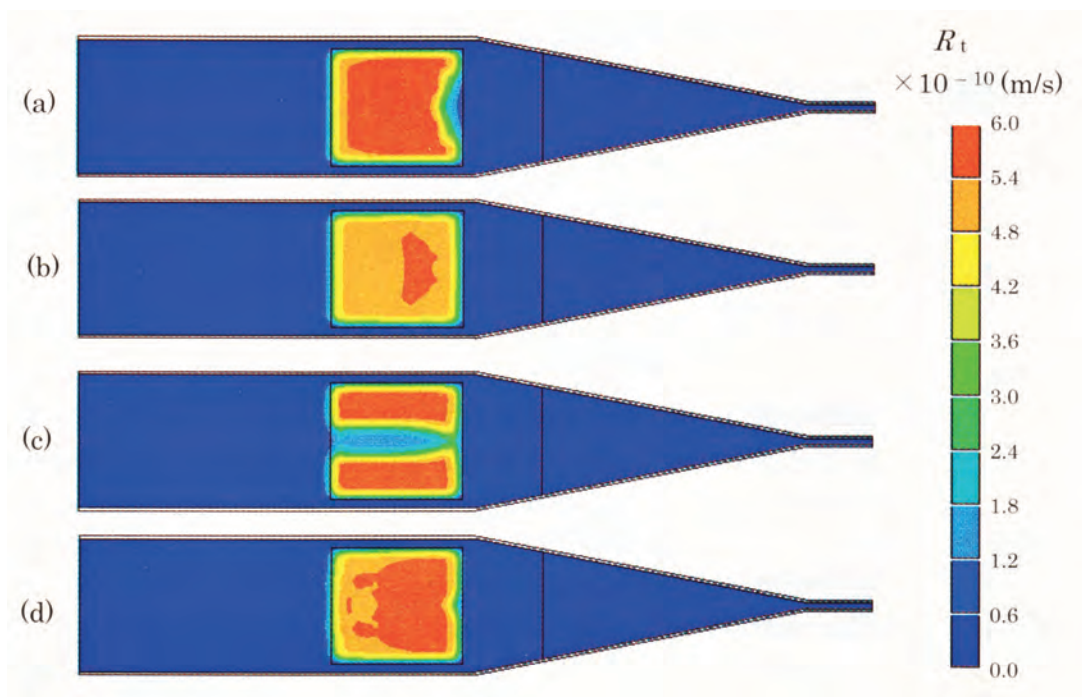
51

Fig. 2.2. Computational result for the growth rate distribution above the susceptor. Four kinds of combinations of the gas flow velocity at the inlet and the gas pressure are examined: (a) 5.0 m/s, 40 kPa (300 Torr); (b) 2.5 m/s, 40 kPa; (c) 5.0 m/s, 80 kPa (600 Torr); (d) 2.5 m/s, 80 kPa.
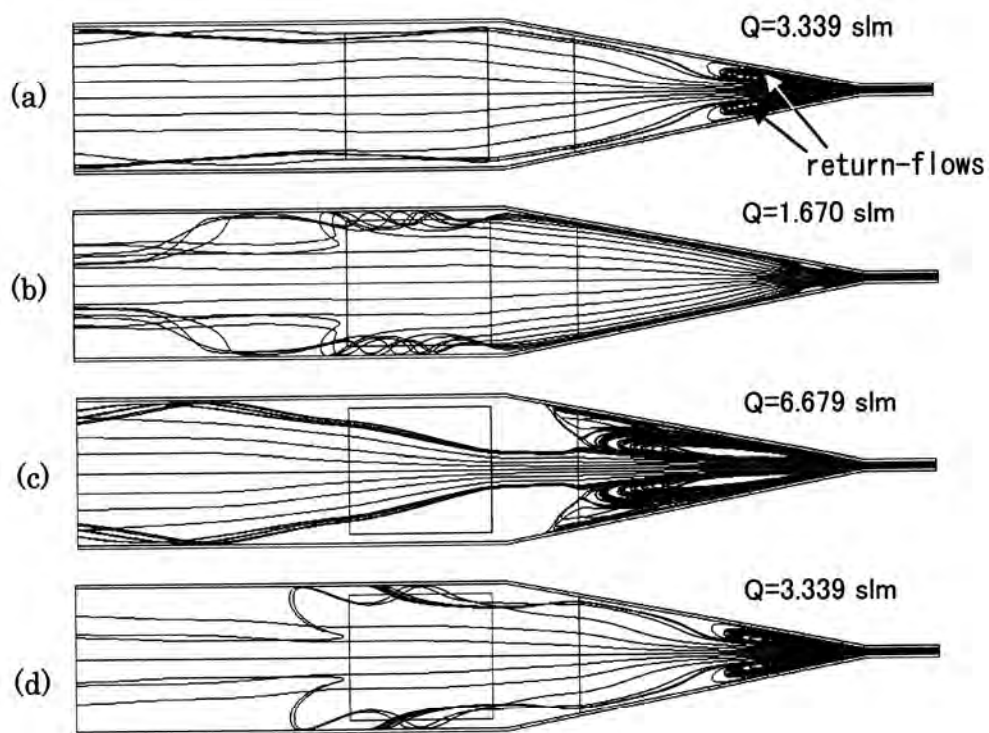
Fig. 2.3. Computational result for the plan view for streamlines passing through the line at $z = 4$ mm (the mid-height of the lower flow channel) on the plane of $x = 0.5$ m. The four cases shown in Fig. 2.2 are examined.

respect to the reactor symmetry plane. Figure 2.2(d) is the case where the flow rate is identical to that in Fig. 2.2(a). The distribution is comparatively uniform.

Figure 2.3 shows the streamlines passing through the line at $z = 4$ mm (the mid-height of the lower flow channel) on the plane of $x = 0.5$ m for the four cases. In Fig. 2.3(a), streamlines are spatially uniform above the susceptor, though there is a pair of return-flows near the gas entrance of the expansion region. As Q increases, the size of return-flows is larger, and the channel width of gas flow is substantially decreased there. As a result, the flow velocity near the symmetry plane is larger. Then, the colder gas is supplied densely near the symmetry plane above the susceptor, and causes the split distribution of the growth shown in Fig. 2.2(c). Note that the growth rate distribution in Fig. 2.2(d) resembles that in Fig. 2.2(a), though the latter is more uniform than the former. The size and the shape of return-flows are similar to each other. In these two cases of (a) and (d), the gas flow rates are identical. That is, Q is proportional to both P and v_x, and the product of Pv_x in the case of (a) is equal to that in the case of (d). The gas flow rate Q seems to be a key parameter which significantly controls the spatial distribution of the growth rate. Figure 2.3(b) shows very small return-flows and uniform streamlines above the susceptor. This case has, however, too small supply of Ga* and GaN* above the susceptor to achieve uniform growth. Either a tilted susceptor or a vertically tapered tube is expected to compensate for the depletion in the downstream region above the susceptor.

Conclusion

Three-dimensional simulations of complex flow and chemical reactions were performed in a horizontal reactor for GaN epitaxy. It was found that the gas flow rate Q is a key parameter which controls the spatial distribution of the growth rate above the susceptor. At low Q, the peak position of the growth rate shifted in the upstream direction. At an optimum Q, the growth rate distribution was spatially uniform. At high Q, the distribution was a split one with respect to the reactor symmetry plane. This was due to the peaking of gas flow velocity around the symmetry plane, which is driven by a pair of large return-flows.

References in 2.1

[1] S. Nakamura, *Phys. Status Solidi A* **176**, 15 (1999).

[2] S. Goto, T. Asano, Y. Suzuki, M. Takeya., Y. Shibuya, S. Ikeda, S. Uchida, and M. Ikeda, *Ext. Abstr. 48th Jpn. Soc. Appl. Phys. & Relat. Soc.* **1**, 369 (2001).

[3] R. C. Reid, J. M. Prausnitz, and B. E. Poling, *The Properties of Gases & Liquids*, 4th ed. (McGraw Hill, Boston, 1987).

[4] K. Harafuji, Y. Hasegawa, A. Ishibashi, A. Tsujimura, I. Kidoguchi, Y. Ban, and K. Ohnaka, *Jpn. J. Appl. Phys.* **39**, 6180 (2000).

[5] T. Mihopoulos, *Ph.D. Thesis* (Massachusetts Institute of Technology, 1999).

2.2. Room-temperature CW operation of InGaN MQW LDs with low indium content

Introduction

Remarkable progress of group III-nitride semiconductors has recently realized GaN-based violet laser diodes (LDs) with a lifetime of more than 10,000 hours under CW operation at room temperature [1]. These LDs operating around 400 nm band are the promising light source for high-density optical data storage system in the near future. The InGaN multiple quantum well (MQW) structure, which is extensively applied to an active medium, has a problem of considerable bandgap inhomogeneity caused by the inherent compositional fluctuation [2, 3]. However, the relation between the inhomogeneity and the laser performance has been unclear. In this section, I investigated the dependence of amplified spontaneous emission (ASE) spectra and threshold current density on indium content in InGaN/GaN MQWs, and obtained improved characteristics of the LDs by suppressing the bandgap inhomogeneity.

Epitaxial growth of the LD structures

The laser structure was grown on a (0001) sapphire substrate by low-pressure metalorganic vapor phase epitaxy. Source materials were trimethylgallium, trimethylaluminum, trimethylindium and ammonia. Silane and biscyclopentadienyl-magnesium were used as n-type and p-type dopant, respectively. The growth pressure was 40 kPa (300 Torr). The growth temperatures were in the range between 500 and 1050ºC. The laser structure consists of a GaN buffer layer (a thickness of 20 nm), a GaN layer (2 μm), a GaN:Si contact layer (2 μm), an $Al_{0.07}Ga_{0.93}N$:Si cladding layer (0.7 μm), a GaN:Si optical guiding layer (0.1 μm), an MQW active region, an $Al_{0.15}Ga_{0.85}N$:Mg capping layer (10 nm), a GaN:Mg optical guiding layer (0.1 μm), an $Al_{0.07}Ga_{0.93}N$:Mg cladding layer (0.7 μm) and a GaN:Mg contact layer (70 nm). The MQW active region consists of pseudomorphically strained 3 periods of $In_XGa_{1-X}N$ well layers (3 nm) and GaN:Si barrier layers (10 nm). Uniformity of the well width and interfacial abruptness were confirmed by transmission electron microscope observation.

Several samples with different In content of the well layers were prepared. Indium content X, which is determined by X-ray diffraction of lattice constants c and a taking into account the

deformation of the unit cell [4], was varied between 0.07 and 0.11.

ASE spectrum measurement

In order to investigate the dependence of bandgap inhomogeneity and optical gain on indium content in the InGaN MQWs, ASE from the LD wafers was measured at room temperature [5]. The sample was optically pumped by an optical parametric oscillation laser with 5 ns-long pulses and a repetition rate of 10 Hz at a wavelength of 368 nm, where the InGaN well layers were selectively excited, using the variable excitation-stripe length method [6]. The ASE emitted from the sample edge was detected by a multiple-channel analyzer. The excitation power density was approximately 1 MW/cm^2 and the length of the excited stripe was varied between 100 and 800 μm.

Figure 2.4 shows the ASE spectra for different In content of InGaN MQWs at excitation lengths of 400 and 800 μm. Blue shift and spectral narrowing of the ASE peak were observed with increasing excitation length for all the samples. They are attributed to the stimulated emission within the excited stripe. The spontaneous emission peak for short excitation length is governed by mean population distribution among the localized states. With increasing stimulated recombination, the gain peak concentrates around the mobility edge, where the density of state is high, due to increasing radiative decay rate [7].

The blue shift and the spectral narrowing of the ASE peak depended on the In content. The inset of Fig. 2.4 shows the blue shift and the full width at half-maximum (FWHM) of the peak for an excitation length of 800 μm as a function of X. For $X = 0.07$, the blue shift and the FWHM were as small as 20 meV and 53 meV, respectively. They increased rapidly for $X > 0.07$. This is similar to the dependence of Stokes-like shift on X which is reported previously [3]. The small blue shift and the narrow FWHM mean that the bandgap inhomogeneity is small and the gain peak is located near the spontaneous emission peak. They are of advantage to achieving the population inversion. These results suggest that low In content leads to small bandgap inhomogeneity and sharp optical gain spectrum. Therefore, it is desirable for the 400 nm band LDs to suppress the bandgap inhomogeneity in the InGaN MQW by optimizing indium content.
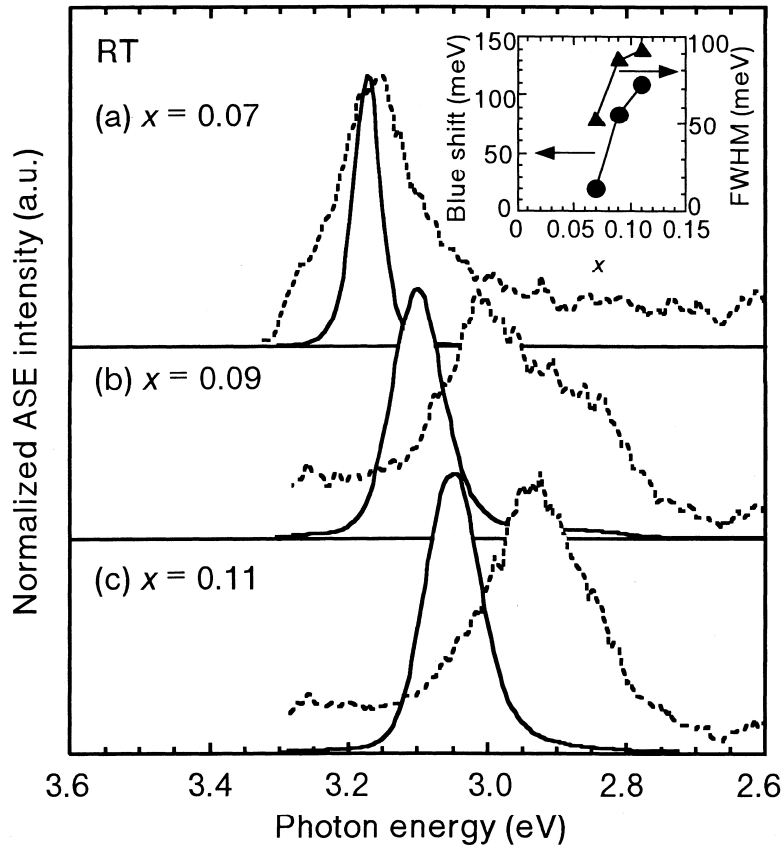
Fig. 2.4. Amplified spontaneous emission (ASE) spectra for $In_XGa_{1-X}N/GaN$ MQWs with different In content X of (a) 0.07, (b) 0.09 and (c) 0.11. Dashed and solid lines represent excitation lengths of 400 and 800 μm, respectively. The ASE intensity is normalized by peak intensity to compare each line width. Inset shows the relevant blue shift of the peaks and the FWHM of the spectra for an excitation length of 800 μm as a function of X.
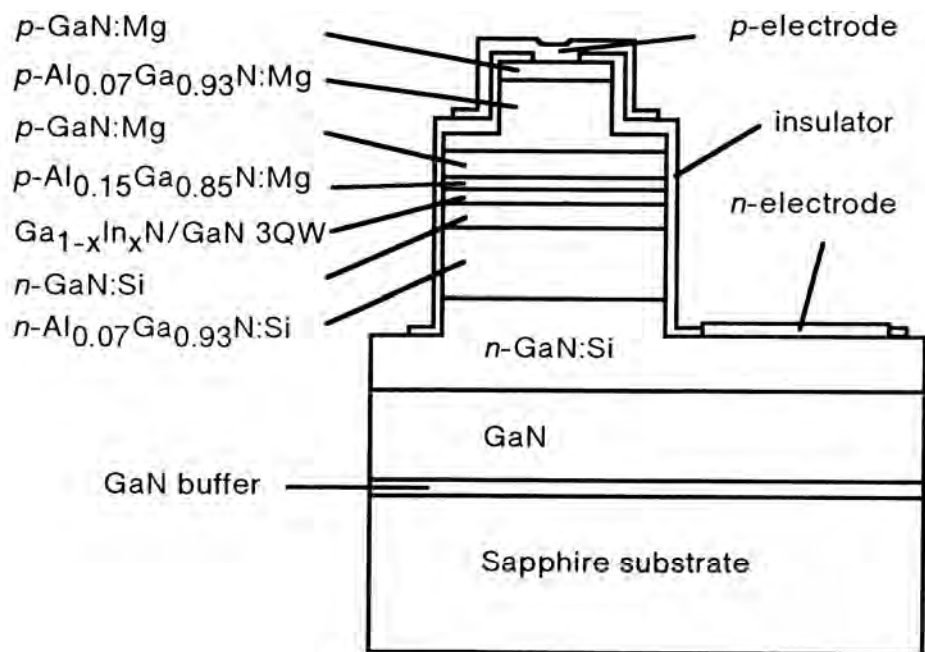
p-GaN:Mg

p-Al$_{0.07}$Ga$_{0.93}$N:Mg

p-GaN:Mg

p-Al$_{0.15}$Ga$_{0.85}$N:Mg

Ga$_{1-x}$In$_x$N/GaN 3QW

n-GaN:Si

n-Al$_{0.07}$Ga$_{0.93}$N:Si

p-electrode

insulator

n-electrode

n-GaN:Si

GaN

GaN buffer

Sapphire substrate

Fig. 2.5. Schematic structure of an In$_x$Ga$_{1-x}$N/GaN MQW LD.

Device characteristics

Ridge-geometry LDs with different In content X of the well layers were fabricated as shown in Fig. 2.5. The ridge width and the cavity length were 4 μm and 1 mm, respectively. The cavity was formed by cleavage. Both facets of LD chips were coated with high-reflection (HR) quarter-wave dielectric multiple layers, except some of the uncoated chips. The reflectivities of HR-coated facets were 58% and 94% for the front and rear facets, respectively. The LD chip was mounted on a heat sink with the junction-down configuration. The laser characteristics were measured at room temperature under pulsed operation using 5 μs-long pulses at a duty ratio of 0.5% and CW operation.

Figure 2.6 shows the relation between the threshold current density and the lasing wavelength of the uncoated LDs with different In content X under pulsed operation. The threshold current density decreased with decreasing lasing wavelength. The insets show emission spectra at the threshold for the LDs with $X = 0.07$ and 0.09. The laser emissions were observed at a wavelength of 396 nm for $X = 0.07$ and that of 408 nm for $X = 0.09$. Each spontaneous emission peak energy was identical with the ASE peak energy when the excitation length was as long as 800 μm. The laser emission peak energy was lower than the spontaneous emission peak energy. It is general for typical LDs [8]. These results support that low In content leads to small bandgap inhomogeneity, which is deduced from the ASE analysis.

Other characteristics were measured for an HR-coated $In_{0.07}Ga_{0.93}N$ MQW LD under pulsed operation. The characteristic temperature was 252 K in the ambient temperature range between 20 and 80ºC. Temperature dependence of the lasing wavelength was 0.066 nm/K. This value agrees with a previously reported one [9]. The beam FWHM of the near-field patterns were 3 μm and 0.9 μm for parallel and perpendicular to the junction, respectively. The far-field patterns of 4.5º and 23º for parallel and perpendicular to the junction, respectively, resulted in an aspect ratio of approximately 5 due to the wide ridge.

$In_{0.07}Ga_{0.93}N$ MQW LDs, which have smaller bandgap inhomogeneity, were operated under CW condition at room temperature. Figure 2.7 shows light output power and voltage versus injection current characteristics for an HR-coated $In_{0.07}Ga_{0.93}N$ MQW LD under CW operation. The threshold current, the corresponding threshold current density and the operating voltage at the threshold were 440 mA, 11 kA/cm^2 and 11.4 V, respectively. It is necessary to reduce the
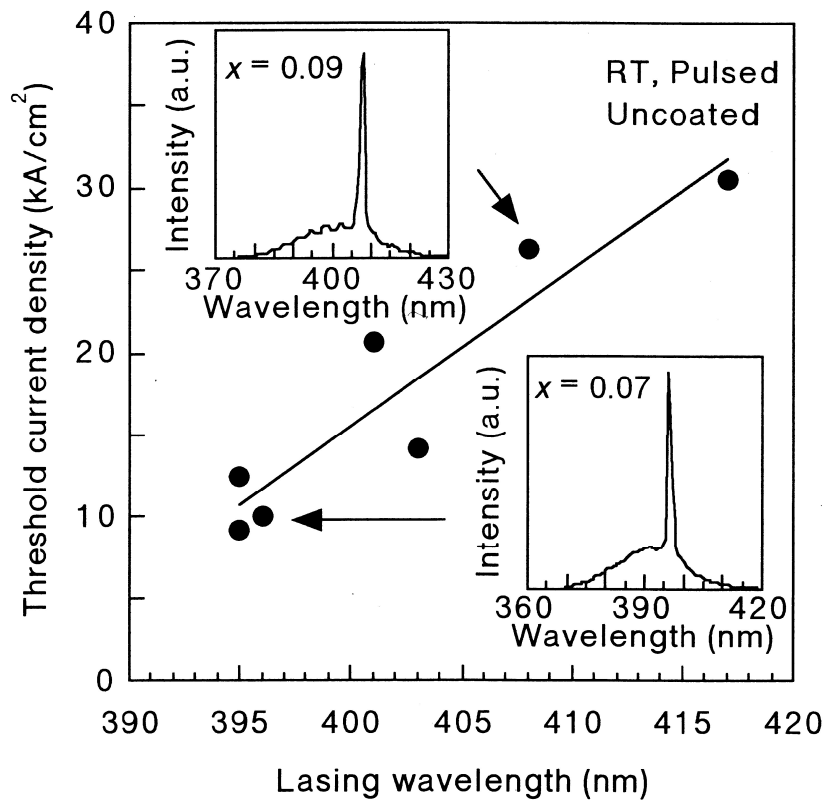
Fig. 2.6. Relation between the threshold current density and the lasing wavelength under pulsed operation of $In_XGa_{1-X}N$/GaN MQW LDs with different In content X at room temperature. The insets show emission spectra at the threshold for the LDs with $X = 0.07$ and 0.09.
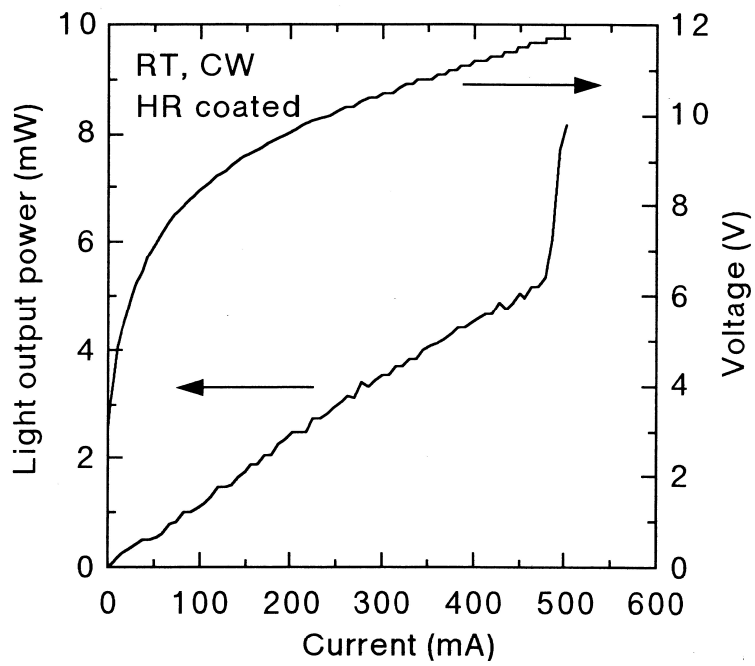
Fig. 2.7. Light output power and operating voltage versus injection current characteristics under CW operation of an $In_{0.07}Ga_{0.93}N/GaN$ MQW LD at room temperature.

threshold current and voltage through the improvement of crystalline quality and the laser structure.

Conclusion

It was necessary for GaN-based 400-nm-band LDs to suppress the bandgap inhomogeneity in the InGaN MQW by optimizing In content. The dependence of ASE spectra and threshold current density on X in $In_X Ga_{1-X}N$ (X = 0.07-0.11) MQW LDs exhibited that low In content led to small bandgap inhomogeneity and low threshold current density. Room-temperature CW operation of $In_{0.07}Ga_{0.93}N$ MQW LDs was demonstrated with a threshold current density of 11 kA/cm^2.

References in 2.2

[1] S. Nakamura, M. Senoh, S. Nagahara, N. Iwasa, T. Yamada, T. Matsushita, H. Kiyoku, Y. Sugimoto, T. Kozaki, H. Umemoto, M. Sano, and K. Chocho, *Jpn. J. Appl. Phys.* **36**, L1568 (1997).

[2] Y. Narukawa, Y. Kawakami, Sz. Fujita, Sg. Fujita, and S. Nakamura, *Phys. Rev. B* **55**, R1938 (1997).

[3] S. Chichibu, T. Sota, K. Wada, and S. Nakamura, *J. Vac. Sci. Technol. B* **16**, 2204 (1998).

[4] T. Takeuchi, H. Takeuchi, S. Sota, H. Sakai, H. Amano, and I. Akasaki, *Jpn. J. Appl. Phys.* **36**, L177 (1997).

[5] A. Tsujimura, Y. Hasegawa, A. Ishibashi, S. Kamiyama, I. Kidoguchi, R. Miyanaga, M. Suzuki, M. Kume, K. Harafuji, and Y. Ban, *Electron. Lett.* **35**, 998 (1999).

[6] K. L. Shaklee and R. F. Leheny, *Appl. Phys. Lett.* **18**, 475 (1971).

[7] A. Ishibashi, I. Kidoguchi, A. Tsujimura, Y. Hasegawa, Y. Ban, T. Ohata, M. Watanabe, and T. Hayashi, *J. Lumin.* **87**, 1271 (2000).

[8] P. Blood, A. I. Kucharska, J. P. Jacobs, and K. Griffiths, *J. Appl. Phys.* **70**, 1144 (1991).

[9] S. Nakamura, M. Senoh, S. Nagahara, N. Iwasa, T. Yamada, T. Matsushita, Y. Sugimoto, and H. Kiyoku, *Appl. Phys. Lett.* **69**, 4056 (1996).

2.3 Optical gain spectra in InGaN/GaN MQWs

Introduction

The violet laser diodes (LDs) using InGaN multiple quantum wells (MQWs) have attracted much attention for high-density optical storage disk systems [1]. The InGaN alloys have the bandgap inhomogeneity due to alloy fluctuation because of highly incomplete solubility. The recombination of localized excitons in the potential wells near the band edge or of quantum-dot-like states has been reported [2,3]. Many authors have also reported the stimulated emission (SE) from InGaN alloys and InGaN-based QWs under high-power excitation [4-9]. However, there are various experimental results about the behavior of emission bands changing from spontaneous to stimulated emission due to the variation of sample conditions, such as In content and/or growth method. As a result, several gain mechanisms such as electron-hole plasma and localized excitons (carriers) have been proposed [4-9]. In order to clarify the SE mechanism, and further, to obtain high gain for fabricating LDs, it is necessary to study the origin of optical gain at various temperatures for serially grown InGaN alloys with different In contents. In this section, the spontaneous and stimulated emission in InGaN/GaN MQWs with three kinds of In contents have been systematically studied under various excitation conditions.

Experimental

Samples were grown by low-pressure (300 Torr) metalorganic vapor phase epitaxy (MOVPE). A low-temperature GaN buffer layer (40 nm thick), a GaN layer (1.0 μm), 5 periods of $In_XGa_{1-X}N$ (2.5 nm)/GaN (7.5 nm) MQWs and a GaN (15 nm) capping layer were successively grown on a (0001) sapphire substrate. The InN mole fraction are $X = 0.05$, 0.10 and 0.16, which were determined by X-ray diffraction measurements.

Photoluminescence (PL) spectra under various excitation powers were observed at the surface emitting configuration using a nitrogen laser beam (at 337.1 nm, 10 Hz, 5 ns pulse duration, 17.5 MW/cm^2) focused to a spot size of ~ 500×500 μm^2.

The measurements of the optical gain were performed by the variable excitation stripe length (VEL) method at an excitation power density of 0.04-1.75 MW/cm^2 [10]. The amplified spontaneous emission (ASE) spectra were observed from the edge of the sample. The stripe
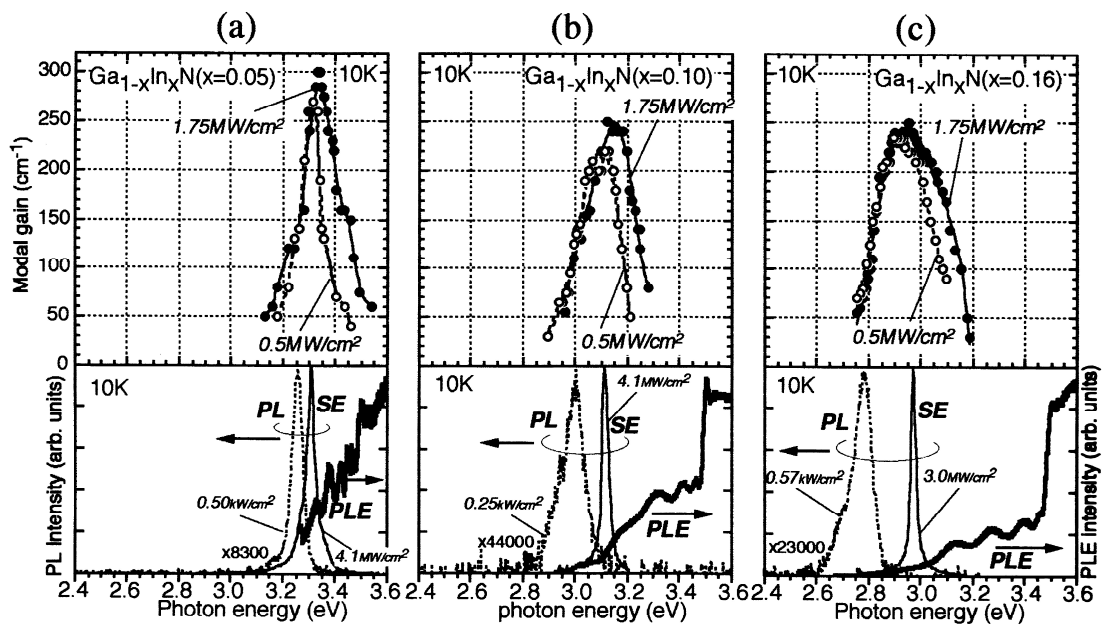
Fig. 2.8. Optical gain spectra obtained under the excitation powers of 0.5 (open circles), 1.75 (closed circles) MW/cm^2 (shown in the upper) and the PL, SE and PLE spectra (shown in the lower) for In$_X$Ga$_{1-X}$N of X = 0.05 (a), 0.10 (b) and 0.16 (c), measured at 10 K.

length l was changed from 0.02 to ~ 2 mm using slits. The net modal gain g was obtained using ASE intensity I by the relation [10]

$$I = \frac{I_0}{g \exp(gl) - 1}.$$ (2.7)

The time integration of the pulsed ASE signal was detected.

The photoluminescence excitation (PLE) spectra were measured by using Xe lamp.

Results and discussion

Figure 2.8 shows the gain spectra (upper) and the PL, SE and PLE spectra (lower) for $X = 0.05$ (a), 0.10 (b) and 0.16 (c), measured at 10 K. Two emission spectra are the spontaneous PL (broken lines) excited with low power and SE (solid lines) spectra, which were observed under and above the threshold excitation power density ($P_{exc.} = 0.1\text{-}1$ MW/cm^2), respectively, in the measurements of excitation power dependence of PL spectra. The PLE spectra monitored at the PL peak show the absorption tail of InGaN around the high-energy side of PL spectra. With increase of In content, the energy separation between the PL peak and the absorption tail increases. These PL spectra obtained at 10 K certainly originate from the recombination of localized excitons due to potential fluctuation [2,3]. For all the samples, the SE peak focuses on the high-energy end of PL. The energy separation between the PL peak and the SE also increases with In content. The gain peak obtained using Eq. (2.7) is almost coincident with the SE peak, and the high-energy side of the gain spectra increases with increase in the excitation power. The gain spectrum is sharp for lower In contents.

Figure 2.9 shows the gain spectra for $x = 0.10$ (a) and 0.16 (b) measured at 300 K (closed marks) and 10 K (open circles) under several excitation power densities. The gain spectra at 300 K have lower values and broader low-energy tails than those at 10 K. The gain peak shifts to higher energy with increase in the excitation power. The peak value obtained at 300 K for the highest excitation power in $X = 0.16$ is lower than that in $X = 0.10$.

The behavior about PL, SE, and gain spectra at 10 K can be systematically explained in terms of the density of states and the lifetime of localized states, for all the samples shown in Fig. 2.8. The localized excitons in the higher-energy states relax non-radiatively into the lower-lying states via phonon-assisted tunneling [6]. Increase in the excitation power induces
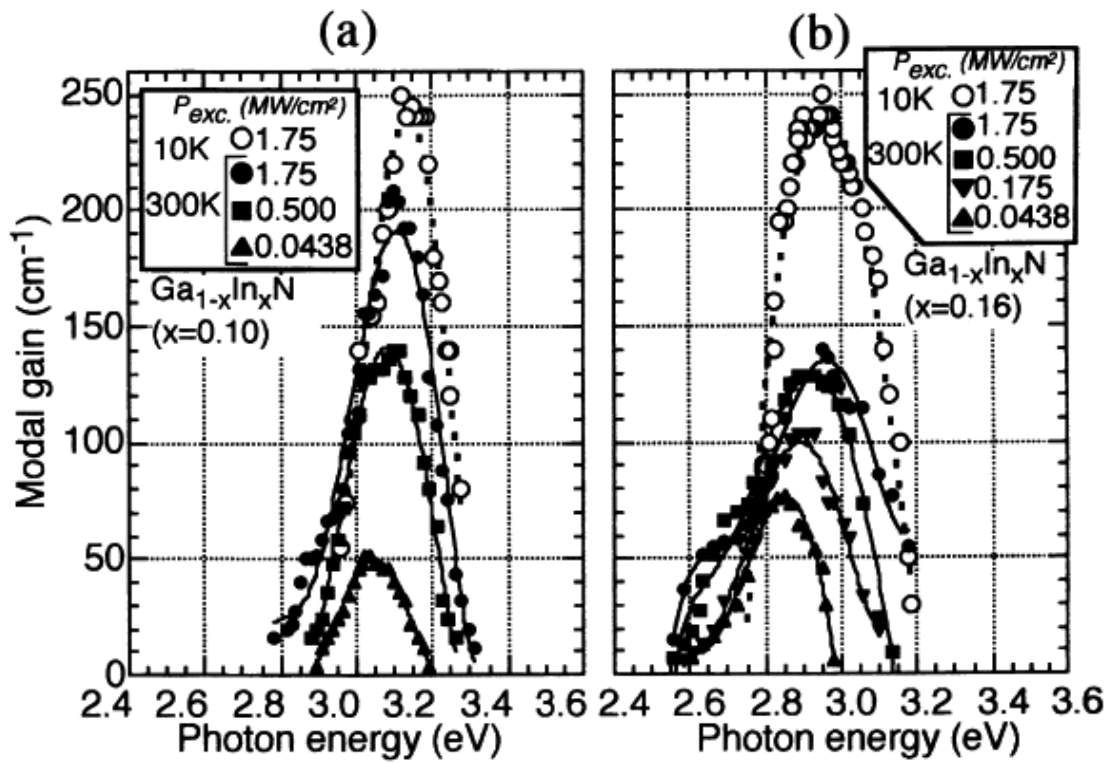
66

Fig. 2.9. Optical gain spectra for $In_XGa_{1-X}N$ of $X = 0.10$ (a) and $X = 0.16$ (b), measured at 300 K (closed marks) and 10 K (open circles) under various excitation powers.

the filling of the lower-lying states and the stimulated recombination at higher-energy states. With the increase in the stimulation effect, the gain concentrates around the mobility edge where the density of state is high. When the gain exceeds the loss, an intense and sharp SE can be observed around the high-energy end of PL. This mechanism is similar to that proposed by Satake *et al.* [6]. The present results confirm this mechanism in the range $X = 0.05$-0.16. From the PL measurements, it was found that the SE peak position slightly shifts to lower energy with increase of the excitation power at $P_{exc.} \geq 1$ MW/cm^2. This red-shift seems to be due to many-body bandgap renormalization effects, and the screening of excitons is expected to occur effectively, taking into consideration the carrier density and the exciton Bohr radius. Therefore, it is supposed that the positive gain due to deep-localized exciton states is, in fact, obtained, but it is relatively low, while the higher gain for SE is due to electron-hole plasma in the shallow-localized states around the mobility edge. The role of electron-hole plasma on SE has, so far, been shown at least for room temperature by several reports [4,8,9].

The PL intensity at 300 K obeys the squared excitation power dependence in the range of low excitation power (not shown in figures). It is confirmed that PL spectra obtained at room temperature are due to the recombination of thermally dissociated free electrons and holes for all the samples, as reported in Ref. 11. The power dependence implies that non-radiative recombination of carriers is dominant. The relaxation towards lower-energy states is also rapid at 300 K. These effects must give rise to the experimental results shown in Fig. 2.9, *i.e.*, the low gain and expansion of the spectrum at 300 K compared with 10 K, which become dominant for higher In content like $X = 0.16$. With increase in the bandgap inhomogeneity due to the alloy fluctuation, *i.e.*, increase of In content, the broadening of gain spectrum induces the increase of the threshold carrier density for lasing. Improvement in the bandgap inhomogeneity as well as in the carrier lifetime could make it possible to increase the gain, which realizes higher device performance of the violet LDs.

Conclusion

It was confirmed that the sharp and intense stimulated emission at the high-energy end of spontaneous emission originates from the optical gain due to electron-hole plasma around the mobility edge.

References in 2.3

[1] S. Nakamura, M. Senoh, S. Nagahara, N. Iwasa, T. Yamada, T. Matsushita, H. Kiyoku, Y. Sugimoto, T. Kozaki, H. Umemoto, M. Sano, and K. Chocho, *Jpn. J. Appl. Phys.* **37**, L309 (1998).

[2] S. Chichibu, T. Sota, K. Wada, and S. Nakamura, *J. Vac. Sci. Technol. B* **16**, 2204 (1998).

[3] Y. Narukawa, Y. Kawakami, Sg. Fujita, and S. Nakamura, *Phys. Rev. B* **59**, 10283 (1999).

[4] G. Mohs, T. Aoki, M. Nagai, R. Shimano, M. Kuwata-Gonokami, and S. Nakamura, *Solid State Commun.* **104**, 643 (1997).

[5] T. Deguchi, T. Azuhata, T. Sota, S. Chichibu, M. Arita, H. Nakanishi, and S. Nakamura, *Semicond. Sci. Technol.* **13**, 97 (1998).

[6] A. Satake, Y. Masumoto, T. Miyajima, T. Asatsuma, and M. Ikeda, *J. Cryst. Growth* **189/190**, 601 (1998).

[7] T. J. Schmidt, Y.-H. Cho, G. H. Gainer, J. J. Song, S. Keller, U. K. Mishra, and S. P. DenBaars, *Appl. Phys. Lett.* **73**, 3689 (1998).

[8] G. Frankowsky, F. Steuber, V. Harle, F. Scholts, and A. Hangleiter, *Appl. Phys. Lett.* **68**, 3746 (1996).

[9] Y.-K. Song, M. Kuball, A. V. Nurmikko, G. E. Bulman, K. Doverspike, S. T. Sheppard, T. W. Weeks, M. Leonard, H. S. Kong, H. Dieringer, and J. Edmond, *Appl. Phys. Lett.* **72**, 1418 (1998).

[10] K. L. Shaklee, R. E. Nahory, and R. F. Leheny, *J. Lumin.* **7**, 284 (1973).

[11] K. Domen, A. Kuramata, R. Soejima, K. Horino, S. Kubota, and T. Tanahashi, *IEEE J. Selected Topics Quantum Electron.* **4**, 490 (1998).

2.4 Ultraviolet emission from AlGaN double heterostructure LEDs

Introduction

The group III-nitrides, consisting of AlN, GaN, and their alloys, are attractive due to their large direct bandgaps of 6.2 and 3.4 eV, respectively, in their wurtzite structure. In particular, the ternary alloy $Al_XGa_{1-X}N$ has the potential for use in laser diodes (LDs), light-emitting diodes (LEDs) and detectors covering nearly the entire deep-ultraviolet (UV) region of the spectrum (200-365 nm). Applications of deep-UV emitters include highly dense optical storage systems, fluorescence-based chemical sensing and high-efficiency lighting. Despite a considerable amount of research directed towards InGaN-based violet LEDs [1,2] and LDs [3-5] which operate at wavelengths longer than 365 nm, very little research has been conducted on GaN [6] or AlGaN-based [7] UV LEDs [8] and LDs [9]. Homojunction GaN LEDs have been reported [10,11], and the emission is frequently dominated by a blue emission (~ 420 nm) due to carrier recombination involving Mg acceptors [6,10]. For the AlGaN double heterostructure (DH) LEDs, the linewidth of emission peak in excess of 40 nm suggests a band-to-impurity transition [6]. Recently, room-temperature (RT) operations of $Al_{0.2}Ga_{0.8}N/GaN$ MQW LEDs on sapphire substrate [12] and $Al_{0.12}Ga_{0.88}N/Al_{0.08}Ga_{0.92}N$ multiple quantum well (MQW) LEDs on SiC substrate [13] with emission peak wavelengths around 353 and 346 nm, respectively, have been reported. Although the introduction of MQW structures is promising, the large strain due to the difference in the Al mole fraction between the well layers and the barrier layers in the $Al_{0.15}Ga_{0.85}N/GaN$ MQW structure causes a significant piezoelectric field resulting in the longer emission wavelength and poorer emission efficiency. Therefore, it is difficult to shorten the emission wavelength simply by narrowing the well thickness or by increasing the Al mole fraction in the barrier layers [13].

In this section, I describe the fabrication and the characterization of AlGaN DH LEDs consisting of an $Al_{0.10}Ga_{0.90}N$ active layer and $Al_{0.13}Ga_{0.87}N$ cladding layers, which were grown on sapphire substrate. A DH structure with a relatively high Al content active layer was used in order for the UV LEDs to suppress the piezoelectric field [13]. LEDs were fabricated on sapphire substrate because a crack-free thick GaN layer can be grown on sapphire substrate under the active layer, resulting in the quality of the AlGaN active layer on sapphire substrate
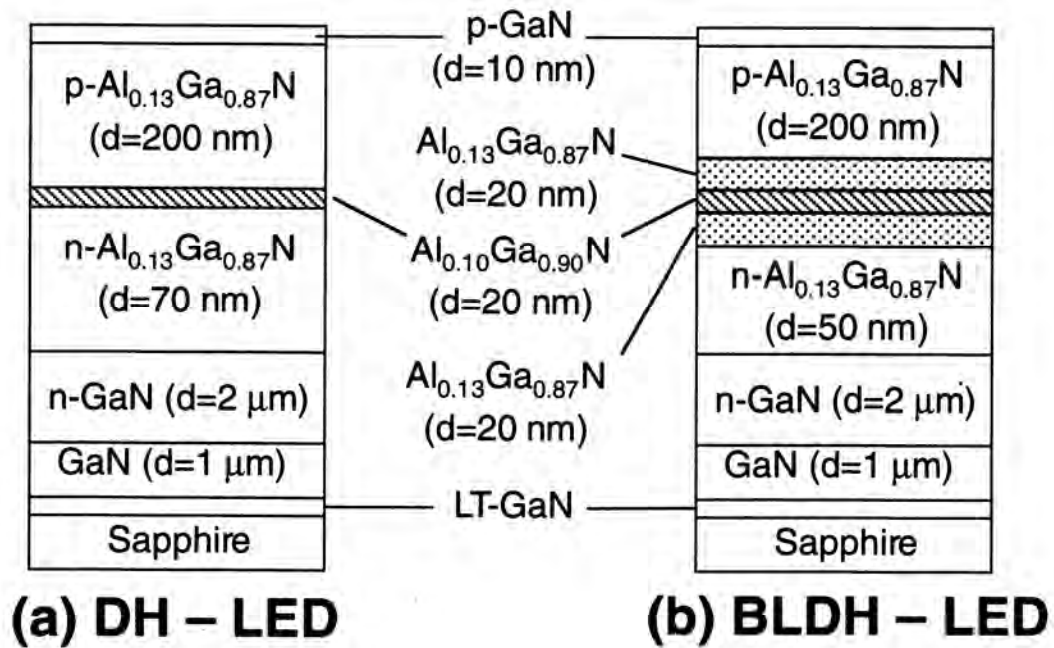
Fig. 2.10. Schematic of $Al_{0.13}Ga_{0.87}N/Al_{0.10}Ga_{0.90}N$ DH LED structures (a) without barrier layer, DH-LED and (b) with barrier layers, BLDH-LED.

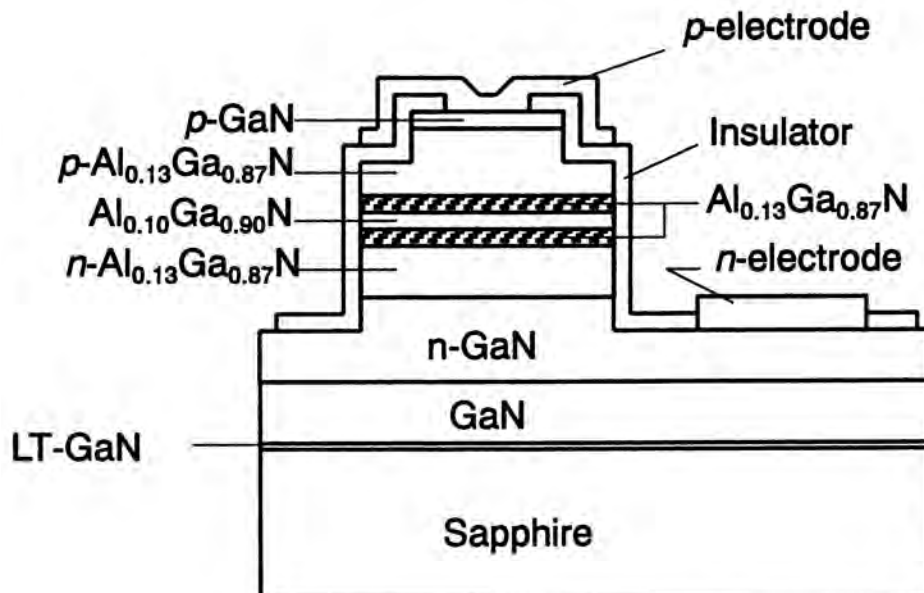Fig. 2.11. Schematic of $Al_{0.13}Ga_{0.87}N/Al_{0.10}Ga_{0.90}N$ ridge stripe BLDH structure.

being better than that on SiC substrate. An LED structure in which the active layer was sandwiched by undoped barrier layers has been proposed to prevent carrier recombination involving Mg acceptors [6]. The observed electroluminescence (EL) emission well within the deep-UV region of a wavelength of 339 nm at RT is the shortest wavelength reported for an AlGaN-based injection device fabricated on sapphire substrate, to the best of our knowledge.

Experimental

The LED structures were grown on (0001) sapphire substrate in a horizontal quartz tube reactor by low-pressure metalorganic vapor phase epitaxy (MOVPE) [14]. Trimethylgallium (TMGa), trimethylaluminum (TMAl) and ammonia (NH_3) were used as the Ga, Al and N precursors, respectively. Silane (SiH_4) and biscyclopentadienyl-magnesium (Cp_2Mg) were used as n-type and p-type dopants, respectively. Hydrogen (H_2) and nitrogen (N_2) were used as carrier gases. A two-step growth process was used in this work; namely, after the growth of a low-temperature (LT) GaN buffer layer (thickness $d = 20$ nm) at 480°C, a thick GaN layer was grown at 1120°C. The growth pressure was 300 Torr.

Two sets of LED structures have been fabricated to investigate the effect of the undoped barrier layers. Schematics of DH LED structures without barrier layers (DH-LED) and with barrier layers (BLDH-LED) are shown in Figs. 2.10(a) and (b), respectively. The DH-LED structure consists of an undoped GaN layer ($d = 1$ μm) grown on sapphire using the LT-GaN buffer layer, an n-GaN contact layer ($d = 2$ μm, carrier concentration $n = 10^{18}$ cm^{-3}), an n-$Al_{0.13}Ga_{0.87}N$ cladding layer ($d = 70$ nm, $n = 10^{18}$ cm^{-3}), an undoped $Al_{0.10}Ga_{0.90}N$ active layer ($d = 20$ nm), a p-$Al_{0.13}Ga_{0.87}N$ cladding layer ($d = 200$ nm, atomic concentration [Mg] ~ 10^{19} cm^{-3}), and a p-GaN contact layer ($d = 10$ nm). For the BLDH-LED structure, the active layer is sandwiched by undoped $Al_{0.13}Ga_{0.87}N$ barrier layers ($d = 20$ nm) and the thickness of the n-$Al_{0.13}Ga_{0.87}N$ cladding layer is 50 nm. After growth, the samples were annealed in a rapid thermal anneal furnace to activate the Mg acceptors. In-Zn alloy and In-Sn alloy were used for the p-type and n-type contacts with diameters around 1 mm for broad contact LEDs. Ridge stripe BLDH-LEDs have been also fabricated to estimate the potential for use in UV LD operation with high injection current density. Figure 2.11 shows a schematic of $Al_{0.13}Ga_{0.87}N/Al_{0.10}Ga_{0.90}N$ ridge stripe BLDH structure. A ridge stripe with a 3 μm width is
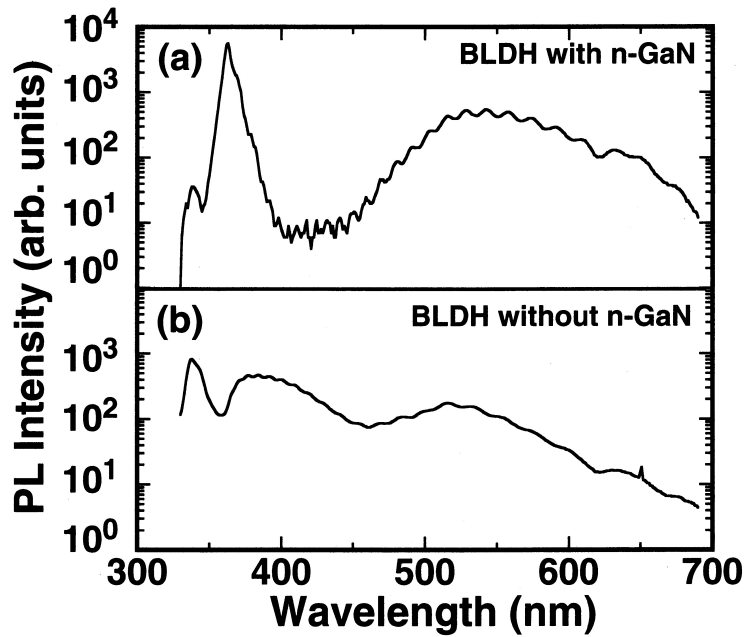
Fig. 2.12. Room-temperature photoluminescence spectra of $Al_{0.13}Ga_{0.87}N/Al_{0.10}Ga_{0.90}N$ BLDH-LED structures (a) with n-GaN contact layer and (b) without n-GaN contact layer.

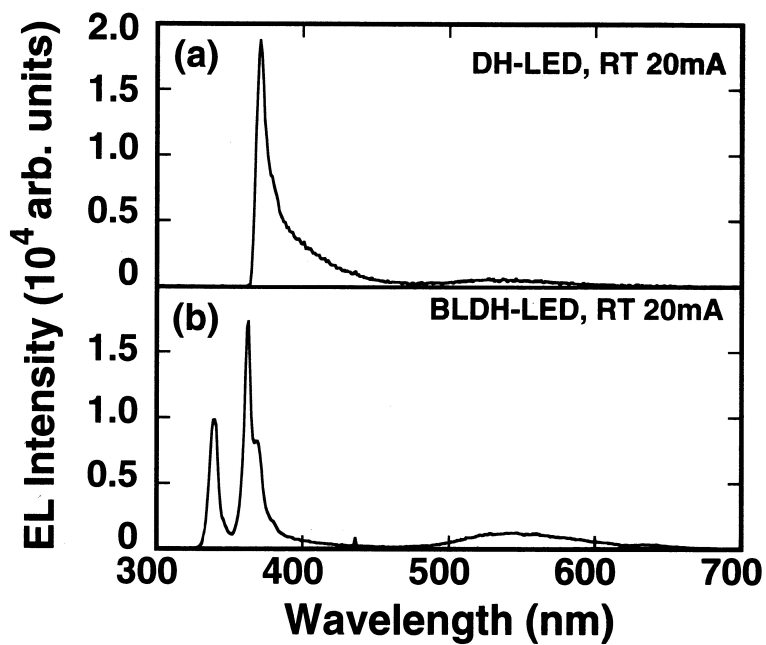Fig. 2.13. Room-temperature electroluminescence spectra of $Al_{0.13}Ga_{0.87}N/Al_{0.10}Ga_{0.90}N$ (a) DH-LED and (b) BLDH-LED. Emission peaks are at (a) 371 nm and (b) 339, 363 and 369 nm. Injection current is 20 mA.

formed for carrier confinement. Ni/Pt/Au and Ti/Al/Pt are evaporated for the p-type and n-type electrodes. The cavity length is 1 mm.

Photoluminescence (PL) measurements of the LED structures were performed using a He-Cd laser (325 nm). Current versus voltage (*I-V*) characteristics and the EL spectrum of the LEDs were measured using CW condition or pulsed modulation, in which the injection current is modulated from zero to a positive peak with a repetition frequency of 120 Hz.

Results and discussion

The room-temperature PL spectrum of the BLDH-LED structure is shown in Fig. 2.12(a). The PL spectrum of the DH-LED structure is almost the same as that of the BLDH-LED structure. For both the DH-LED and the BLDH-LED structures, a weak intensity peak at 338 nm is observed; this peak is attributed to the luminescence from the active layer, as inferred from its compositional wavelength. A strong intensity peak at 363 nm is attributed to the luminescence from the n-GaN contact layer because the PL intensity of the n-type layer is stronger than that of the undoped and p-GaN layer. In order to clarify the origin of the 363 nm emission, we fabricated a BLDH-LED structure without the n-GaN contact layer, in which the thicknesses of the undoped GaN layer and the n-$Al_{0.13}Ga_{0.87}N$ cladding layer were 0.2 and 2 μm, respectively. The PL spectrum is shown in Fig. 2.12(b). A strong intensity peak at 338 nm is observed and the intensity of the 363 nm peak decreases to a negligible value. Therefore, the PL peaks at 338 and 363 nm observed in Fig. 2.11(a) originate in the active layer and the n-GaN layer, respectively. The broad peaks around 400 and 500 nm are assumed to be due to the nitrogen vacancies and the buffer layer [15], respectively.

The room-temperature EL spectra from the DH-LED and the BLDH-LED are shown in Figs. 2.13(a) and (b), respectively. Only an EL peak at 371 nm is observed in Fig. 2.13(a), while EL peaks at 339, 363 and 369 nm are observed in Fig. 2.13(b). The EL emission at 339 nm, which is attributed to the active layer, as inferred from the PL spectrum of the LED structure, is the shortest wavelength for LEDs on sapphire at RT, to our knowledge. Therefore, the undoped barrier layers play important roles in obtaining the band-to-band emission of the active layer, and we concentrate on the BLDH-LED in the following discussion.

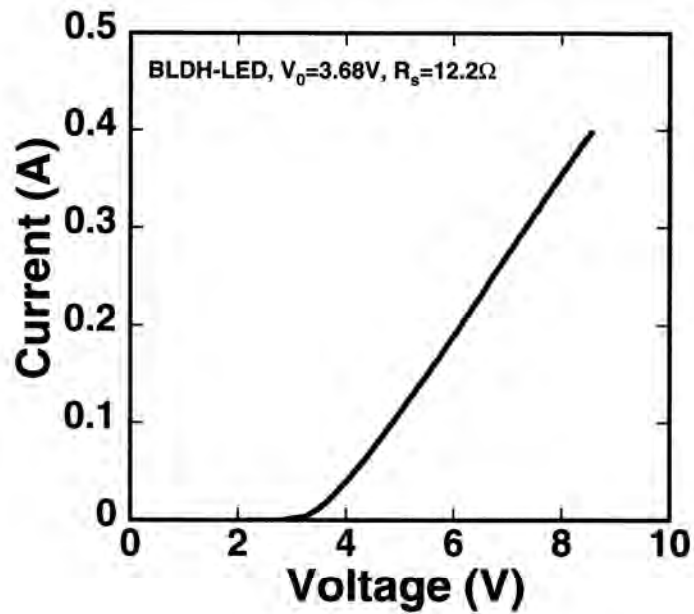Figure 2.14 shows the *I-V* characteristics for the BLDH-LED. The voltage increases steeply

Fig. 2.14. Injection current versus applied voltage characteristics for $Al_{0.13}Ga_{0.87}N/Al_{0.10}Ga_{0.90}N$ BLDH-LED at room temperature. Turn-on voltage (V_O) is 3.68 V and series resistance (R_S) of 12.2 Ω.

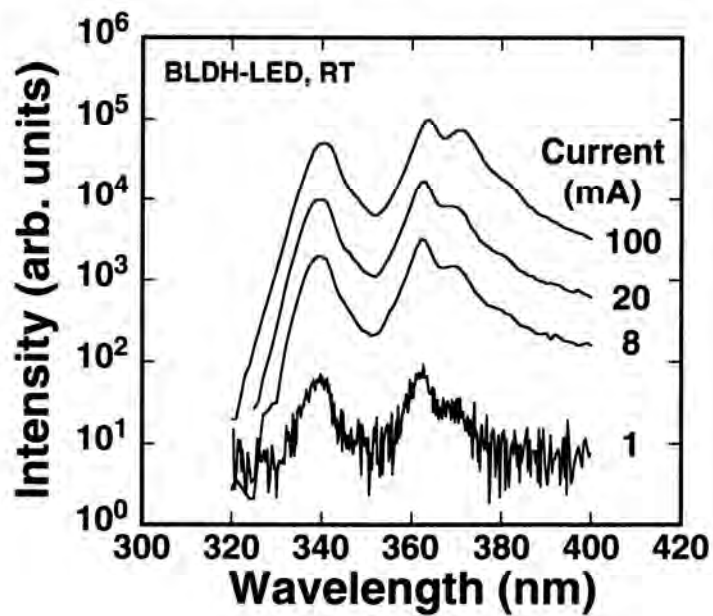Fig. 2.15. Room-temperature electroluminescence spectra of $Al_{0.13}Ga_{0.87}N/Al_{0.10}Ga_{0.90}N$ BLDH-LED under various levels of forward current injection. Current levels are indicated.

at a turn-on voltage (V_O) of 3.68 V, and then increases linearly with the injection current with a series resistance (R_S) of 12.2 Ω. The room-temperature EL spectra from the BLDH-LED for several different forward injection current levels are shown in Fig. 2.15. The intensities of the EL peaks at 339, 363, and 369 nm increase with the injection current. The intensity ratios among the three EL peaks show almost the same relationship, irrespective of the injection current. The EL peaks do not show any significant broadening or spectral shifts throughout the current range. The dependencies of the integrated EL intensity and full width at half-maximum (FWHM) on forward injection current for the 339 nm peak are shown in Fig. 2.16. The EL intensity increases with the injection current with a power (m_1) of 1.7 in the injection current range lower than 20 mA, while exhibiting a linear dependence in the injection current range higher than 20 mA, as reported for conventional LEDs [16]. These results indicate that the recombination process is changed from space-charge recombination, surface-recombination, or perimeter-recombination currents ($m_1 = 2$), in which the currents are predominantly nonradiative, to diffusion current ($m_1 = 1$), in which the radiative recombination resulting from band-to-band transition is dominant [7]. An FWHM linewidth of 5.6 nm (60 meV) obtained even for the BLDH-LED is as narrow as that of 5.8 nm for MQW LEDs [12]. The narrow linewidth of the BLDH-LED suggests that the emission is attributable to the band-to-band transition, and sufficient emission is obtained even in the BLDH-LEDs.

The EL peak around 363 nm for the BLDH-LED shown in Fig. 2.13(b) is probably attributable to the emission from the n-GaN layer which is excited by the 339 nm wavelength emission from the active layer, as inferred from the strong PL intensity of the n-GaN layer shown in Fig. 2.12(a). In order to study the origin of the EL peak at around 370 nm for the DH-LED shown in Fig. 2.13(a), a single heterostructure (SH) LED is fabricated. The SH-LED consists of the undoped GaN layer, the n-GaN contact layer, an n-$Al_{0.10}Ga_{0.90}N$ layer ($d = 200$ nm, $n = 10^{18}$ cm^{-3}), the p-$Al_{0.13}Ga_{0.87}N$ cladding layer and the p-GaN contact layer. The SH-LED also exhibits an EL peak at around 370 nm, which corresponds to the feature of the DH-LED shown in Fig. 2.13(a). We assume that the EL peak at around 370 nm is attributed to the recombination between the donor level in the n-$Al_{0.10}Ga_{0.90}N$ layer and the acceptor level in the p-$Al_{0.13}Ga_{0.87}N$ cladding layer. The acceptor activation energy of almost 0.32 eV in p-$Al_{0.13}Ga_{0.87}N$ [18-20] is larger than the valence band discontinuity of 0.02 eV between
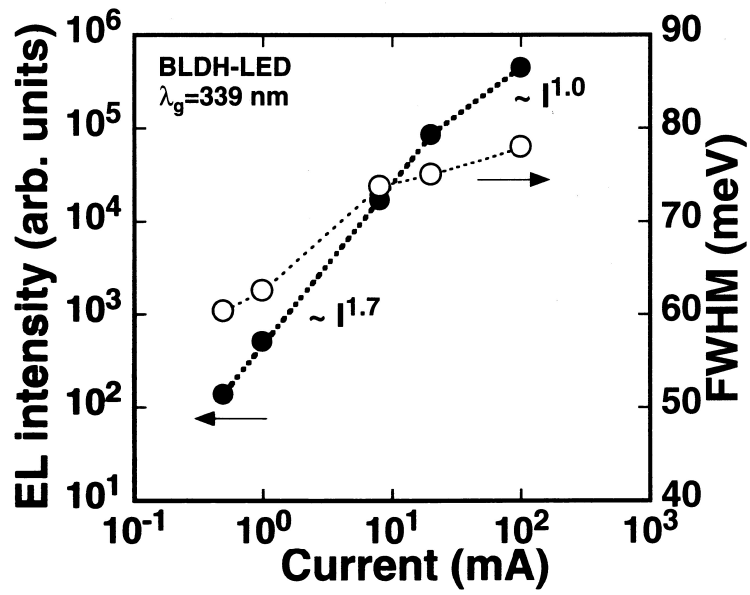
Fig. 2.16. Dependence of integrated electroluminescence intensity (closed circles) and full width at half-maximum (open circles) on forward injection current for 339 nm peak of $Al_{0.13}Ga_{0.87}N/Al_{0.10}Ga_{0.90}N$ BLDH-LED.
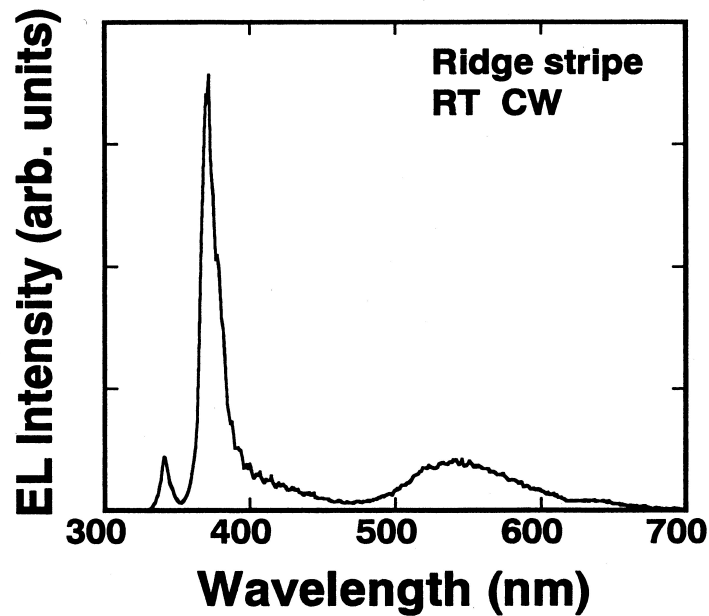

Fig. 2.17. Room-temperature emission spectra of ridge stripe BLDH structure. Emission peaks are at 342 and 370 nm. Injection current is 10 mA with CW operation.

Al$_{0.10}$Ga$_{0.90}$N and Al$_{0.13}$Ga$_{0.87}$N [21]. Thus, the acceptor level in the cladding layer corresponds to the level inside the bandgap of the active layer. The transition energy between the conduction band in the Al$_{0.10}$Ga$_{0.90}$N active layer to the acceptor level in the p-Al$_{0.13}$Ga$_{0.87}$N cladding layer is calculated to be 3.35 eV (370 nm), which is consistent with the EL emission around 370 nm for the DH-LED. For the BLDH-LED, the intensity of the EL peak at 369 nm is as small as that at 339 nm, as shown in Fig. 2.13(b), because the Al$_{0.10}$Ga$_{0.90}$N active layer and the p-Al$_{0.13}$Ga$_{0.87}$N cladding layer are separated by the undoped barrier layer and the recombination between the conduction band of the Al$_{0.10}$Ga$_{0.90}$N active layer to the acceptor level of the p-Al$_{0.13}$Ga$_{0.87}$N cladding layer is suppressed. Therefore, for UV emitters in which the acceptor level of the cladding layer corresponds to the level inside the bandgap of the active layer, the introduction of an undoped barrier layer between the active layer and the cladding layer is one way to suppress the recombination which results in long wavelength emission. An increase in the emission efficiency is expected with the introduction of a well-designed MQW structure [7,13].

The RT emission spectrum with CW operation from the ridge stripe BLDH structure is shown in Fig. 2.17. Emission peaks of 342 and 370 nm, which correspond to the 339 and 369 nm EL peaks for the BLDH-LEDs, respectively, are observed. The emission at 342 nm is attributed to the active layer. An FWHM linewidth of 6.3 nm (67 meV) obtained for the 342 nm peak in the ridge stripe BLDH structure is as narrow as that in the broad contact BLDH-LED.

The RT emission spectra from the ridge stripe BLDH structure for several different forward injection current levels of CW operation are shown in Fig. 2.18. The intensities of the emission peaks at 342 and 370 nm increase with the injection current. In order to study the origin of the 370 nm peak emission, the peak intensity ratio (P_{340}/P_{370}) of the peak intensity around 340 nm (P_{340}) to that around 370 nm (P_{370}) is calculated for the broad contact BLDH-LED and ridge stripe BLDH structure. The dependence of the peak intensity ratio on injection current density is shown in Fig. 2.19. The intensity ratio decreases with the injection current density with a power (m_3) of −0.47. This means that the peak intensity at 370 nm increases with the injection current with a power (m_2) of 1.47, which is calculated as follows:

$$P_{340} = P_1 \times I^{m1}, \quad P_{370} = P_2 \times I^{m2}, \tag{2.8}$$

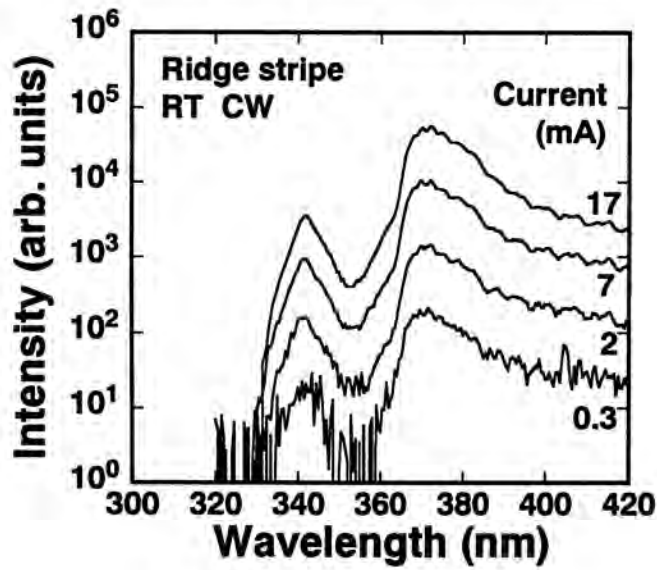$$\frac{P_{340}}{P_{370}} = \frac{P_1}{P_2} \times I^{m1-m2} = P_3 \times I^{m3}, \tag{2.9}$$

Fig. 2.18. Room-temperature emission spectra of ridge stripe BLDH structure under various levels of CW current injection.
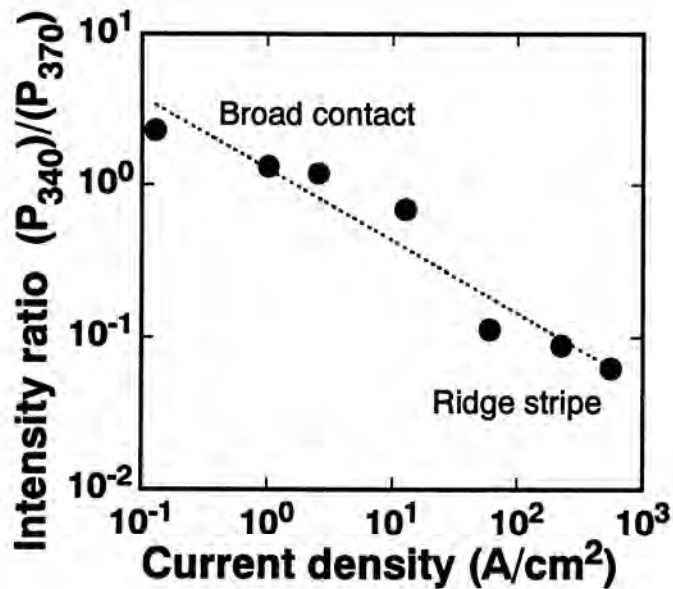

Fig. 2.19. Dependence of intensity ratio of the peak wavelength around 340 nm to that around 370 nm on injection current density for both broad contact BLDH-LED and ridge stripe BLDH structure.

$$m_2 = m_1 - m_3 \,, \tag{2.10}$$

where P_1, P_2 and P_3 are constants.

Therefore, radiative and nonradiative recombinations are comparable at 370 nm emission when the 340 nm emission is radiative ($m_1 = 1$). Carrier density of ridge stripe BLDH structure is higher than that of broad contact BLDH-LED. Thus, it is assumed that the carrier overflow to the p-cladding layer is dominant in ridge stripe BLDH structure. The emission peak around 370 nm is probably attributed to the emission from the recombination of overflow carriers involving Mg acceptors. A high Al content undoped buffer layer or a cap layer which has been introduced in typical violet LDs, is required to realize UV LD as well as to decrease the 369 nm emission in BLDH-LEDs.

These results, while providing an initial baseline, offer strong support for the viability of AlGaN UV LEDs. The recent demonstration of blue LEDs based on InGaN technology [22], combined with the observation of deep-UV emission from the AlGaN LEDs reported here, makes the prospect of extending LEDs and LDs technology into the deep-UV region of the spectrum using this material system appear promising.

Conclusion

Fabrication and characterization of $Al_{0.13}Ga_{0.87}N/Al_{0.10}Ga_{0.90}N$ DH LEDs on sapphire for UV emission were successfully reported. The introduction of the undoped barrier layers was proposed to suppress the carrier recombination involving Mg acceptors. The emission wavelength of 339 nm at RT, which has been the shortest wavelength previously reported, was observed. The emission linewidth of 60 meV as narrow as that reported for MQW LEDs suggested band-to-band transition. The dependence of emission intensity on injection current revealed that the diffusion current for the recombination process was dominant at the injection current of over 20 mA and that nonradiative recombination was suppressed. Ridge stripe BLDH structures were fabricated to estimate the potential for use in UV LD operation with high injection current density. The 342 nm emission was observed with CW operation at RT for ridge stripe LEDs. The 370 nm emission was enhanced with increasing injection current density. Thus, it was assumed that the suppression of carrier overflow to p-cladding layer is essential for decreasing long wavelength emission.

References in 2.4

[1] I. Akasaki, H. Amano, K. Itoh, N. Koide, and K. Manabe, *Inst. Phys. Conf. Ser.* **129**, 851 (1992).

[2] S. Nakamura, T. Mukai, and M. Senoh, *Appl. Phys. Lett.* **64**, 1687 (1994).

[3] S. Nakamura, M. Senoh, S. Nagahama, N. Iwasa, T. Yamada, T. Matsushita, H. Kiyoku, and Y. Sugimoto, *Jpn. J. Appl. Phys.* **35**, L74 (1996).

[4] I. Akasaki, S. Sota, H. Sakai, T. Tanaka, M. Koike, and H. Amano, *Electron. Lett.* **32**, 1105 (1996).

[5] T. Mukai, D. Morita, and S. Nakamura, *J. Cryst. Growth* **189/190**, 778 (1998).

[6] Y. Kuga, T. Shirai, M. Haruyama, H. Kawanishi, and Y. Suematsu, *Jpn. J. Appl. Phys.* **34**, 4085 (1995).

[7] H. Hirayama and Y. Aoyagi, *Ext. Abstr. 18th Electronic Materials Symp.* (1999) p.79.

[8] T. Mukai, M. Yamada, and S. Nakamura, *Jpn. J. Appl. Phys.* **37**, L1358 (1998).

[9] Y. Ohba and H. Yoshida, *Jpn. J. Appl. Phys.* **37**, L905 (1998).

[10] I. Akasaki, H. Amano, H. Murakami, M. Sasa, H. Kato, and K. Manabe, *J. Cryst. Growth* **128**, 379 (1993).

[11] M. A. Khan, Q. Chen, R. A. Skogman, and J. N. Kuznia, *Appl. Phys. Lett.* **66**, 2046 (1995).

[12] J. Han, M. H. Crawford, R. J. Shul, J. J. Figiel, M. Banas, L. Zhang, Y. K. Song, H. Zhou, and A. V. Nurmikko, *Appl. Phys. Lett.* **73**, 1688 (1998).

[13] T. Nishida and N. Kobayashi, *Phys. Status Solidi A* **176**, 45 (1999).

[14] A. Tsujimura, A. Ishibashi, Y. Hasegawa, S. Kamiyama I. Kidoguchi, N. Otsuka, R. Miyanaga, G. Sugahara, M. Suzuki, M. Kume, K. Harafuji, and Y. Ban, *Phys. Status Solidi A* **176**, 53 (1999).

[15] M. H. Zaldivar, P. Fernandez, and J. Piqueras, *J. Appl. Phys.* **83**, 2796 (1998).

[16] M. H. Pilkuhn and W. Shairer, *Light Emitting Diodes* (Elsevier Science Publishers B.V., Amsterdam, 1993) **4**, chap. 7, p. 634.

[17] K. Kurisu and T. Taguchi, *Electroluminescence, Springer Proceedings in Physics* (Springer-Verlag Berlin, Heidelberg, 1989) **38**, p. 367.

[18] M. Katsuragawa, S. Sota, M. Komori, C. Anbe, T. Takeuchi, H. Sakai, H. Amano, and I. Akasaki, *J. Cryst. Growth* **189/190**, 528 (1998).

[19] J. V. Orton and C. T. Foxon, *Properties, Processing and Application of Gallium Nitride and Related Semiconductors* (IEE, EMIS, INSPEC, UK, 1999) No. 23, chap. A8, p. 300.

[20] M. Suzuki, J. Nishio, M. Onomura, and C. Hongo, *J. Cryst. Growth* **189/190**, 511 (1998).

[21] J. A. Majewski, M. Sadele, and P. Vogl, *III-V Nitrides*, *Mater. Res. Soc. Symp. Proc.* **449**, 917 (1997).

[22] T. Mukai, M. Yamada, and S. Nakamura, *Jpn. J. Appl. Phys.* **38**, 3976 (1999).

Chapter 3

Development of novel epitaxial growth methods for ZnSe-based and GaN-based LDs

3.1. Compound source molecular beam epitaxy for ZnSe-based LDs

3.1.1 Surface reconstruction during compound source MBE growth and defects in the laser structure

Introduction

The molecular beam epitaxy (MBE) of high-quality II-VI films [1] and practical amphoteric doping of ZnSe n-type by ZnCl$_2$ [2] and p-type by N$_2$ radical doping [3] has lead to the realization of ZnSe-based lasers in blue-green region [4]. Continuous-wave (CW) operation of ZnSe-based lasers at room temperature was achieved [5-7] by using the ZnMgSSe quaternary alloy [8].

The devices reported so far have been grown by conventional MBE which employs mainly elemental sources (Zn, Se, Mg, Cd and Te) [5]. Demands for ternary and quaternary alloys require an increased number of cells, each of which contains elemental sources. The temperature necessary to obtain sufficient beam flux intensity for MBE growth are generally lower compared with the temperatures needed in the case of compound materials. With respect to conventional MBE, some difficulty exists in the control of the composition of alloys due to the number of temperatures to be adjusted and to the accuracy of relative intensity of three or more beam fluxes.

Ohkawa *et al.* have developed compound source MBE (CSMBE) for II-VI laser structures, and achieved CW operation at room temperature of the devices grown by CSMBE [7]. Binary polycrystalline compounds are adopted in CSMBE. Compound source MBE is able to reduce the number of source materials and to stabilize the VI/II beam flux ratio (J_{VI}/J_{II}) around unity. Compound source MBE also improves the uniformity and reproducibility of ternary and quaternary alloys of the laser structure. In this section, I describe the physics of CSMBE, especially the surfaces of II-VI films during CSMBE growth and defects in the laser structures.

Experimental

Source materials adopted are polycrystalline ZnSe (purity 6N), ZnS (5N), CdSe (6N), ZnTe (6N) and elemental Mg (6N). $ZnCl_2$ is used as an n-type doping source [2] and active nitrogen produced in a plasma source is used as a p-type doping source [3], as shown in Fig. 3.1. GaAs (100) substrates are used. Si-doped GaAs buffer layers (0.4 μm) with carrier concentrations of 10^{18} cm^{-3} were grown on the n-type GaAs:Si substrates only for the laser structures. ZnSe films were grown on the GaAs substrates directly, *i.e.* without the buffer layer. Growth temperatures for the ZnSe films varied from 50°C to 500°C. The II-VI laser structure consists of an n-ZnSe:Cl contact layer (30 nm), an n-ZnMgSSe:Cl cladding layer (0.83 μm), an n-ZnSSe optical guiding layer (85 nm), $Zn_{0.6}Cd_{0.4}Se$(2.4 nm)/ZnSSe(3.4 nm) triple quantum wells, a p-ZnSSe optical guiding layer (85 nm), a p-ZnMgSSe:N cladding layer (0.75 μm), a p-ZnSe:N capping layer (40 nm), a ZnSeTe:N graded bandgap layer (50 nm) and a p-ZnTe:N contact layer (40 nm). The ZnSSe and ZnMgSSe layers in the laser structure are nearly lattice-matched to the GaAs substrate. ZnSe binary layers and ZnSSe ternary layers were grown with only one (ZnSe) and two (ZnSe and ZnS) sources in CSMBE, respectively. The S mole fraction in ZnSSe can be varied by the ZnSe/ZnS beam flux ratio. The VI/II beam flux ratio is exactly unity for the growth of ZnSe and ZnSSe. ZnMgSSe quaternary layers were also grown by CSMBE with three sources of ZnSe, ZnS, and Mg. The bandgap and lattice constant of ZnMgSSe were controlled by varying these three beam fluxes. The bandgap defined by the band-edge emission of ZnMgSSe cladding layer is 2.93 eV at 12 K. Carrier concentrations for n- and p-type ZnSe, ZnSSe, ZnMgSSe layers are on the order of 10^{17} cm^{-3}. This structure was grown at 280°C. The GaAs substrate temperature was measured by an infrared pyrometer which was calibrated in advance from the oxide desorption temperature (582°C) of GaAs substrates. The typical growth rate was 0.55 μm/h for ZnMgSSe layer.

Crystal quality of the layers grown by CSMBE was evaluated by photoluminescence (PL) at 12 K. Surface reconstruction during CSMBE growth was studied by reflection high-energy electron diffraction (RHEED) observation with an applied voltage of 8 kV. Surface morphology was observed by a scanning electron microscope (SEM) and an atomic force microscope (AFM). The structure of the defects was studied by transmission electron microscopy (TEM).
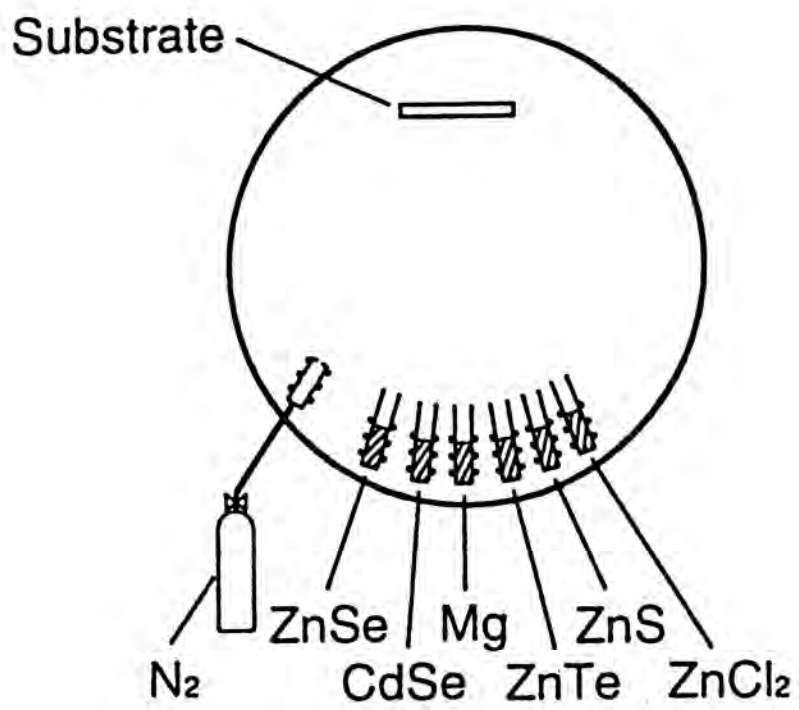
Fig. 3.1. Schematic diagram of the compound source MBE.

Results and discussion

The PL spectrum from an undoped ZnSSe film nearly lattice-matched to GaAs shows dominant free-exciton emission (E_X) and well suppressed deep-level emission, indicating the high purity and quality of the film. Figure 3.2 shows that the PL spectrum from a Cl-doped ZnMgSSe film ($N_D-N_A \approx 10^{17}$ cm^{-3}) lattice-matched to GaAs exhibits intense neutral donor-bound exciton emission (I_2) at 2.95 eV. The intensity of deep-level emission is as low as 10^{-2} of that of the I_2 emission. The spectrum indicates the high quality of the film.

The VI/II ratio and the growth temperature influence surface reconstruction. The VI/II ratio for CSMBE is fixed around unity, therefore the surface reconstruction depends strongly on the growth temperature. A clearly streaked (2 × 1) reconstructed pattern was observed for ZnSe, ZnSSe, ZnTe layers during CSMBE growth at 280°C [7]. Surface reconstruction of ZnSe during CSMBE was studied at various growth temperatures. The (2 × 1) reconstructed pattern was observed in the temperature range from 100°C to 350°C. This means that the surface is Se-stabilized in spite of the condition $J_{VI}/J_{II} = 1$. In the case of conventional MBE, the surface is Zn-stabilized during the growth of ZnSe with $J_{VI}/J_{II} = 1$ [9]. The growth mechanism of CSMBE will be different from that of conventional MBE. Species produced from elemental selenium are Se$_6$: Se$_5$: Se$_7$: Se$_2$: Se$_8$ = 1.00 : 0.66 : 0.28 : 0.11 : 0.04 at around the operation temperature of 200°C [10]. On the other hand, the Se$_2$ beam is produced in CSMBE because the ZnSe compound sublimes dissociatively as follows [11]:

$$\text{ZnSe (solid)} \rightarrow \text{Zn (gas)} + \frac{1}{2}\text{Se}_2 \text{ (gas)}. \tag{3.1}$$
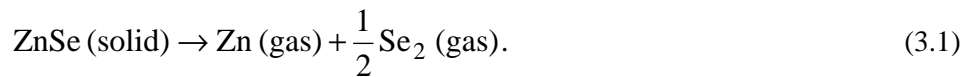
The Se$_2$ molecules presumably have higher sticking coefficients compared with Se$_6$, Se$_5$ and Se$_7$. Therefore, the anion-stabilized surface is obtained for the CSMBE growth with $J_{VI}/J_{II} = 1$. A streaky pattern was observed in the temperature range of 150-350°C. The pattern means there is a smooth surface which is suitable for the growth of laser structures.

The c(2 × 2) pattern meaning a Zn-stabilized surface was seen in the temperature range of above 400°C or after a moment interrupting the growth. Growth of ZnSe epitaxial films has been achieved at growth temperature as low as 50°C. A two-dimensional growth was observed down to 100°C. These were confirmed by the RHEED observation shown in Fig. 3.3. Cheng *et al.* and Cammack *et al.* reported that epitaxial growth of ZnSe at the growth temperature down
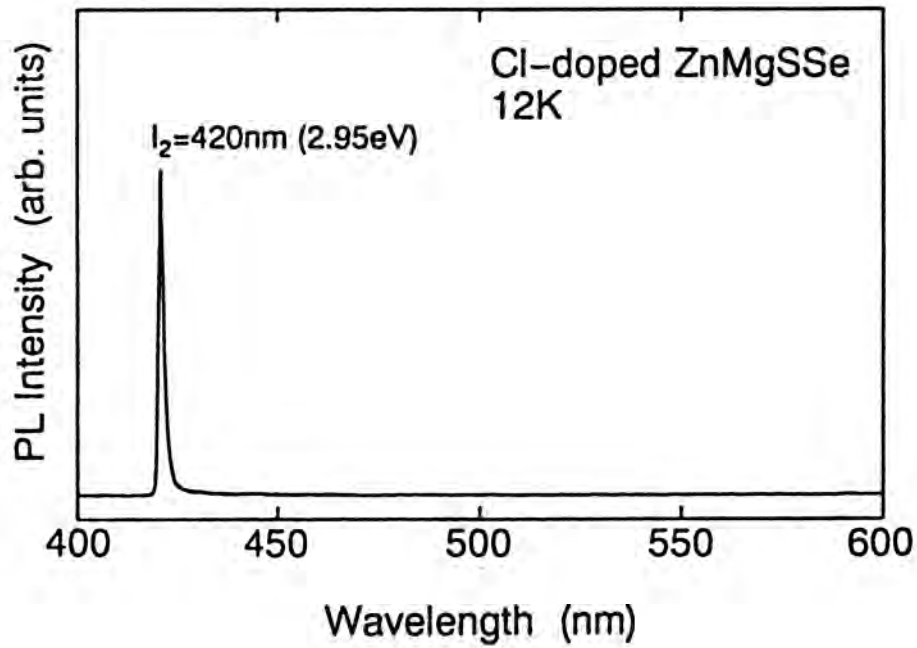
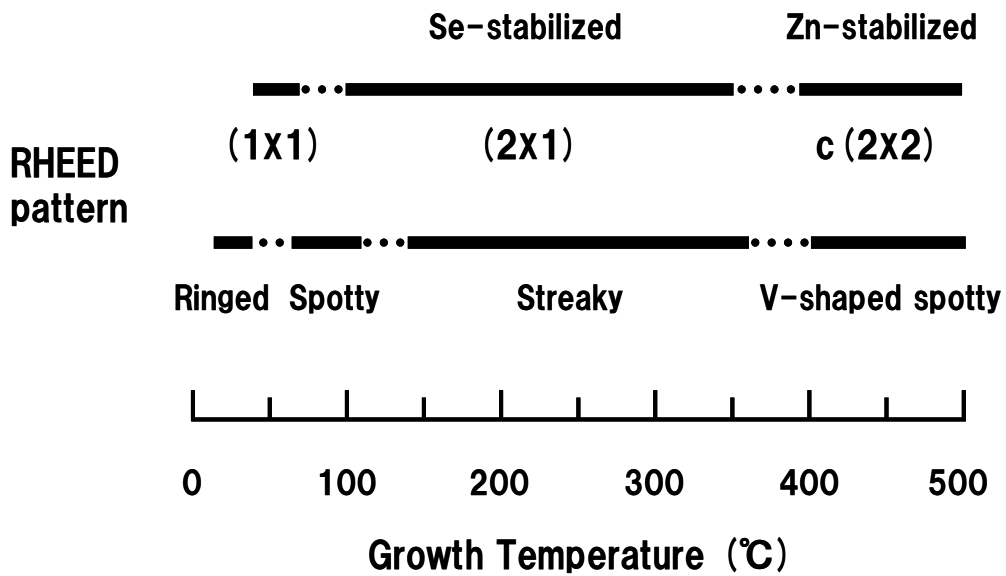Fig. 3.2. 12 K PL spectrum obtained from a Cl-doped ZnMgSSe/GaAs film grown by CSMBE.

Fig. 3.3. RHEED patterns from ZnSe films grown by CSMBE at various growth temperatures.

to 150°C is possible by using elemental Zn and thermally cracked selenium as source materials [10,12]. Furthermore Ohishi *et al.* shown that ZnSe epitaxial films are successfully grown by MBE at the temperature of 100°C using hot molecular beams generated by post-heating at 600°C both for Zn and Se [13]. Since molecular beams from polycrystalline compounds are fully cracked to group VI diatoms and hot (about 800°C), the CSMBE technique has realized the low-temperature growth below 100°C.

Intensities of the substreaks of ZnSSe, ZnSe and ZnTe surfaces increase in this order, indicating that the sticking coefficients of group VI elements on the growth front are in the order of S < Se < Te. Furthermore, ZnMgSSe films whose flux ratio during the growth was $J_{VI}/J_{II} < 1$ showed a mixture of (2×1) and $c(2 \times 2)$ reconstructed surface due to the simultaneous impingement of II-VI elements and Mg. Further investigation is needed for an understanding of the growth mechanism of CSMBE.

The structural defects in the laser structures observed were stacking faults generated at the II-VI/III-V interface at a density of 10^4-10^6 cm^{-2} and defects (more than 10^9 cm^{-2}) at the ZnSeTe contact layer due to lattice mismatch. The origin of the stacking fault was not determined by the TEM observation. Cross-sectional and plan-view images show that two stacking faults form "a bow tie" as shown in Fig. 3.4. One triangle corresponds to one stacking fault, and a strained area with the shape of a triangle outside of the stacking faults can also be observed. The stacking faults can be seen by the SEM observation of an as-grown sample without any chemical etching. Two stacking faults form a hillock which consists of two hills joined as shown in Fig. 3.5. The hillock exists on the upper area of the bow tie and the strained area. The AFM measurement shows that heights of the top and the narrow part of the hillock are 130 and 66 nm, respectively. The edge of the stacking faults corresponds to the top of the each hill. The growth rate around the defects increased by a maximum of 7%. The growth rate of hillocks shows enhanced surface migration or enhanced sticking coefficients at defects. Considering the same defects, *i.e.*, a pair of stacking faults, are observed both for CSMBE and conventional MBE, the result implies that surface migration in case of CSMBE is enhanced compared with conventional MBE.

Furthermore, I point out an important difference between CSMBE and conventional MBE. The composition modulation which is observed for the ZnMgSSe quaternary alloys grown by conventional MBE [14] has never been seen for those grown by CSMBE. Further study will be
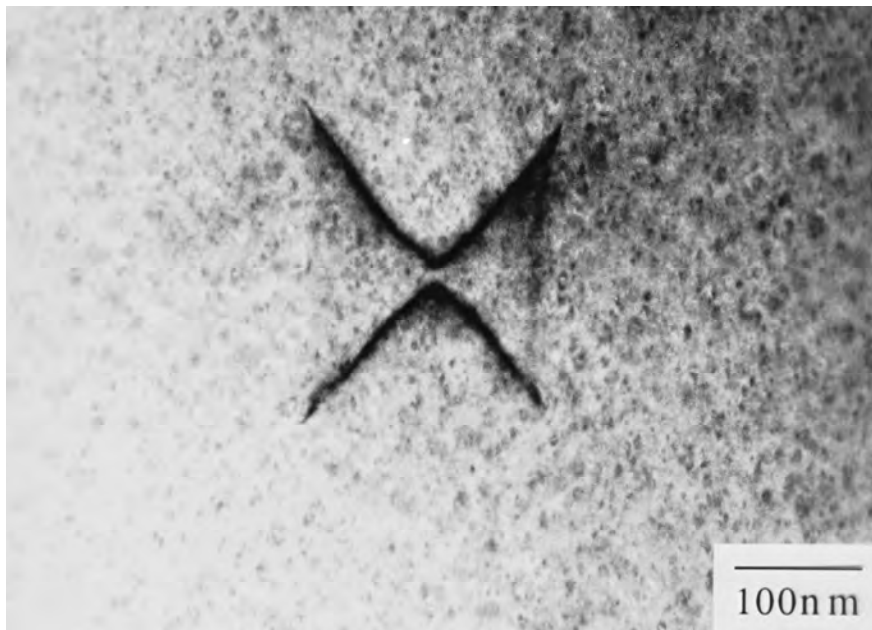
Fig. 3.4. Plan-view TEM showing a pair of stacking faults. The sample was thinned, *i.e.* the p-side layers were removed.
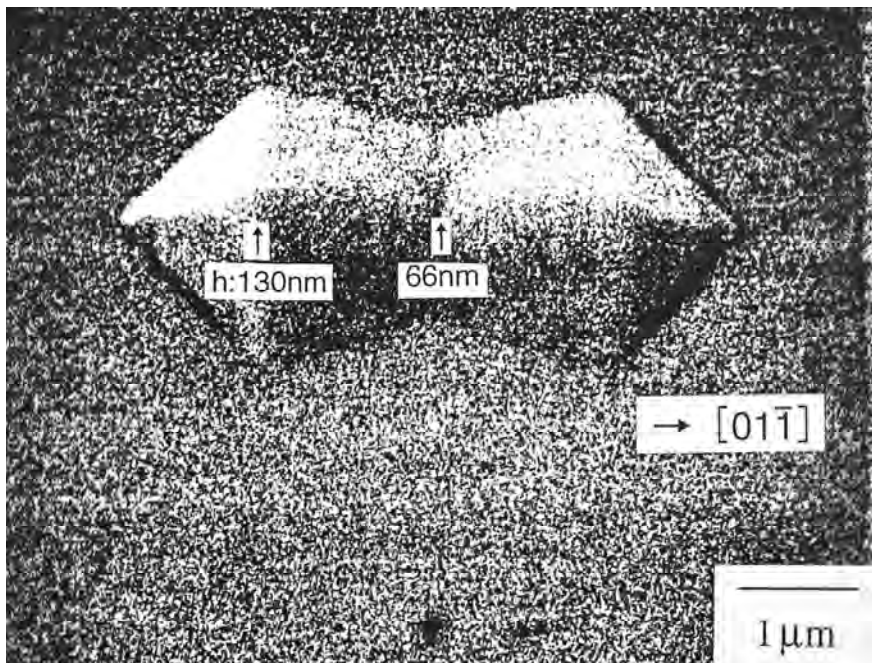

Fig. 3.5. Plan-view SEM showing a pair of stacking faults observed for as-grown surface of a laser structure.

necessary to understand the phenomena.

Conclusion

ZnSe films and laser structures grown by CSMBE were studied. It was found that surface of ZnSe film during the growth is anion (Se)-stabilized at the growth temperature of 100-350°C in spite of the condition $J_{VI}/J_{II} = 1$. Low-temperature (below 100°C) growth was realized. A unique hillock which corresponds to a pair of the stacking faults was observed on the laser structures. Composition modulation was not seen for ZnMgSSe alloys. These results were due to the difference of growth mechanisms for conventional MBE and CSMBE, since CSMBE produces reactive molecular beams involving the group VI diatomic molecules with high kinetic energy due to the high operation temperature.

References in 3.1.1

[1] T. Yao, S. Amano, M. Ogura, S. Matsuoka, and T. Morishita, *Appl. Phys. Lett.* **43**, 499 (1983).

[2] K. Ohkawa, T. Mitsuyu, and O. Yamazaki, *J. Appl. Phys.* **62**, 3216 (1987).

[3] K. Ohkawa, T. Karasawa, and T. Mitsuyu, *J. Cryst. Growth* **111**, 797 (1991).

[4] M. A. Haase, J. Qiu, J. M. DePuydt, and H. Cheng, *Appl. Phys. Lett.* **59**, 1272 (1991).

[5] N. Nakayama, S. Itoh, T. Ohata, K. Nakano, H. Okuyama, M. Ozawa, A. Ishibashi, M. Ikeda, and Y. Mori, *Electron. Lett.* **29**, 1488 (1993).

[6] A. Salokatve, H. Jeon, J. Ding, M. Hovinen, A. V. Nurmikko, D. C. Grillo, L. He, J. Han, Y. Fan, M. Ringle, R. L. Gunshor, G. C. Hua, and N. Otsuka, *Electron. Lett.* **29**, 2192 (1993).

[7] K. Ohkawa, S. Yoshii, H. Takeishi, A. Tsujimura, S. Hayashi, T. Karasawa, and T. Mitsuyu, *Jpn. J. Appl. Phys.* **33**, L1673 (1994).

[8] H. Okuyama, K. Nakano, T. Miyajima, and K. Akimoto, *J. Cryst. Growth* **117**, 139 (1992).

[9] K. Menda, I. Takayasu, T. Minato, and M. Kawashima, *Jpn. J. Appl. Phys.* **26**, L1326 (1987).

[10] H. Cheng, J. M. DePuydt, M. A. Haase, and J. E. Potts, *J. Vac. Sci. Technol. B* **8**, 181 (1990).

[11] P. Goldfinger and M. Jeunehomme, *Trans. Faraday Soc.* **59**, 2851 (1963).

[12] D. A. Cammack, K. Shahzad, and T. Marshall, *Appl. Phys. Lett.* **56**, 845 (1990).

[13] M. Ohishi, H. Saito, M. Yoneta, and Y. Fujisaki, *J. Cryst. Growth* **117**, 125 (1992).

[14] L. H. Kuo, L. Salamanca-Riba, B. J. Wu, J. M. DePuydt, G. M. Haugen, H. Cheng, S. Guha, and M. A. Haase, *Appl. Phys. Lett.* **65**, 1230 (1994).

3.1.2. Fabrication and characterization of ZnMgSSe quaternary LDs

Introduction

The molecular beam epitaxy (MBE) growth technique for high-quality ZnSe and related materials was developed in the early 1980s [1]. Practical amphoteric doping for MBE-grown ZnSe was developed in 1986 for the n-type and in 1990 for the p-type, where $ZnCl_2$ [2] and active nitrogen from a plasma sources [3] were employed as n- and p-type dopants, respectively. Since the first report by Haase *et al.* in 1991 [4], the developments of ZnSe-based laser diodes (LDs) by means of MBE have progressed rapidly. CW operation of ZnSe-based LDs at room temperature was achieved in 1993 [5,6]. The most promising laser structure is a pseudomorphic ZnCdSe/ZnSSe/ZnMgSSe [7], ZnSeTe graded-bandgap contact [8] and GaAs buffer [9] layers [6,10]. The devices reported so far have been grown by conventional MBE which employs mainly elemental sources (Zn, Se, Mg, Cd and Te) [10]. Demands for ternary and quaternary alloys require an increased number of cells, each of which contains elemental sources. The temperatures necessary to obtain beam flux intensity for the MBE growth are generally lower compared with the temperatures needed in the case for compound materials. With respect to conventional MBE, some difficulty exists in the control of the composition of alloys due to the number of temperatures to be adjusted and to the accuracy of relative intensity of three or more beam fluxes. A few groups attempted to grow II-VI compounds by using compound source such as ZnSe, ZnS, ZnTe and CdTe in the early stage of MBE [11-13]. Such compound source MBE (CSMBE) had not been employed in the past several years except by our group [14].

This study is the first report of the growth of quaternary alloys and LD structures by CSMBE. The study shows the possible reduction of the number of source materials, and precise control of the VI/II beam flux ratio (J_{VI}/J_{II}) around unity. The results indicate that CSMBE improves the uniformity and reproducibility of ternary and quaternary alloys of the LD structure. The ZnCdSe/ZnSSe/ZnMgSSe LD structure has been attempted to grow by CSMBE. The surface structure during growth and properties of epitaxial films have been examined.

Experimental

Source materials adopted are polycrystalline ZnSe (purity 6N), ZnS (5N), CdSe (6N), ZnTe

(6N) and elemental Mg (6N). $ZnCl_2$ is used as an n-type doping source [2], and p-type layers are doped with active nitrogens produced in a plasma source [3]. First, Si-doped GaAs buffer layers with carrier concentration of 2×10^{18} cm^{-3} were grown on Si-doped GaAs (100) substrates by MBE at 590°C. Then, the wafer with the (2×4) reconstructed surface was transferred in ultrahigh vacuum from the III-V growth chamber to the II-VI growth chamber. The growth temperature for the ZnSe-based LD structure was maintained at 280°C. The growth rate was about 0.5 μm/h. The LD structure wafer was processed into gain-guided LDs with 5 μm mesa stripe and 750 μm resonator length. ZnS deposited by vacuum evaporation was used as an insulator. Contacts to p-ZnTe layer and n-GaAs substrate were made with Pd/Au and In, respectively. The device was mounted with the p-side in contact with a Cu block for efficient heatsinking. The device performance was measured at room temperature (23-24°C) under pulsed (500 ns current pulses at a duty cycle of 0.05%) and CW operations.

Results and discussion

Figure 3.6 is a photoluminescence (PL) spectrum from an undoped ZnSSe film nearly lattice matched to GaAs. The film was grown by CSMBE with the beam pressure ratio of $P_{ZnS}/(P_{ZnS}+P_{ZnSe}) \approx 0.2$. The spectrum shows dominant free-exciton emission (E_X) and well suppressed deep-level emission. Intensity of the E_X emission is stronger than that of neutral-donor-bound exciton emission (I_2). The spectrum indicates high purity of ZnSSe film, and source materials of ZnSe and ZnS have sufficient purity for MBE growth of ZnSe-related materials.

Net acceptor concentration, determined by capacitance-voltage measurement, of N-doped ZnSe by CSMBE reached 2×10^{18} cm^{-3} for 200°C growth and 7×10^{17} cm^{-3} for 280°C growth. The van der Pauw method at room temperature gave a hole concentration of 3×10^{19} cm^{-3} and a Hall mobility of 36 cm^2/Vs for N-doped ZnTe film. These electrical properties of p-ZnSe and p-ZnTe are comparable to previous studies by conventional MBE [15,16]. The same result was also confirmed for the control of n-type conduction. Although the VI/II ratio is fixed, no difference between CSMBE and conventional MBE was observed in amphoteric doping.

Surface structure during CSMBE growth was studied by reflection high-energy electron diffraction (RHEED) observation. A clearly streaked (2×1) reconstructed pattern was observed
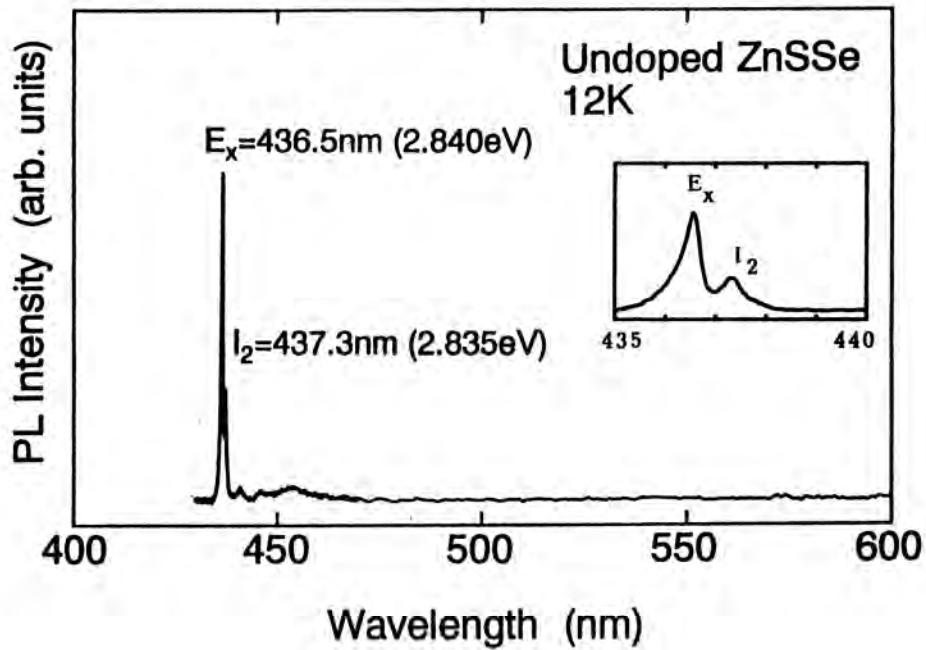
Fig. 3.6. 12 K PL spectra obtained from an undoped ZnSSe/GaAs film grown by CSMBE. The inset shows the spectrum around excitonic emissions.
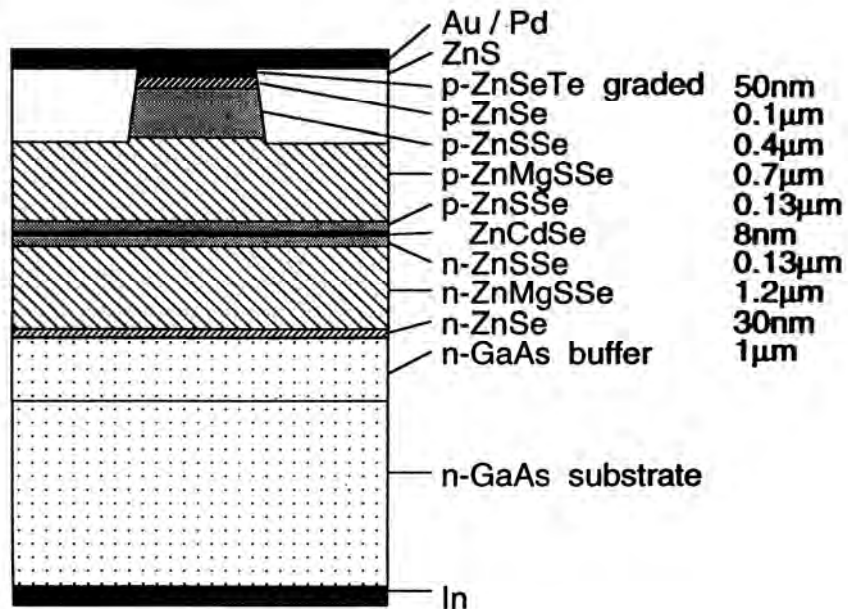

Fig. 3.7. Schematic structure of a ZnCdSe/ZnSSe/ZnMgSSe SQW-SCH quaternary LD.

for ZnSe, ZnSSe and ZnTe layers during the growth. It is found that the surfaces of these layers are anion-stabilized, in spite of the condition $J_{VI}/J_{II} = 1$. Intensities of the substreaks of ZnSSe, ZnSe and ZnTe surfaces increase in this order, indicating that the sticking coefficients of group VI elements on the growth front are in the order of S < Se < Te. In the case of conventional MBE, a Zn-stabilized surface was reported for MBE growth of ZnSe with $J_{Se}/J_{Zn} = 1$ at 280°C [17]. The growth mechanism of CSMBE will be different from conventional MBE because diatomic molecular beams of group VI elements are created in effusion cells containing compound sources [18].

The LD structure has the ZnCdSe/ZnSSe/ZnMgSSe single quantum well (SQW) separate confinement heterostructure (SCH), as shown in Fig. 3.7. Layer thicknesses were measured using a cross-sectional transmission electron microscope (TEM). The bandgap defined with band-edge emission of ZnMgSSe cladding layer is 2.93 eV at 12 K. Carrier concentrations for n- and p-type ZnSe, ZnSSe, ZnMgSSe layers are on the order of 10^{17} cm^{-3}.

Coherent light from the fabricated LD is observed at 513 nm under pulsed operation. The wavelength indicates that Cd content in the active layer is about 18%, and compressive strain of +1.5% exists in the layer. Cd content of ZnCdSe is almost the same as the beam pressure ratio of $P_{CdSe}/(P_{CdSe}+P_{ZnSe})$. Figure 3.8 shows light output power and current (*L-I*) characteristics of a LD under pulsed and CW operation. High-reflectivity (HR) coating of 92% and 99% was applied to the front and rear facets, respectively. The threshold current (I_{th}) under CW operation is 68 mA, corresponding to a threshold current density of 1.8 kA/cm^2. The threshold voltage is 12 V for both CW and pulsed operation. The differential quantum efficiency from both uncoated facets is 38% under pulsed operation. The CW operation for the uncoated device at room temperature has been demonstrated with $I_{th} = 143$ mA. The HR-coated LD was operated by CW mode under automatic power control; the light output from the front facet was set at 0.3 mW. The lifetime of the LD is around 1 s at room temperature as shown in Fig. 3.9.

Furthermore, ZnCdSe (6 nm)/ZnSSe (8 nm) quadruple quantum well SCH LDs were fabricated without facet coating and mounted with the junction-up configuration. The device lased at 518 nm at room temperature. Figure 3.10 shows the *L-I* characteristics of the device. The maximum light output power exceeded 300 mW per facet, which was limited by the power supply.
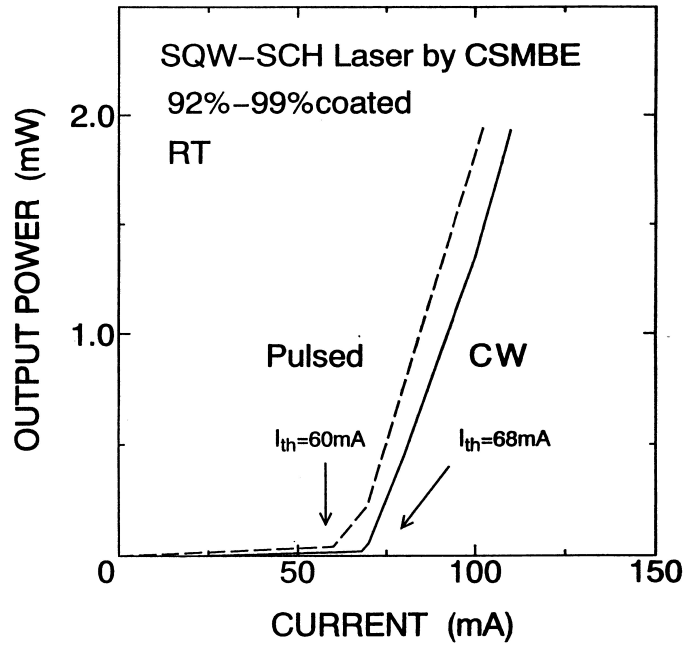
Fig. 3.8. Light output power versus injection current characteristics under pulsed and CW operation of an HR-coated ZnCdSe/ZnSSe/ZnMgSSe SQW-SCH LD at room temperature.
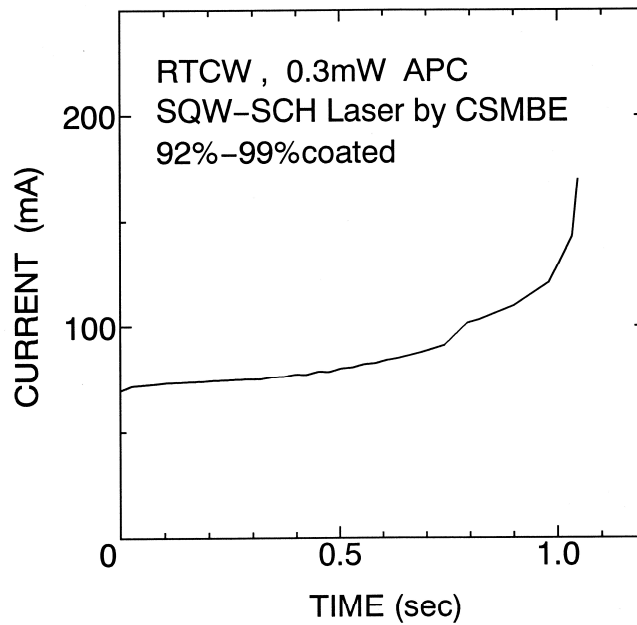

Fig. 3.9. Operating current of an HR-coated ZnCdSe/ZnSSe/ZnMgSSe SQW-SCH LD as a function of time under a constant output power of 0.3 mW at room temperature.
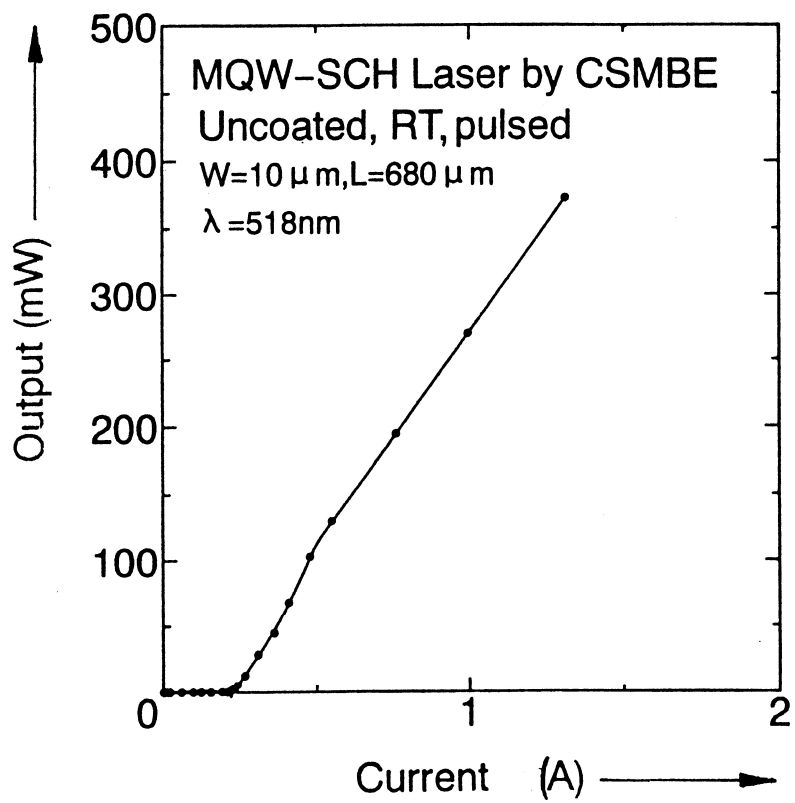
Fig. 3.10. Light output power versus injection current characteristics under pulsed operation of an uncoated ZnCdSe/ZnSSe/ZnMgSSe MQW-SCH LD at room temperature.

The structural defects in the LDs were mainly stacking faults generated at the II-VI/III-V interface at a density of 6×10^5 cm^{-2}. The origin of the defect was not determined by the TEM observation. Further study on the heterointerface will be necessary to reduce the dislocations.

Conclusion

ZnSe and related materials were grown by CSMBE. The doping level in CSMBE was the same as that in conventional MBE. Surface structure for binary and ternary alloys was anion-stabilized in spite of the condition $J_{VI}/J_{II} = 1$. Continuous-wave operation of a ZnCdSe/ZnSSe/ZnMgSSe SQW-SCH quaternary LD was demonstrated at room temperature. The fixed VI/II ratio around unity was concluded to be suitable for the growth of ZnSe-based LD structure.

References in 3.1.2

[1] T. Yao, S. Amano, M. Ogura, S. Matsuoka, and T. Morishita, *Appl. Phys. Lett.* **43**, 499 (1983).

[2] K. Ohkawa, T. Mitsuyu, and O. Yamazaki, *J. Appl. Phys.* **62**, 3216 (1987).

[3] K. Ohkawa, T. Karasawa, and T. Mitsuyu, *J. Cryst. Growth* **111**, 797 (1991).

[4] M.A. Haase, J. Qiu, J.M. DePuydt, and H. Cheng, *Appl. Phys. Lett.* **59**, 1272 (1991).

[5] N. Nakayama, S. Itoh, T. Ohata, K. Nakano, H. Okuyama, M. Ozawa, A. Ishibashi, M. Ikeda, and Y. Mori, *Electron. Lett.* **29**, 1488 (1993).

[6] A. Salokatve, H. Jeon, J. Ding, M. Hovinen, A. V. Nurmikko, D. C. Grillo, L. He, J. Han, Y. Fan, M. Ringle, R. L. Gunshor, G. C. Hua, and N. Otsuka, *Electron. Lett.* **29**, 2192 (1993).

[7] J. M. Gaines, R. R. Drenten, K. W. Haberern, T. Marshall, P. Mensz, and J. Petruzzello, *Appl. Phys. Lett.* **62**, 2462 (1993).

[8] Y. Fan, J. Han, L. He, J. Saraie, R. L. Gunshor, M. Hagerott, H. Jeon, A. V. Nurmikko, G. C. Hua, and N. Otsuka, *Appl. Phys. Lett.* **61**, 3160 (1992).

[9] J.Qiu, D. R. Merke, M. Kobayashi, R. L. Gunshor, Q.-D. Qian, D. Li, and N. Otsuka, *J. Cryst. Growth* **111**, 747 (1991).

[10] S. Itoh, N. Nakayama, S. Matsumoto, M. Nagai, K. Nakano, M. Ozawa, H. Okuyama, S. Tomiya, T. Ohata, M. Ikeda, A. Ishibashi, and Y. Mori, *Jpn. J. Appl. Phys.* **33**, L938 (1994).

[11] D. B. Holt, *Thin Solid Films* **24**, 1 (1974).

[12] D. L. Smith and V. Y. Picknardt, *J. Appl. Phys.* **46**, 2366 (1975).

[13] J. P. Faurie and A. Million, *J. Cryst. Growth* **54**, 577 (1981).

[14] T. Karasawa, K. Ohkawa, and T. Mitsuyu, *J. Appl. Phys.* **69**, 3226 (1991).

[15] J. Qiu, J. M. DePuydt, H. Cheng, and M. A. Haase, *Appl. Phys. Lett.* **59**, 2992 (1991).

[16] J. Han, T. S. Stavrinides, M. Kobayashi, R. L. Gunshor, M. M. Hagerott, and A. V. Nurmikko, *Appl. Phys. Lett.* **62**, 840 (1993).

[17] K. Menda, I. Takayasu, T. Minato, and M. Kawashima, *Jpn. J. Appl. Phys.* **26**, L1326 (1987).

[18] P. Goldfinger and M. Jeunehomme, *Trans. Faraday Soc.* **59**, 2851 (1963).

3.1.3. High-rate growth of laser structures by compound source MBE

Introduction

Molecular beam epitaxy (MBE) of high-quality II-VI films [1] and practical n-type doping of ZnSe by $ZnCl_2$ [2] and p-type doping of ZnSe by N_2 radicals [3] have led to the realization of ZnSe-based semiconductor lasers in blue-green region [4]. Continuous-wave (CW) operation of ZnSe-based lasers at room temperature was achieved [5-7] by using ZnMgSSe quaternary alloy [8]. The devices reported so far have been grown by conventional MBE which employs mainly elemental sources such as Zn, Se, Mg, Cd and Te [5]. With respect to the conventional MBE some difficulties exist in controlling the composition and the doping level of alloys due to the accuracy of relative intensity of three or more beam fluxes.

Ohkawa *et al.* have developed compound source MBE (CSMBE) for II-VI laser structures and achieved CW operation at room temperature [7]. The CSMBE technique employs polycrystalline compound sources instead of elemental sources. This enables the epitaxial growth of II-VI layers to reduce the number of source materials and to stabilize the group VI/II elemental impingement ratio around unity. Therefore, reproducibility and uniformity of ternary and quaternary alloys for the laser structure have been improved.

The CSMBE has additional potential to realize high-rate growth of II-VI films with high quality resulting from high kinetic energy of source molecules. The operation temperatures of effusion cells necessary to obtain beam flux for CSMBE growth are generally higher than those for the conventional MBE growth. For example while Zn and Se effusion cells are operated at 200-400°C, a ZnSe effusion cell is operated at 700-900°C. The kinetic energy of molecules produced from a ZnSe effusion cell is twice as high as that of molecules from Zn and Se effusion cells. Hot molecular beams expected to enhance the surface migration of adsorbed species at the growth front and to increase the tendency to two-dimensional growth. Consequently, the CSMBE is expected to maintain the surface morphology even at higher growth rate at which the surface morphology degrades in case of the conventional MBE growth. The growth rate of II-VI laser structures grown by the conventional MBE is as low as about 0.5 μm/h because higher growth rate causes rough surface morphology [9]. There is a dilemma that it takes more than 5 hours to grow the basic laser structure. In order to bring II-VI lasers to

commercial utility, the problem of low productivity for II-VI MBE growth has to be overcome. The CSMBE technique is possible to solve this problem.

In this section, I have studied the high-rate growth and the characterization of ZnSe:N, ZnMgSSe:N films and II-VI laser structures by using the CSMBE technique. In particular, the growth temperature dependence of the crystalline quality was investigated for ZnSe:N films.

Experimental

Source materials used are polycrystalline ZnSe (purity 6N), ZnS (5N), CdSe (6N), ZnTe (6N) and elemental Mg (6N) for the growth of II-VI layers. $ZnCl_2$ was used as an n-type doping source [2] and N radicals produced in a plasma source were used as a p-type doping source [3]. Growth rate for ZnSe:N films was intentionally fixed around 2 μm/h which was 2-4 times higher than the conventional growth rate. Practically it was distributed over 1.9-2.6 μm/h since the growth temperature for these films was varied from 200 to 400°C. The growth temperature was measured by an infrared pyrometer calibrated in advance from the oxide desorption temperature (582°C) of GaAs substrates. More than 5 μm-thick ZnSe:N films were grown in order to study the crystalline quality by the X-ray diffraction measurement and observation of the surface morphology. ZnMgSSe:N films and ZnSe-based laser structure were grown at 280°C with a growth rate of 2.6 μm/h on the basis of the characterization of ZnSe:N films. The laser structure was typical ZnCdSe/ZnSSe/ZnMgSSe separate confinement heterostructure (SCH).

All growths were performed on Si doped n-type GaAs (100) substrates that were chemically etched in $H_2SO_4 : H_2O_2 : H_2O = 8 : 1 : 1$, rinsed in deionized water and mounted on a molybdenum block by using indium. Prior to growth the substrates were thermally cleaned at 595°C for 15 min in the II-VI growth chamber without an exposure to arsenic flux except to grow the laser structures. GaAs:Si buffer layers were grown on the thermally cleaned substrate only for the growth of the laser structures in the III-V growth chamber interconnecting II-VI's via an ultrahigh vacuum transfer tube.

Surface structure during CSMBE growth was studied by reflection of high-energy electron diffraction (RHEED) observation. Surface morphology was observed by a Nomarski interference microscope. The growth rate of the layers was determined by a scanning electron microscope (SEM) measurement of the layer thickness. Crystalline quality was examined
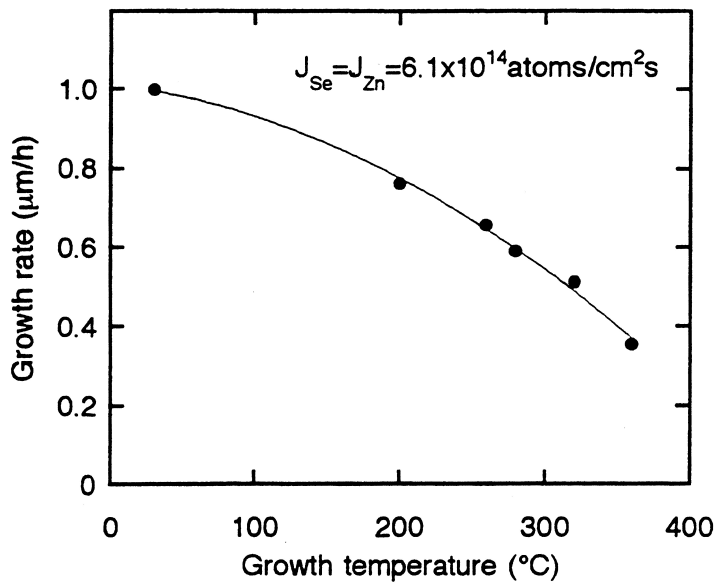
Fig. 3.11. Temperature dependence of the growth rate of ZnSe:N films grown by CSMBE. The growth rate is normalized for a molecular beam flux of 6.1×10^{14} Zn or Se atoms/cm^{2}s.
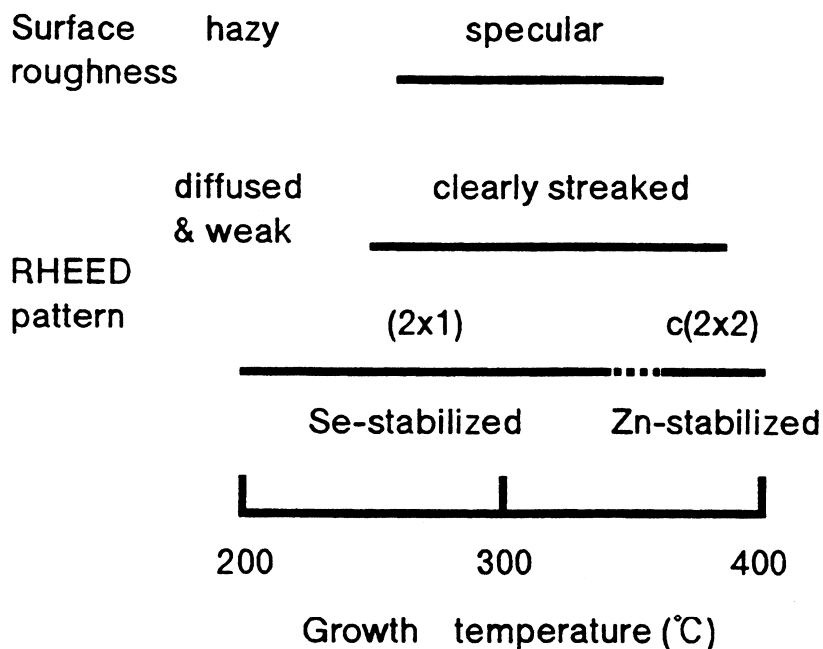

Fig. 3.12. RHEED pattern and surface roughness to the naked eye from ZnSe:N films grown by the high-rate CSMBE as a function of the growth temperature.

through the full width at half-maximum (FWHM) of double-crystal X-ray rocking curve (XRC) measurement for the (400) reflection. 15 K photoluminescence (PL) spectra were measured for ZnSe:N, ZnMgSSe:N films and the laser structures excited by the 325 nm line of a He-Cd laser with a power density of as low as 100 mW/cm^2. Net acceptor concentration (N_A-N_D) at room temperature was determined by the capacitance-voltage (*C-V*) measurement with the double-Schottky configuration of Al and Au for p- and n-type layers, respectively. The laser structure was observed by a cross-sectional transmission electron microscope (TEM).

The laser-structure wafer was processed into gain-guided devices with 5 μm-wide mesa stripe and 750 μm-long cavity. ZnO deposited by RF sputtering was used as an insulator. The device performance was measured at room temperature under pulsed operation using 700 ns-long pulses at a duty cycle of 0.07% without any heat sinks.

Results and discussion

(1) Characterization of ZnSe:N films grown by high-rate CSMBE

Figure 3.11 shows the temperature dependence of the growth rare of ZnSe:N films grown by CSMBE. The growth rate is normalized to a molecular beam flux of 6.1×10^{14} Zn or Se atoms/cm^{2}s. The linear dependence of the growth rate on the beam flux was satisfied between the previous works on CSMBE and this work. For example, the growth rate at a growth temperature of 260°C was obtained to be 2.0 μm/h for a beam flux of 1.9×10^{15} atoms/cm^{2}s. A ZnSe effusion cell was operated at 800-850°C for the high-rate growth. The operation temperature was around 50°C higher than that of the conventional growth rate. As the growth temperature increases, the surface lifetime of the species becomes shorter and the sticking coefficients smaller, so that the growth rate decreases.

The VI/II elemental impingement ratio and the growth temperature influence the surface reconstruction of the growth front. The VI/II ratio for CSMBE is fixed around unity, therefore the surface reconstruction depends strongly on the growth temperature. The surface reconstruction of ZnSe layer during the high-rate CSMBE was studied for various growth temperatures. The growth temperature dependence of the RHEED pattern from ZnSe layers are schematically shown in Fig. 3.12. A streaked (2 × l) pattern appeared during the growth in the temperature range of 200-340°C. This means that below 340°C the surface is Se-stabilized in
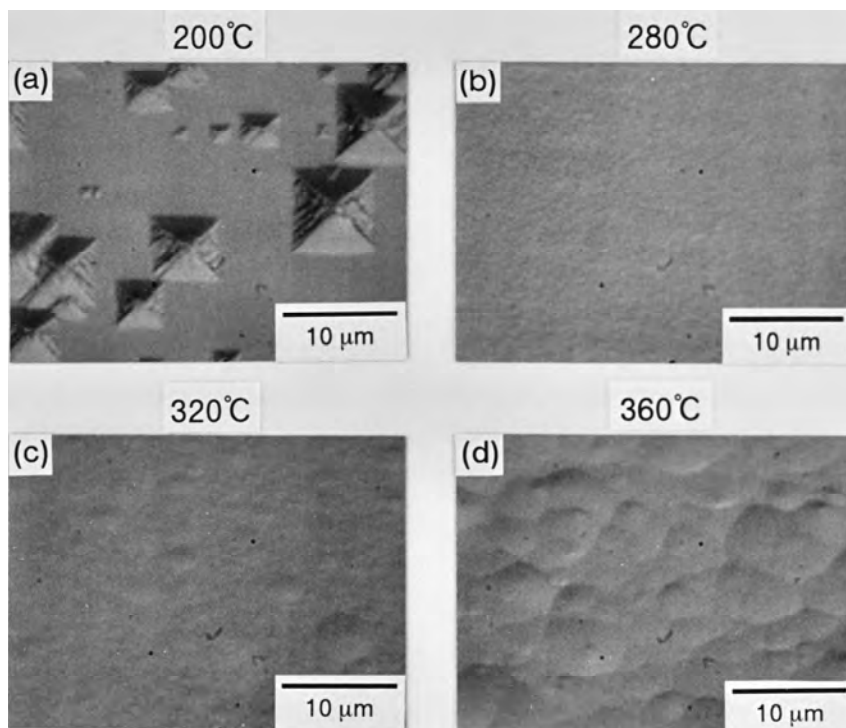
Fig. 3.13. Nomarski interference micrographs of around 5 μm-thick ZnSe:N films grown by the high-rate CSMBE at a growth temperature of (a) 200°C, (b) 280°C, (c) 320°C and (d) 360°C.
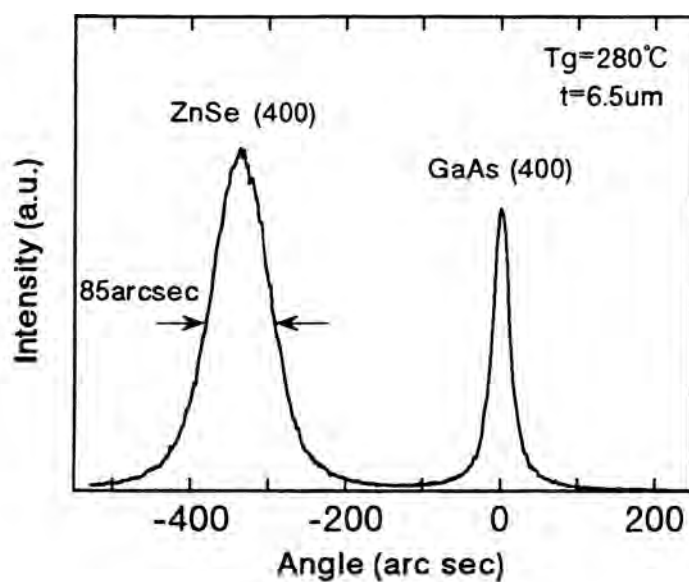

Fig. 3.14. Double-crystal X-ray rocking curve for a 6.5 μm-thick ZnSe:N film grown by CSMBE at a growth temperature of 280°C with 2.6 μm/h.

spite of the condition of VI/II = 1. This result is similar to that for the CSMBE at the conventional growth rate [7] and is different from that for the conventional MBE. In case of the conventional MBE, the surface of ZnSe is Zn-stabilized during the growth under the condition of VI/II = 1 [10]. The growth mechanism of CSMBE will be different from that of the conventional MBE. Se dimers are produced in CSMBE because ZnSe compound sublimes dissociatively as [11]:

$$ZnSe\,(solid) \rightarrow Zn\,(gas) + \frac{1}{2}Se_2\,(gas). \tag{3.2}$$
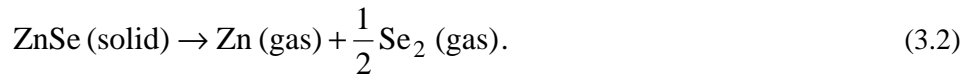
On the other hand, molecular species produced from elemental Se are $Se_6 : Se_5 : Se_7 : Se_2 : Se_8 =$ 1.00 : 0.66 : 0.28 : 0.11 : 0.04 in the partial pressure ratio at an operation temperature of 196°C [12]. It is known that the smaller Se species have lower sticking coefficient than the larger Se molecules by the growth of ZnSe using cracked selenium source [12,13]. Consequently, the surface migration of Se dimer is presumably enhanced due to its higher kinetic energy in case of the CSMBE. A streaked $c(2 \times 2)$ pattern was observed above 360°C. This is also similar to the result for the CSMBE at the conventional growth rate [7].

All samples except for a sample which was grown at 200°C had shiny and specular surfaces to the naked eye. The sample grown at 200°C in which diffused and weak (2×1) streak pattern was observed during the growth had hazy surface. Figure 3.13 shows Nomarski interference micrographs of ZnSe:N films grown at various growth temperatures. The sample grown at 200°C had square hillocks whose density was 2×10^6 cm^{-2} as shown in Fig. 3.13(a). Except for the hillocks, the surface flatness of this sample was best of all the samples grown in this work. The sample grown at 360°C had rough surface as shown in Fig. 3.13(d). Similar surface morphology has been observed for the samples grown with cracked selenium at growth temperatures of 300-350°C [13]. The rough surface of these samples is presumably caused by reduced surface migration length of adsorbed Se species resulting from shorter surface lifetime due to their high volatility. On the other hand, smooth morphology was observed for samples grown at 250-320°C as shown in Fig. 3.13(b) and (c). Degradation of the surface morphology attributed to the high-rate growth was not observed in comparison with the morphology of ZnSe films grown by CSMBE at the conventional growth rate.

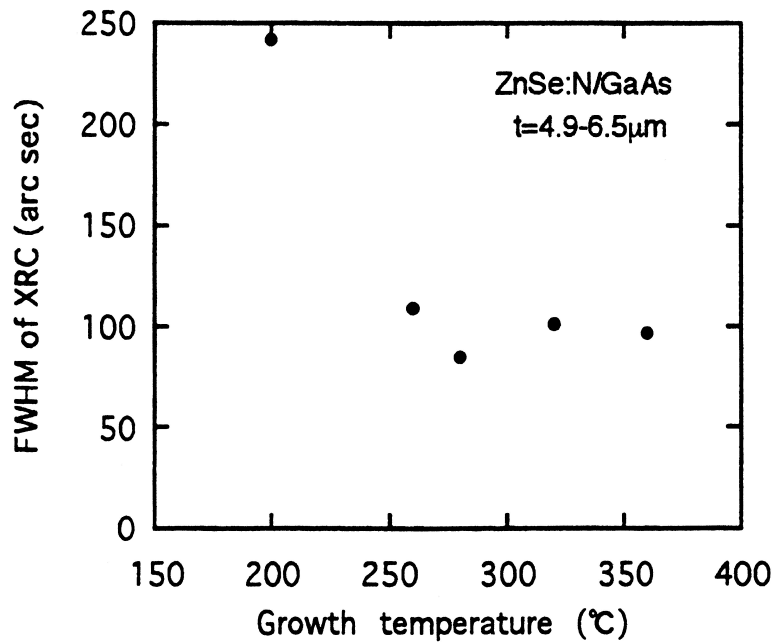Figure 3.14 shows double-crystal XRC for a 6.5 μm-thick ZnSe:N film grown at 280°C

Fig. 3.15. Growth temperature dependence of the FWHM of XRC (400) reflection for ZnSe:N films grown by the high-rate CSMBE.
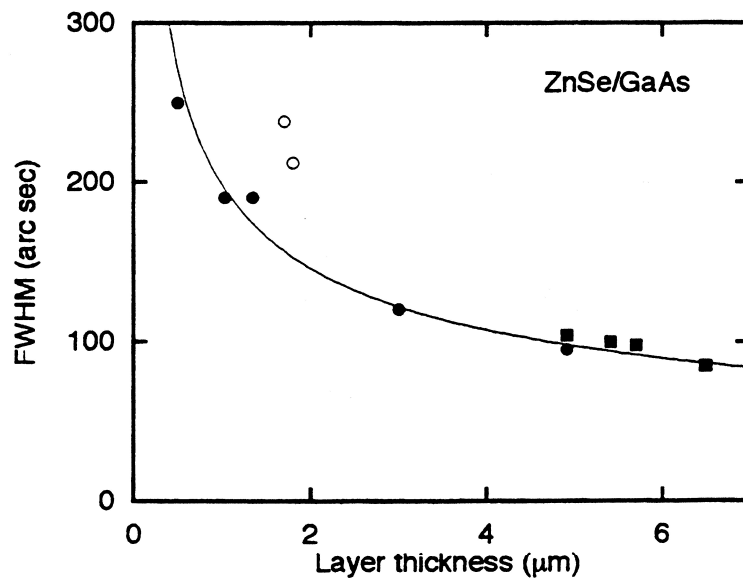

Fig. 3.16. Full width at half-maximum of XRC (400) reflection as a function of layer thickness for ZnSe films grown by the conventional MBE under Se/Zn elemental impingement ratio = 1 at 280-325°C with 0.4-0.6 μm/h (closed circles), with 2.5 μm/h (open circles) and grown by the CSMBE at 260-360°C with 1.9-2.6 μm/h (closed squares).

106

with 2.6 µm/h. The FWHM of ZnSe (400) reflection was as narrow as 85 arcsec. The growth temperature dependence of the FWHM of (400) reflection is shown in Fig. 3.15. The FWHMs were 85-109 arcsec for growth temperatures of 260-360°C, and did not depend on the growth temperature except for a growth temperature of 200°C. It is well established that an FWHM of around 100 arcsec is obtained for around 5 µm-thick high-quality ZnSe film grown on GaAs substrate [2]. Therefore, high-quality ZnSe films were obtained even for the high-rate growth around 2 µm/h by using the CSMBE. The FWHM for a sample grown at 200°C was as wide as 242 arcsec due to the presence of large volume of the hillocks. The FWHM as a function of the film thickness is shown in Fig. 3.16 in order to clear the crystalline quality of the films grown by the high-rate CSMBE. The data indicated by closed and open circles were taken from ZnSe films grown by the conventional MBE with a growth rate of 0.4-0.6 µm/h and 2.5 µm/h, respectively, under Se/Zn elemental impingement ratio = 1 at a growth temperature of 280-325°C [2]. The data indicated by closed squares were taken from this work (the CSMBE at a growth temperature of 260-360°C with a growth rate of 1.9-2.6 µm/h). Closed squares are plotted on a curved line suggesting that the crystalline quality obtained by the high-rate CSMBE is comparable to the high-quality ZnSe films grown by the conventional MBE. In case of the conventional MBE higher growth rate, however, caused the degradation of the crystalline quality. The samples had rough surface morphology due to three-dimensional island growth suggesting that the surface migration of adatoms is insufficient under this growth condition. These results show that CSMBE technique keeps the crystalline quality even at the high growth rate more than 2 µm/h, where the conventional MBE has not realized. CSMBE has the effect of enhancing the surface migration of adsorbed species at the growth front due to high kinetic energy of source molecules.

Figure 3.17 shows 15 K PL spectra for two typical samples of ZnSe:N films grown by the high-rate CSMBE. Lightly doped films as shown in Fig. 3.17(a) were grown under the doping condition which is applied to obtain an N_A-N_D of mid 10^{17} cm^{-3} at the conventional growth rate. They exhibit so-called shallow donor-acceptor pair (DAP) emission at 2.70 eV with LO-phonon replicas, recombination emission between free electrons and acceptor holes (FA) at 2.7l eV with LO-phonon replicas, free and acceptor-bound exciton (E_X and I_1) emissions at 2.80 and 2.79 eV, respectively, and the absence of the Y line (at 2.602 eV) nor any deep level emissions. This
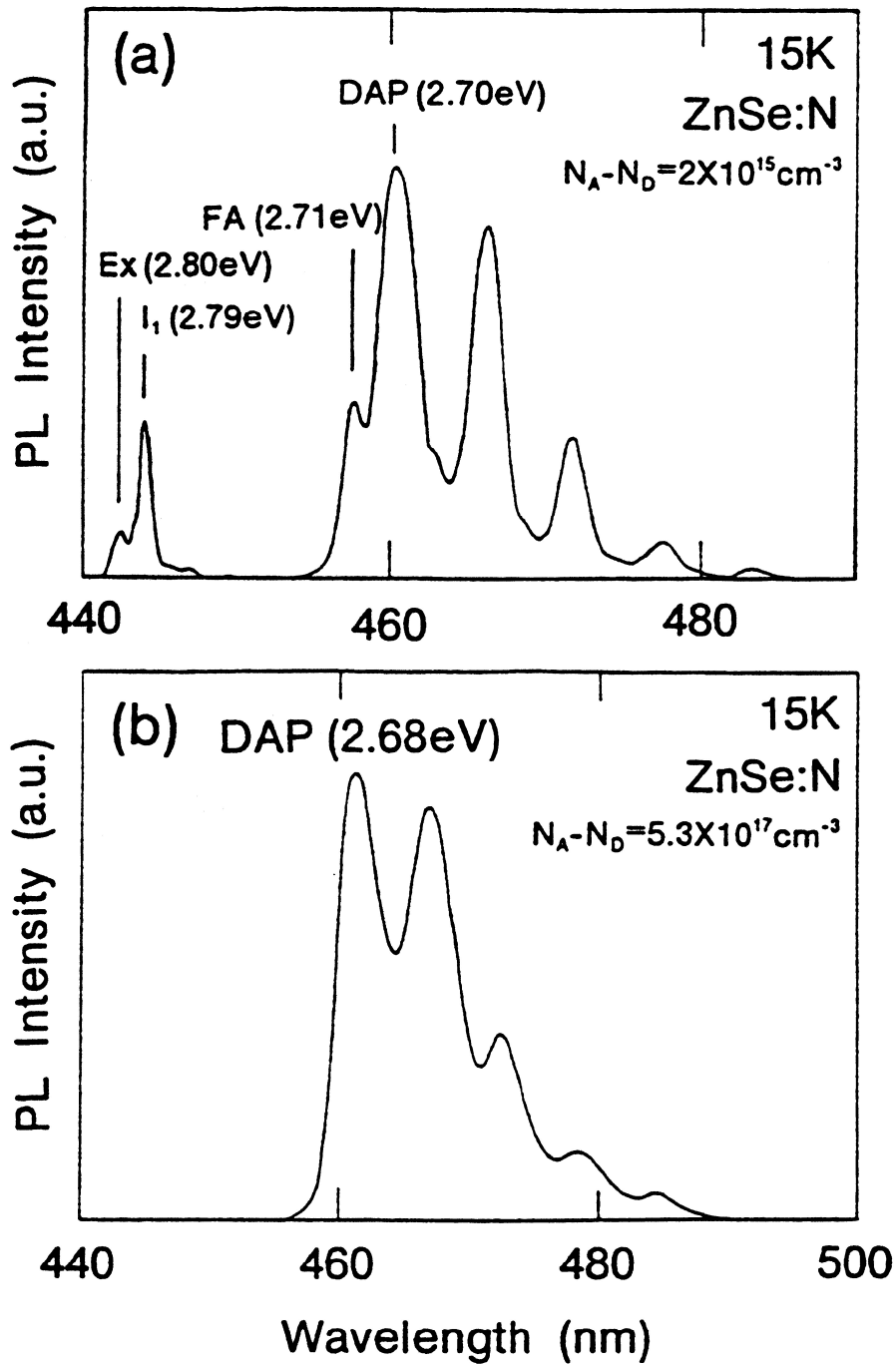
Fig. 3.17. 15 K PL spectra for ZnSe:N films grown by the high-rate CSMBE under (a) lightly doping condition and (b) p-type doping condition.

spectrum also supports that ZnSe:N film grown by the high-rate CSMBE has high crystalline quality. The N_A-N_D of these films were as low as of the order of 10^{15} cm^{-3}. Accordingly the concentration of nitrogen radical in N$_2$ plasma was improved by decreasing the flow rate of N$_2$ gas [3] and increasing the input RF power during the high-rate CSMBE growth. Dominant so-called deep DAP emission at 2.68 eV was observed with LO-phonon replicas as shown in Fig. 3.17(b) for ZnSe:N films grown with higher concentration of nitrogen radical in N$_2$ plasma The N_A-N_D of these films is of the order of 10^{17} cm^{-3}. These results show that even for the high-rate growth the doping level of nitrogen is able to control over wide range by changing the flow rate of N$_2$ gas and the RF power. In addition, it is desirable that lowering the flow rate of N$_2$ leads to reduce the background pressure to the order of 10^{-7} Torr at the growth chamber.

(2) Characterization of ZnMgSSe:N films and ZnMgSSe quaternary laser diodes

Since ZnSe:N films grown at 280°C had highest quality overall, the growth temperature of ZnMgSSe:N films and ZnSe-based laser structures was fixed at this temperature. A growth rate of 2.6 μm/h for ZnMgSSe:N films was adopted on the basis of 2.0 μm/h for ZnSe:N films.

A clearly streaked c(2 × 2) RHEED pattern was observed during the growth of ZnMgSSe:N films. This indicates that the VI/II ratio is less than unity due to the simultaneous impingement of ZnSe, ZnS and Mg at the growth front. Figure 3.18 shows a Nomarski interference micrograph of ZnMgSSe:N film. Mirror-like surface was obtained except the hillocks unique for ZnMgSSe grown by CSMBE [14]. The 'bow tie' hillock corresponds to a pair of stacking faults originated from the II-VI/GaAs interface. The density of the stacking faults (the order of 10^5 cm^{-2}) did not depend the growth rate.

The FWHM of XRC for ZnMgSSe:N films nearly lattice-matched to GaAs were less than 40 arcsec. The uniformity of alloy composition was maintained within 2 inches wafer. PL spectra and the *C-V* properties also suggests that ZnMgSSe:N films grown at the high rate have high crystalline quality comparable to that of the films grown at the conventional rate. The successful growth of ZnMgSSe alloy films by the high-rate CSMBE is attributed to the surface migration enhancement effect resulting from the fact that Zn and Se which are main constituent elements of the alloy are supplied from ZnSe compound source with high kinetic energy, since ZnS and Mg are common source materials between the CSMBE and the conventional MBE on
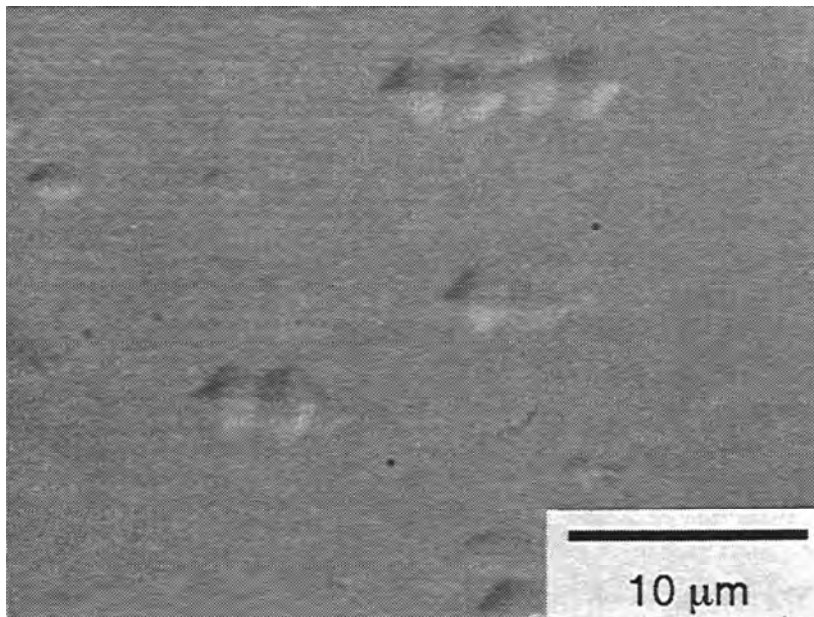
Fig. 3.18. Nomarski interference micrograph of a ZnMgSSe:N film grown CSMBE at 280°C with 2.6 μm/h.
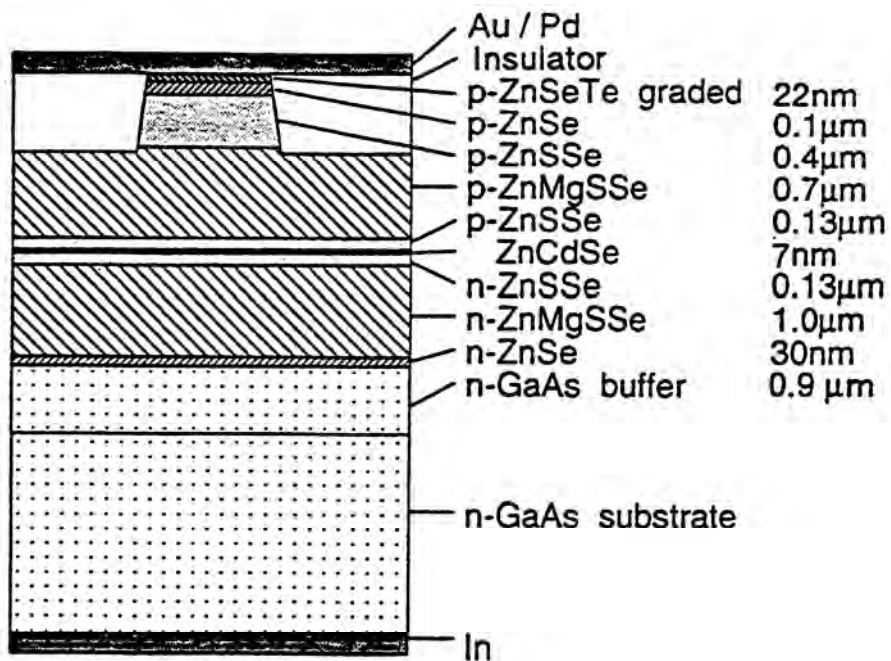

Au / Pd	
Insulator	
p-ZnSeTe graded	22nm
p-ZnSe	0.1μm
p-ZnSSe	0.4μm
p-ZnMgSSe	0.7μm
p-ZnSSe	0.13μm
ZnCdSe	7nm
n-ZnSSe	0.13μm
n-ZnMgSSe	1.0μm
n-ZnSe	30nm
n-GaAs buffer	0.9 μm
n-GaAs substrate	
In	

Fig. 3.19. Schematic structure of a ZnCdSe/ZnSSe/ZnMgSSe SCH quaternary laser diode.

The figure shows a plot with axes labeled "Output power (mW)" (vertical, 0 to 40) and "Current (mA)" (horizontal, 0 to 200). The annotations on the plot read:

27℃, Pulsed
Uncoated
L=750μm
w=5μm
λ=513nm
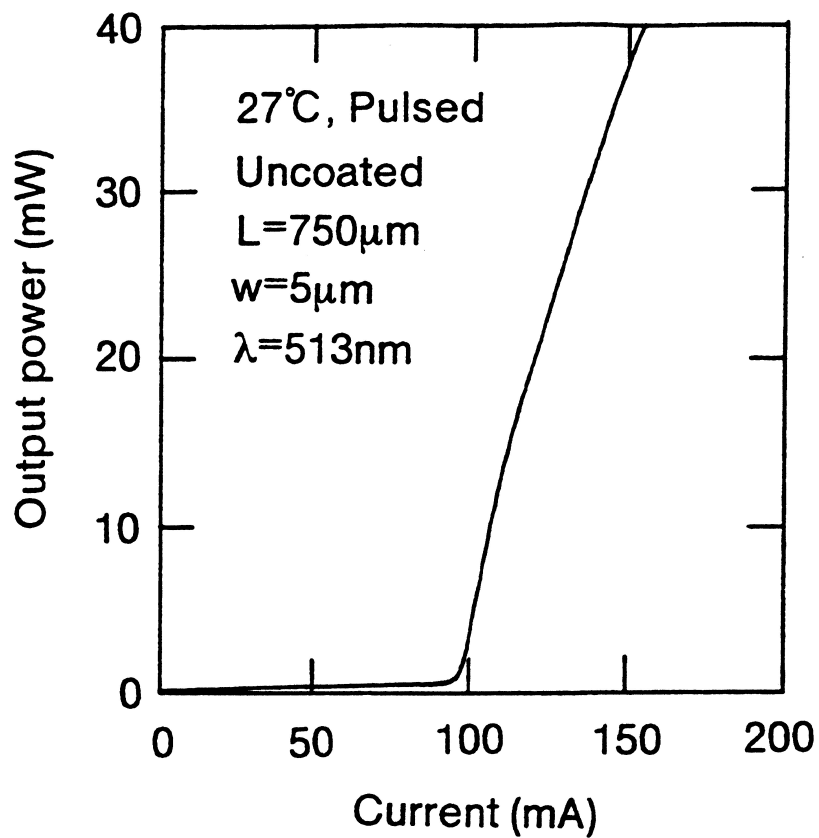
Fig. 3.20. Light output power versus injection current characteristics under pulsed operation of a ZnCdSe/ZnSSe/ZnMgSSe SCH quaternary laser diode at room temperature.

the growth of ZnMgSSe alloy.

The II-VI laser structure consists of ZnCdSe/ZnSSe/ZnMgSSe SCH as shown in Fig. 3.19. It took only 80 min to grow the II-VI laser structure. The bandgap defined with band-edge emission for ZnMgSSe cladding layer was around 2.90 eV at 15 K. Carrier concentrations for n- and p-type ZnSe, ZnSSe, ZnMgSSe layers were of the order of 10^{17} cm^{-3}. Surface of the laser structure had same morphology as that of ZnMgSSe:N films. Although the growth rate for ZnCdSe active layer attained 3.7 μm/h that was the highest rate in the laser structure, interfaces of the active layer appeared abrupt and flat by the cross-sectional TEM observation. 15 K PL spectrum from the active layer showed an FWHM of 11 meV. This value is comparable to that of the active layer grown at the conventional growth rate. Figure 3.20 shows light output versus injection current characteristics for a laser diode at 27°C. The threshold current density, the operation voltage and the differential quantum efficiency were around 2 kA/cm^2, 13 V and 58%, respectively.

These values are similar to those of the laser devices grown by CSMBE at the conventional rate. High growth rate of 2-3 μm/h did not lower the device performance. The CSMBE technique solves the problem of low productivity for the conventional II-VI MBE growth.

Conclusion

High-rate growth of ZnSe films and related laser structures was investigated by using CSMBE. A clearly-streaked (2 × 1) pattern indicating Se-stabilized surface was observed by RHEED during the growth of ZnSe:N films at 260-320°C with around 2 μm/h. The FWHM of double-crystal XRC was as narrow as 85 arcsec for a 6.5 μm-thick film with mirror-like surface morphology. ZnCdSe/ZnSSe/ZnMgSSe separate confinement heterostructure lasers operated at room temperature were obtained with a time required to grow of 80 min. II-VI layers grown by the high-rate CSMBE had high crystalline quality comparable to that of the layers grown at the conventional growth rate. Compound source MBE has the surface migration enhancement effect at the growth front due to high kinetic energy of source molecules. The CSMBE technique solves the problem of low productivity for the conventional II-VI MBE growth.

References in 3.1.3

[1] T. Yao, S. Amano, M. Ogura, S. Matsuoka, and T. Morishita, *Appl. Phys. Lett.* **43**, 499 (1983).

[2] K Ohkawa, T. Mitsuyu, and O. Yamazaki, *J. Appl. Phys.* **62**, 3216 (1987).

[3] K. Ohkawa, T. Karasawa, and T. Mitsuyu, *J. Cryst. Growth* **111**, 797 (1991).

[4] M. A. Haase, J. Qiu, J. M. DePuydt, and H. Cheng, *Appl. Phys. Lett.* **59**, 1272 (1991).

[5] N. Nakayama, S. Itoh, T. Ohata, K. Nakano, H. Okuyama, M. Ozawa, A. Ishibashi, M. Ikeda, and Y. Mori, *Electron. Lett.* **29**, 1488 (1993).

[6] A Salokatve, H. Jeon, J. Ding, M. Hovinen, A. V. Nurmikko, D. C. Grillo, L. He, J. Han, Y. Fan, M. Ringle, R. L. Gunshor, G. C. Hua, and N. Otsuka, *Electron. Lett.* **29**, 2192 (1993).

[7] K. Ohkawa, S. Yoshii, H. Takeishi, A. Tsujimura, S. Hayashi, T. Karasawa, and T. Mitsuyu, *Jpn. J. Appl. Phys.* **33**, L1673 (1994).

[8] H. Okuyama, K. Nakano, T. Miyajima, and K. Akimoto, *J. Cryst. Growth* **117**, 139 (1992).

[9] T. Yao, T. Sera, Y. Makita, and S. Maekawa, *Surf. Sci.* **86**, 120 (1979).

[10] K. Menda, I. Takayasu, T. Minato, and M. Kawashima, *Jpn. J. Appl. Phys.* **26**, L1326 (1987).

[11] P. Goldfinger and M. Jeunehomme, *Trans. Faraday Soc.* **59**, 2851 (1963).

[12] H. Cheng, J. M. DePuydt, M. A. Haase, and J. E. Potts, *J. Vac. Sci. Technol. B* **8**, 181 (1990).

[13] D. A. Cammack, K. Shahzad, and T. Marshall, *Appl. Phys. Lett.* **56**, 845 (1990).

[14] K. Ohkawa, A. Tsujimura, T. Nishikawa, S. Yoshii, T. Yokogawa, M. Kubo, and Y. Sasai, *J. Cryst. Growth* **159**, 632 (1996).

3.2. Reduction of dislocations in GaN films by air-bridged lateral epitaxial growth

3.2.1. Air-bridged lateral epitaxial growth of GaN with low dislocation density

Introduction

The studies on lateral epitaxial overgrowth (LEO) and pendeo-epitaxy (PE) of group III–nitrides via metalorganic vapor phase epitaxy (MOVPE) or hydride vapor phase epitaxy have recently attracted more and more attention, since they are extremely effective in reducing the threading dislocation density (TDD) in GaN films on sapphire [1-5], SiC [6-10] and Si substrates [11]. The device lifetime as long as 10,000 h for the continuous-wave operation at 20°C under a constant output power of 2 mW has been demonstrated for the violet laser diodes using InGaN-based multiple quantum well grown on the LEO-GaN on sapphire substrates [12], which suggests that reducing TDD in GaN is a most promising way in which higher performance of GaN-based devices can be realized. On the other hand, it has been reported that the wing tilt of LEO-GaN is related to the strain between the LEO-GaN films and the mask materials [13] as well as the ratio of lateral to vertical growth, which depends on the growth conditions such as temperature, pressure, V/III ratio, and ambient gas [5,14]. The tilt angles of the wing regions, which are commonly larger than 0.1° for thin GaN films [4,5,15,16], can be characterized by using X-ray diffraction (XRD) for the (0002) peak.

In this section, I describe a promising technique of selected area growth combined with LEO, namely air-bridged lateral epitaxial growth (ABLEG) using low-pressure MOVPE method, which has been developed for not only reduction in TDD but also decrease in the influence of mask materials, that is, low wing tilt. In order to exclude the strain between the wing regions and the mask material, the air gap was introduced between the wing and the mask. By using ABLEG, high-quality GaN films with an atomically smooth surface, low TDD and low wing tilt of the *c*-axis have been successfully obtained.
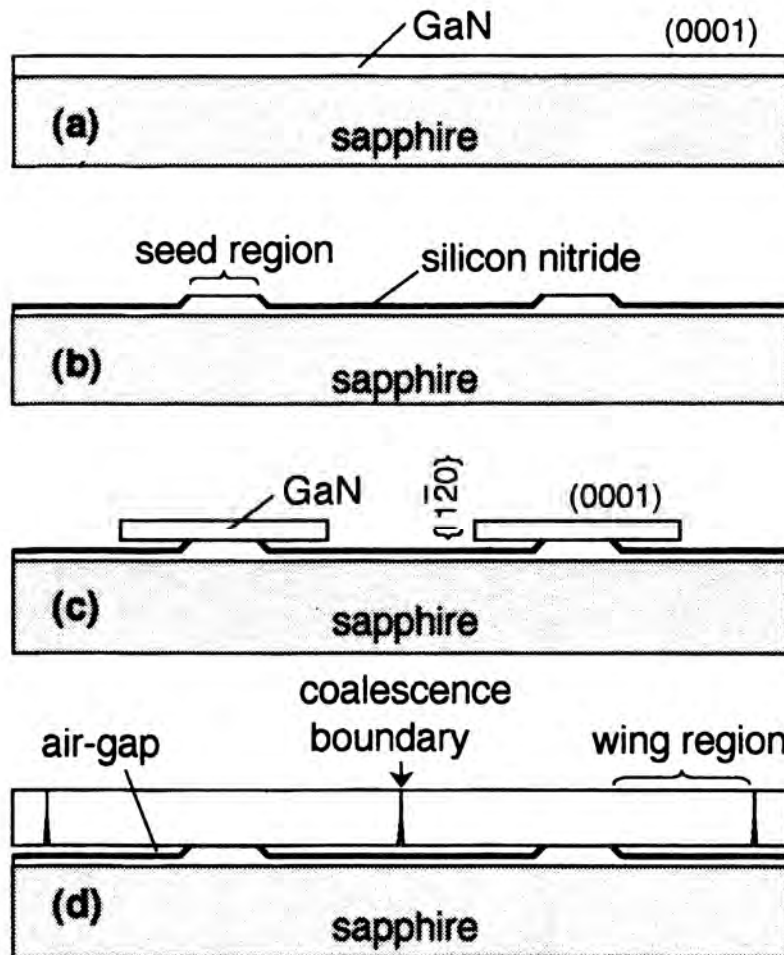
Fig. 3.21. Schematic of the procedure for air-bridged lateral epitaxial overgrowth. (a) MOVPE of GaN layer on sapphire substrate, (b) dry etching of GaN layer to form alternating ridges and trenches whose sidewalls and bottoms are covered with silicon nitride mask, (c) regrowth of GaN, and (d) continued regrowth to coalesce.

Experimental

Figure 3.21 shows the schematic of the fabrication procedure for air-bridged LEO. To achieve air-bridged LEO, a 1.2 μm-thick (0001) GaN layer was first grown on (0001) sapphire substrate by low-pressure MOVPE [Fig. 3.21(a)]. The GaN film was grooved along the $\langle 1\bar{1}00 \rangle$ $_{GaN}$ direction using conventional photolithography technique and dry etching process. The width and the period of the ridge stripes are 3 and 15 μm, respectively. Next the etched bottoms of the trenches and the sidewalls of the trapezoid ridge stripes were covered with 10 nm-thick silicon nitride mask, which was deposited using sputtering at room temperature [Fig. 3.21(b)]. The top surfaces of the ridges were exposed for GaN regrowth. The regrowth was carried out at growth temperatures of 900-970°C and a reactor pressure of 200 Torr using a conventional horizontal MOVPE system. The flow rates of trimethylgallium and NH_3 during regrowth were 1.3×10^{-4} mol/min and 3.5 slm (0.16 mol/min), respectively, resulting in V/III ratio of 1200. The carrier gas was a mixture of N_2 and H_2. At an optimum growth temperature, a GaN layer was vertically grown in the initial stage and lateral epitaxial growth over the mask from the newly shaped $\{11\bar{2}0\}$ facets was followed [Fig. 3.21(c)]. As a result of continued lateral growth, coalescence of the GaN wings occurred and the air-bridged structure was constructed [Fig. 3.21(d)]. The mode of air-bridged LEO is similar to mode B in PE [6] and "maskless" LEO [19].

In ABLEG, only the top surfaces of the ridge structures are used as seed crystals, while the side walls of those are in PE. The crystalline quality near the interface with the substrates is usually low, that is, high TDD and tilt and twist of c-axis [17]. In ABLEG, the seed crystals with high crystalline quality can be used by growing thick films.

The obtained ABLEG-GaN was characterized by scanning electron microscopy (SEM), transmission electron microscopy (TEM), atomic force microscopy (AFM), and XRD measurements. The SEM measurements were performed for the as-cleaved samples using a HITACHI S-5000 field-emission microscope operating at 15 kV, and the TEM measurements were used to observe the threading dislocations using TOPCON EM-002B operating at 200 kV. The surface topography was analyzed by AFM measurements in tapping mode using a Digital Instruments Dimension 3100 scanning probe microscope. The ω-scan XRD measurements were performed on the GaN (0002) plane using double-crystal X-ray diffractometer (Rigaku RU300).
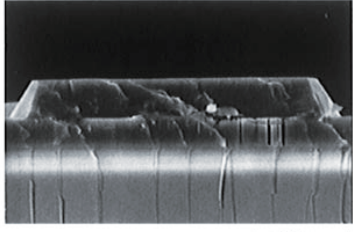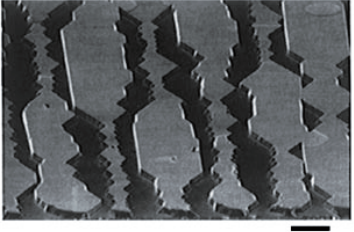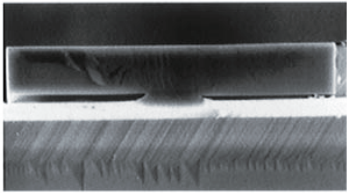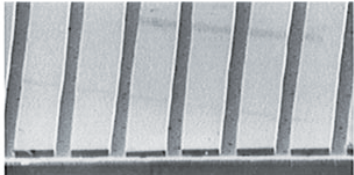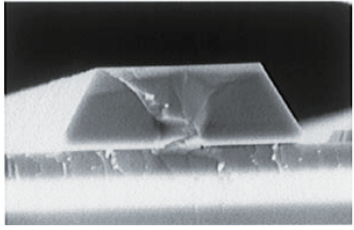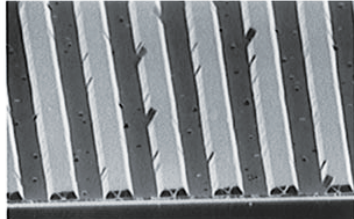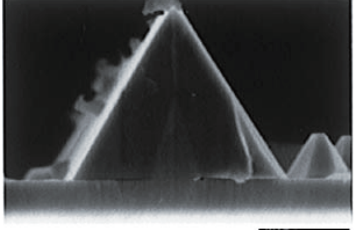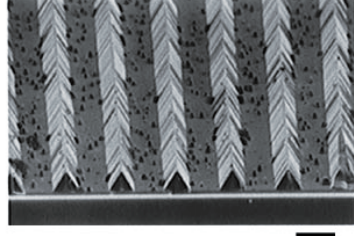
| Temperature (℃)	Cross sectional view [1$\bar{1}$00] surface	Bird's-eye view [0001] surface
970	3μm	10μm
950	3μm	10μm
930	3μm	10μm
900	3μm	10μm

Fig. 3.22. Cross-sectional and bird's-eye view SEM images for the GaN films grown at various growth temperatures.

Results and discussion

Figure 3.22 shows the cross-sectional and the bird's-eye view SEM images for the GaN films grown at various growth temperatures. At 900°C, the inclined $\{11\bar{2}2\}$ facets were dominantly formed, and the polycrystalline GaN particles were deposited on the silicon nitride mask. With increasing temperature, the $\{0001\}$ and $\{11\bar{2}0\}$ facets appeared and lateral growth became dominant. At 950°C, the rectangular cross-section formed with both the $\{0001\}$ and $\{11\bar{2}0\}$ facets was observed. The air gaps existed between the $(000\bar{1})$ GaN facets and the silicon nitride mask surfaces, except seed regions. At 970°C, the GaN $\{11\bar{2}0\}$ facets disappeared and the side walls of the GaN films were not uniform. Therefore, it was found that the growth at 950°C was effective in forming the air-bridged structure with a smooth surface, when the coalescence between the GaN wings occurred by continuing the growth.

In order to observe the growth rates in the $\langle1\bar{1}00\rangle$ and $\langle11\bar{2}0\rangle$ directions, the growth of the GaN films with AlGaN markers was performed at 950°C, as shown in Fig. 3.23. The growth times for the GaN and AlGaN layers were 45 and 15 min, respectively. The Al content was about 5%. Figure 3.23(a) shows the cross-sectional SEM image of the GaN films with the AlGaN markers. Figure 3.23(b) is an enlarged image about the wing part surrounded with the broken lines of Fig. 3.23(a). The rectangular interfaces formed with the GaN $\{0001\}$ and $\{11\bar{2}0\}$ facets were observed at each AlGaN marker. It was found that the GaN $\{0001\}$ and $\{11\bar{2}0\}$ facets were grown just at the initial stage of the regrowth. At the initial stage of the regrowth, the growth rates in the $\langle0001\rangle$ and $\langle11\bar{2}0\rangle$ directions are almost equal. Then, the growth rates in the $\langle0001\rangle$ direction decreased. This result indicates that the GaN layer is vertically grown just at the initial stage of the regrowth effectively, and then lateral epitaxial growth in the $\langle11\bar{2}0\rangle$ direction becomes dominant, compared with the vertical growth.

Figure 3.24 shows the cross-sectional SEM image of the GaN film after the coalescence has occurred, and the air-bridged structure has been constructed. Smooth surface was obtained not only in the wing region, but also in the vicinity of the coalescence region. The tapered voids were formed below the coalescence boundary surfaces. The thickness along the $\langle0001\rangle$ direction is 2.5 μm in the wing region and the aspect ratio (length/thickness of the wing) is 2.4. This value is 4 times larger than that of LEO-GaN whose growth conditions were tailored in order to obtain low wing tilt [5]. Figure 3.25 shows the bird's-eye view SEM images for the
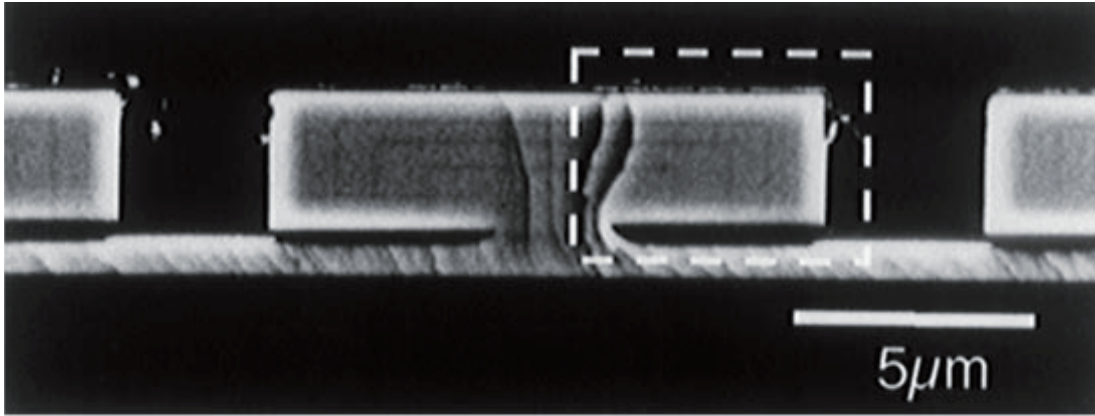
(a)
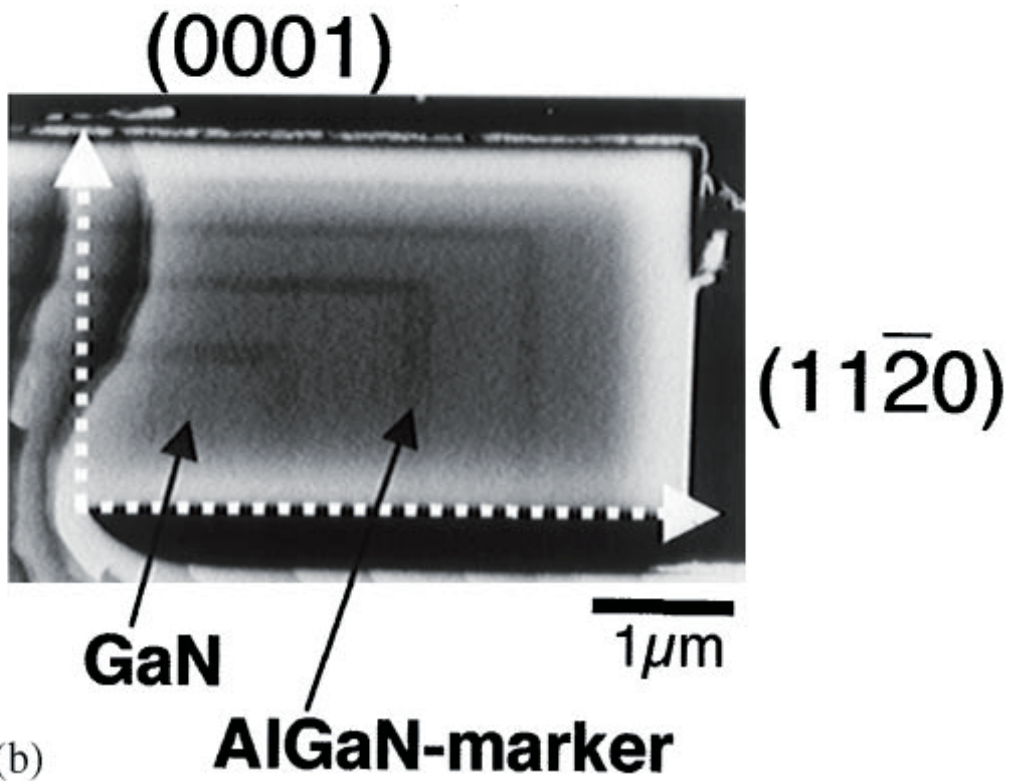
(b)

Fig. 3.23. (a) Cross-sectional SEM image of the GaN films with the AlGaN markers.
(b) Enlarged image about the wing part surrounded with the broken lines in (a).
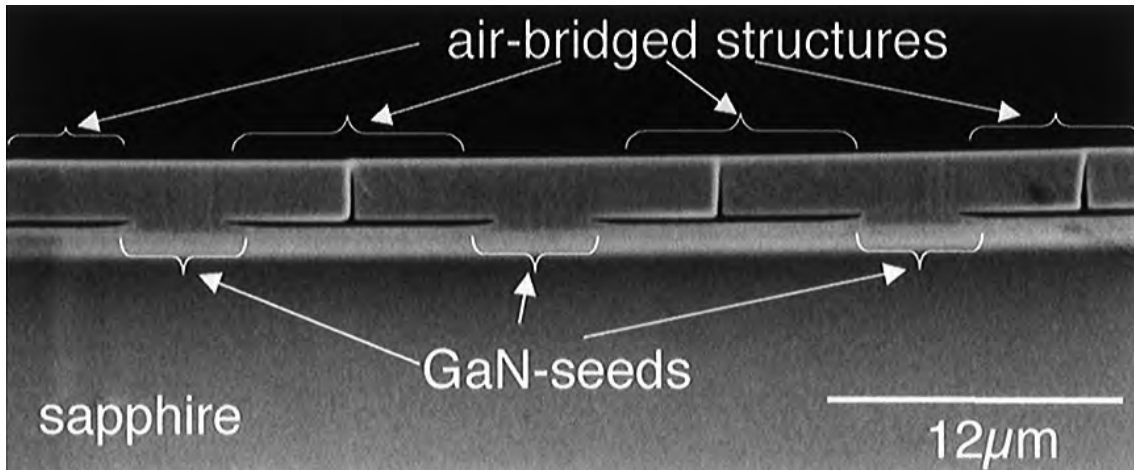
119

Fig. 3.24. Cross-sectional SEM image of the GaN film after coalescence. Air-bridged structure is constructed.
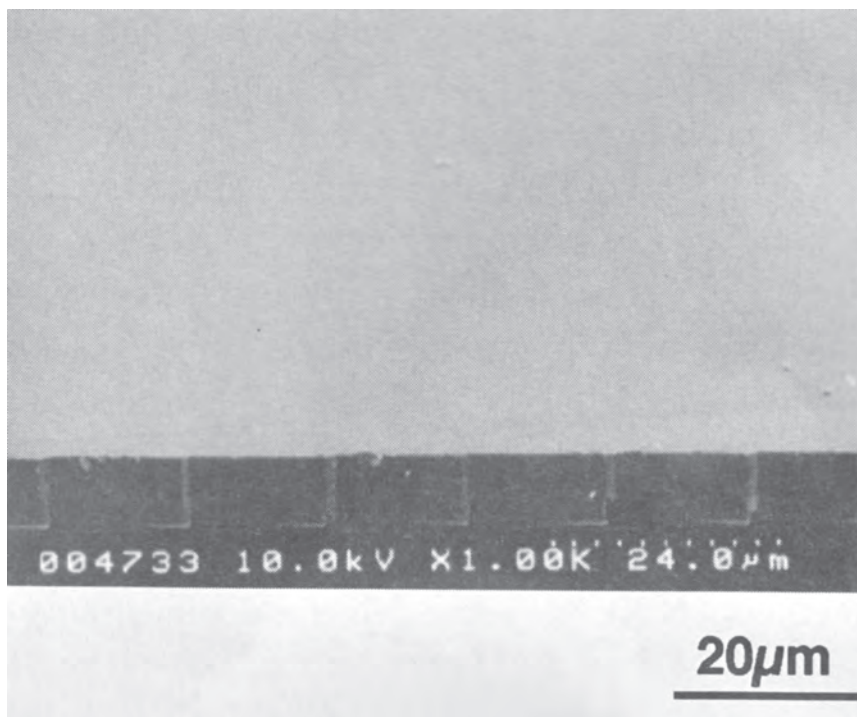

Fig. 3.25. Bird's-eye view SEM image of the surface of ABLEG-GaN film after coalescence.

ABLEG-GaN film with additional growth along the $\langle 0001 \rangle$ direction. The thickness is 8.5 μm. The ABLEG-GaN has a flat surface and no cracks are observed.

Figure 3.26 shows the results about the XRD measurements of a 2.5 μm-thick ABLEG-GaN (0002) peak for $\phi = 0°$ (incident X-ray perpendicular to ridge-stripe) (a), and $\phi = 90°$ (parallel) (b), where the azimuth ϕ is the angle between the stripe direction and the rotation axis in ω-scan. The peak splitting of (0002) GaN for $\phi = 0°$ is due to the crystalline tilting of the c-axis toward the $\langle 11\bar{2}0 \rangle$ direction, since the XRD curve has a single peak for $\phi = 90°$. The tilt angle of the c-axis relative to the underlying GaN is about 297 arcsec (0.083°), as shown in Fig. 3.26(a). The full width at half-maximum (FWHM) of the XRD curve is 175 arcsec for $\phi = 90°$ and that for one side of the two main peaks is 138 arcsec for $\phi = 0°$. These values are about half of those for the GaN films with low-temperature buffer layer on sapphire substrates, indicating that ABLEG-GaN has extremely high uniformity of c-axis orientation. The tilt angle is relatively small, compared with LEO [5], in spite of the large aspect ratio of 2.4. The reason why ABLEG-GaN exhibits small wing tilt and high uniformity of c-axis orientation is not fully clear at present. However, it is considered that the air gaps are effective in making the ABLEG-GaN free from the strain between the wing and the mask material. In fact, the wing tilt of the LEO-GaN film, which was grown under the same condition, was about 3.5 times larger than that of the ABLEG-GaN.

The cross-sectional TEM image is shown in Fig. 3.27(a). The threading dislocations were confined only in the seed regions, and no bending to the wing regions was observed. As a result, TDD in the wing region was decreased dramatically. At the coalescence boundary, the dislocations were newly generated near the top of the tapered voids. However, few dislocations along the c-axis were observed. The low wing tilt may be related with no bending of the threading dislocations to the wing regions. When the wing tilt is reduced, the adjoined wings can coalesce smoothly. As a result, the generation of threading dislocations is suppressed at the coalescence boundary. The dislocation densities of each region were estimated from the plan-view TEM image shown in Fig. 3.27(b). The densities of the vertical dislocations (parallel to the c-axis) were about 9×10^8 cm^{-2} in the seed region, while below 1×10^6 cm^{-2} in other regions. The densities of the horizontal dislocations (perpendicular to the c-axis) were about 1×10^6 cm^{-2} in the wing region, 4×10^7 cm^{-2} in the vicinity of the coalescence boundary,
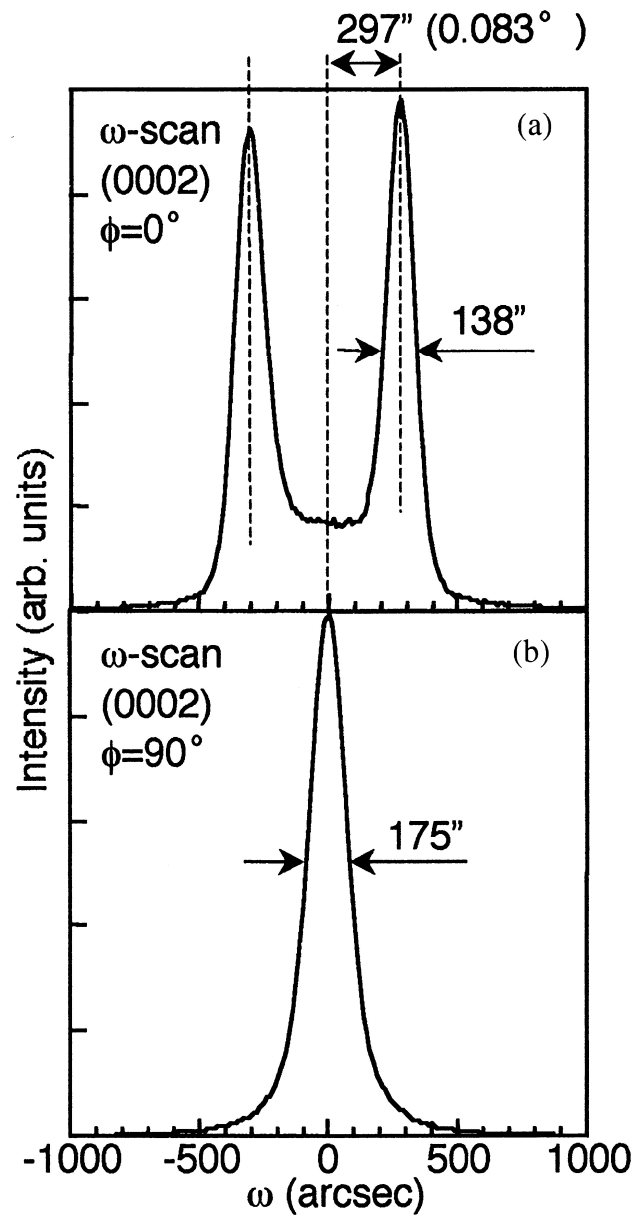
Fig. 3.26. Double-crystal X-ray rocking curves of the GaN (0002) peak for (a) $\phi = 0°$ (incident X-ray perpendicular to ridge-stripe) and (b) $\phi = 90°$ (parallel), where the azimuth ϕ is the angle between the stripe direction and the rotation axis in ω-scan.
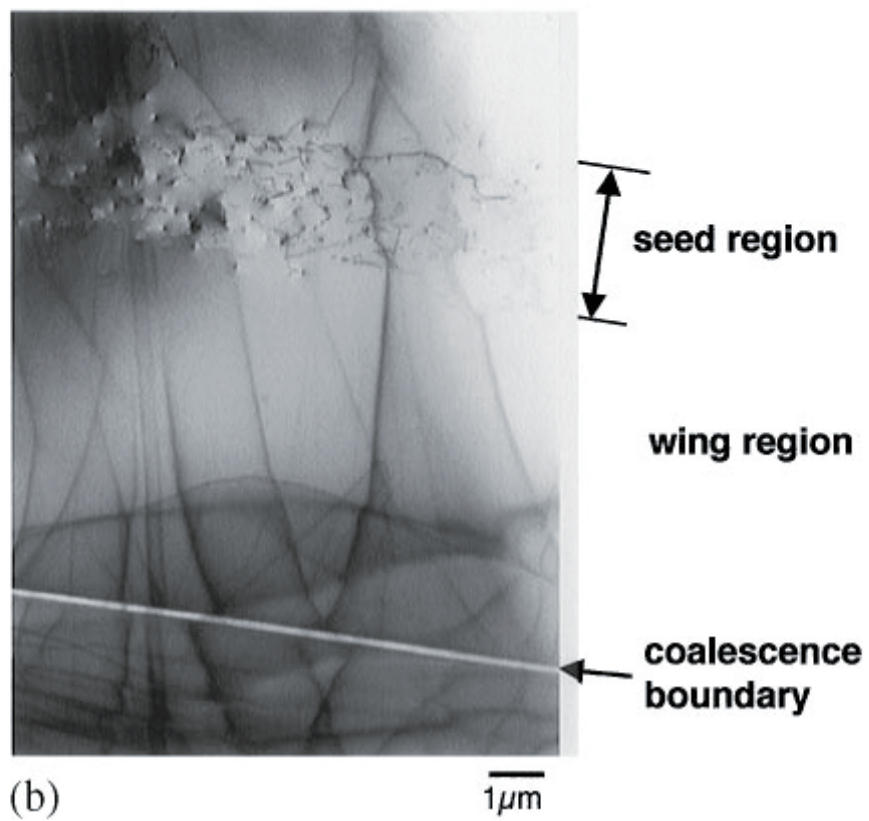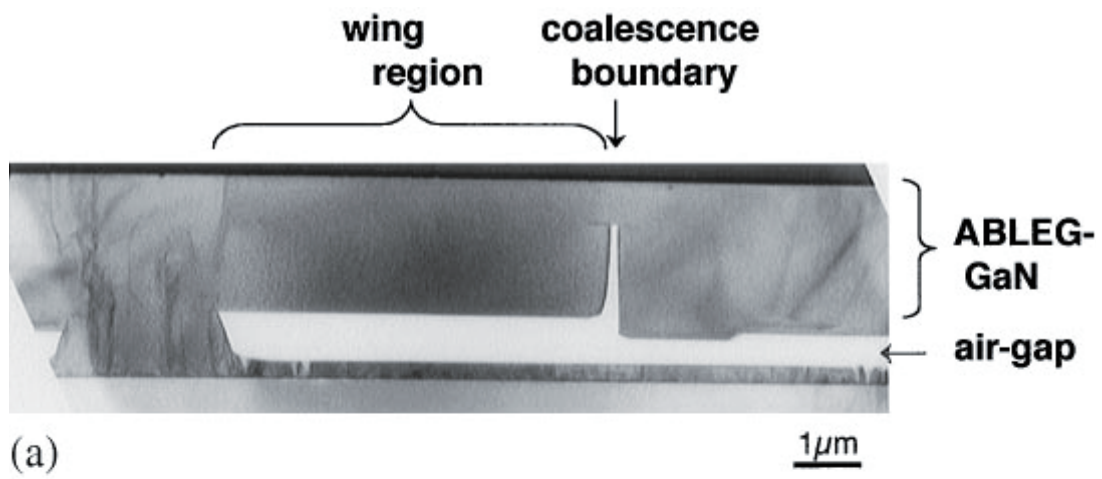
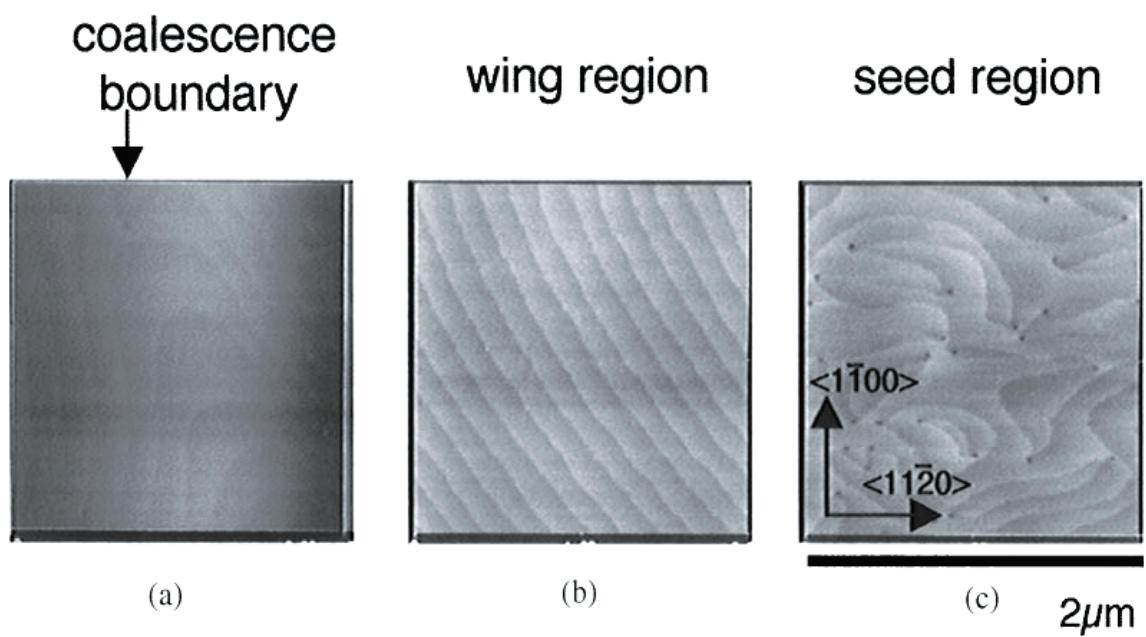Fig. 3.27. (a) Cross-sectional and (b) plan-view TEM images of ABLEG-GaN.

Fig. 3.28. AFM images of (a) the vicinity of coalescence boundary, (b) the middle of wing

region, and (c) the seed region.

respectively.

Figure 3.28 shows the AFM images of (a) the vicinity of coalescence boundary, (b) the middle of wing region and (c) the seed region. The large pits terminating the steps were observed in the seed region. These pits are due to the screw component of the threading dislocations [18]. However, no pits were observed in the wing region and near the coalescence boundary. The wing region of the ABLEG-GaN had typical stepped and terraced structure. The step height was about 0.255 nm, which corresponds to one monolayer of (0001) GaN ($c/2 =$ 0.259 nm). The value of root mean square roughness was found to be 0.089 nm in the wing region. At the coalescence boundary, the smooth and continuous surfaces were obtained. The reason why the coalescence boundary possesses smooth surface is probably due to low wing tilt mentioned above.

Conclusion

High-quality coalescent GaN thin films with low dislocation density as well as low wing tilt were successfully demonstrated by a promising technique of lateral epitaxial growth, namely ABLEG. The densities of the vertical dislocations were about $9 \times 10^8 \, \text{cm}^{-2}$ in the seed region, while below $1 \times 10^6 \, \text{cm}^{-2}$ in other regions. The densities of the horizontal dislocations were about $1 \times 10^6 \, \text{cm}^{-2}$ in the wing region, $4 \times 10^7 \, \text{cm}^{-2}$ in the vicinity of the coalescence boundary, respectively. The XRD measurements indicated that the tilt angle of c-axis relative to the underlying seed GaN was about 297 arcsec (0.083°), and the FWHM of the XRD curve for the wing region was 138 arcsec. Both the wing region and coalescence boundary have atomically smooth surfaces. It was considered that the low wing tilt, high uniformity of the c-axis orientation and no bending of the threading dislocations are due to removal of the strain between the laterally grown GaN and the mask material. More suppression of wing tilt will result in the more reduction of dislocation density.

References in 3.2.1

[1] A. Usui, H. Sunakawa, A. Sakai, and A. A. Yamaguchi, *Jpn. J. Appl. Phys.* **36**, L899 (1997).

[2] A. Sakai, H. Sunakawa, and A. Usui, *Appl. Phys. Lett.* **71**, 2259 (1997).

[3] H. Marchand, X. H. Wu, J. P. Ibbetson, P. Fini, P. Kozodoy, S. Keller, J. S. Speck, S. P.

DenBaars, and U. K. Mishra, *Appl. Phys. Lett.* **73**, 747 (1998).

[4] H. Marchand, J. P. Ibbetson, P. Fini, S. Chichibu, S. J. Rosner, S. Keller, S. P. DenBaars, J. S. Speck, and U. K. Mishra, *Proc. 25th International Symp. Compound Semicond.* (1998) p. 681.

[5] P. Fini, L. Zhao, B. Moran, M. Hansen, H. Marchand, J. P. Ibbetson, S. P. DenBaars, U. K. Mishra, and J. S. Speck, *Appl. Phys. Lett.* **75**, 1706 (1999).

[6] T. S. Zheleva, O. H. Nam, M. D. Bremser, and R. F. Davis, *Appl. Phys. Lett.* **71**, 2472 (1997).

[7] O. H. Nam, T. S. Zheleva, M. D. Bremser, and R. F. Davis, *Appl. Phys. Lett.* **71**, 2638 (1997).

[8] K. J. Linthicum, T. Gehrke, D. B. Thomson, E. P. Carlson, P. Rajagopal, T. P. Smith, A. D. Batchelor, and R. F. Davis, *Appl. Phys. Lett.* **75**, 196 (1999).

[9] T. S. Zheleva, S. A. Smith, D. B. Thomson, T. Gehrke, K. J. Linthicum, P. Rajagopal, E. P. Carlson, W. M. Ashmawi, and R. F. Davis, *MRS Internet J. Nitride Semicond. Res.* **4S1**, G3.38 (1999).

[10] K. J. Linthicum, T. Gehrke, D. B. Thomson, M. K. Tracy, E. P. Carlson, T. P. Smith, T. S. Zheleva, C. A. Zorman, M. Mehregany, and R. F. Davis, *MRS Internet J. Nitride Semicond. Res.* **4S1**, G4.9 (1999).

[11] H. Marchand, N. Zhang, L. Zhao, Y. Golan, S. J. Rosner, G. Girolami, P. Fini, J. Ibbetson, S. Keller, S. P. DenBaars, J. S. Speck, and U. K. Mishra, *MRS Internet J. Nitride Semicond. Res.* **4**, 2 (1999).

[12] S. Nakamura, M. Senoh, S. Nagahama, N. Iwasa, T. Matsushita, and T. Mukai, *MRS Internet J. Nitride Semicond. Res.* **4S1**, G1.1 (1999).

[13] H. Sone, S. Nambu, Y. Kawaguchi, M. Yamaguchi, H. Miyake, K. Hiramatsu, Y. Iyechika, T. Maeda, and N. Sawaki, *Jpn. J. Appl. Phys.* **38**, L356 (1999).

[14] K. Tadamoto, Y. Ohuchi, H. Okagawa, H. Itoh, H. Miyake, and K. Hiramatsu, *MRS Internet J. Nitride Semicond. Res.* **4S1**, G3.1 (1999).

[15] A. Sakai, H. Sunakawa, and A. Usui, *Appl. Phys. Lett.* **73**, 481 (1998).

[16] I. Kim, C. Sone, O. Nam, Y. Park, and T. Kim, *Appl. Phys. Lett.* **75**, 4109 (1999).

[17] K. Kobayashi, A. Yamaguchi, S. Kimura, H. Sunakawa, A. Kimura, and A. Usui, *Jpn. J. Appl. Phys.* **38**, L611 (1999).

[18] D. Kapolnek, X. Wu, B. Heying, S. Keller, B. P. Keller, U. K. Mishra, S. P. DenBaars, and J. S. Speck, *Appl. Phys. Lett.* **67**, 1541 (1995).

[19] P. Fini, H. Marchand, J. P. Ibbetson, B. Moran, L. Zhao, S. P. DenBaars, J. P. Speck, and U. K. Mishra, *Mater. Res. Soc. Symp. Proc.* **572**, 315 (1999).

3.2.2. Recombination dynamics in GaN and InGaN/GaN MQW on air-bridged lateral epitaxial grown GaN layers

Introduction

Currently, the growth technique of GaN-based semiconductors has been developed rapidly for the fabrication of light-emitting devices and robust electron devices. Actually, a lateral epitaxial overgrowth (LEO) method and a pendeo-epitaxy method have been carried out with the aim of achieving good crystallinity of GaN or InGaN with low threading dislocation density (TDD). More recently, Kidoguchi *et al.* [1] accomplished a new crystal growth technique which is called air-bridged lateral epitaxial growth (ABLEG).

As for the correlation between threading dislocation and recombination pathway, Sugahara *et al.* [2] showed by the comparison between transmission electron microscopy (TEM) and cathodoluminescence mapping that dislocations act as nonradiative recombination centers (NRC). On the other hand, Mukai *et al.* [3] reported that the efficiency of blue light-emitting diode (LED), whose defect density is lowered by the LEO technique, is almost the same as that of conventional LEDs grown directly on sapphire. It was also reported that the lifetime of photoluminescence (PL) depended strongly on TDD in LEO-GaN by selective-photoexcitation using a metal-masking technique [4] and by site-selective time-resolved PL (TRPL) spectroscopy with a spatial resolution of less than a few microns [5]. Furthermore, Nakamura reported that the difference in the emission efficiency between LEDs grown on sapphire and LEO-GaN substrates becomes smaller with increasing In mole fraction in InGaN [6]. Therefore, it is of great significance to assess the detailed recombination dynamics in InGaN with different In mole fractions and different TDDs.

In this section, recombination dynamics in GaN and InGaN/GaN multiple quantum well (MQW) layers grown by the ABLEG technique has been studied by using TRPL spectroscopy with a spatial resolution of less than 1 μm.

Experimental

Two types of samples were grown by MOVPE using the ABLEG technique [1]. One is ABLEG-GaN [sample (a)] which consists of two regions, one is the seed region having high
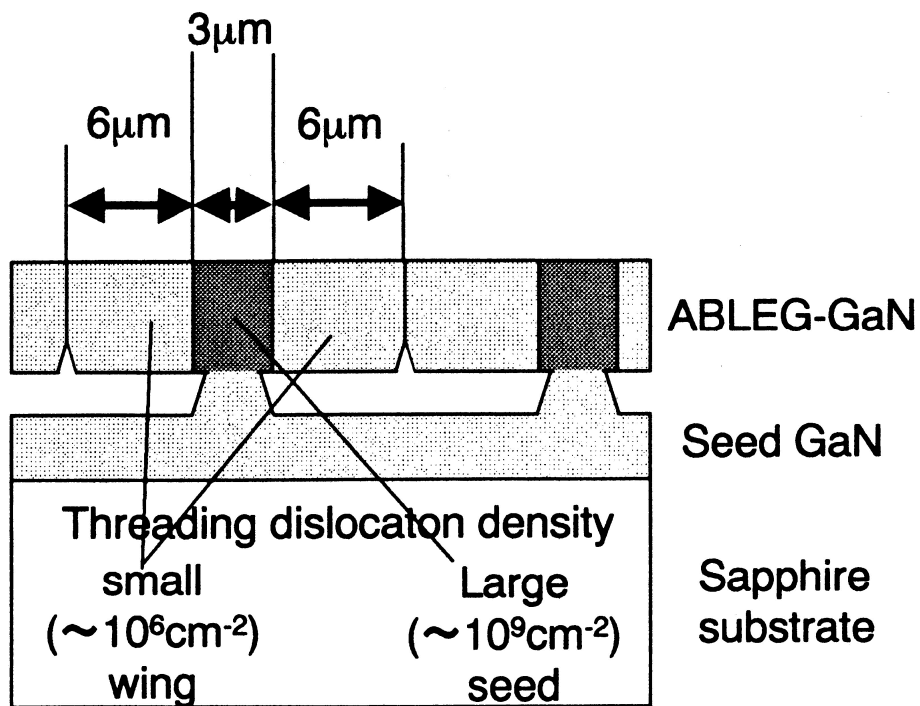
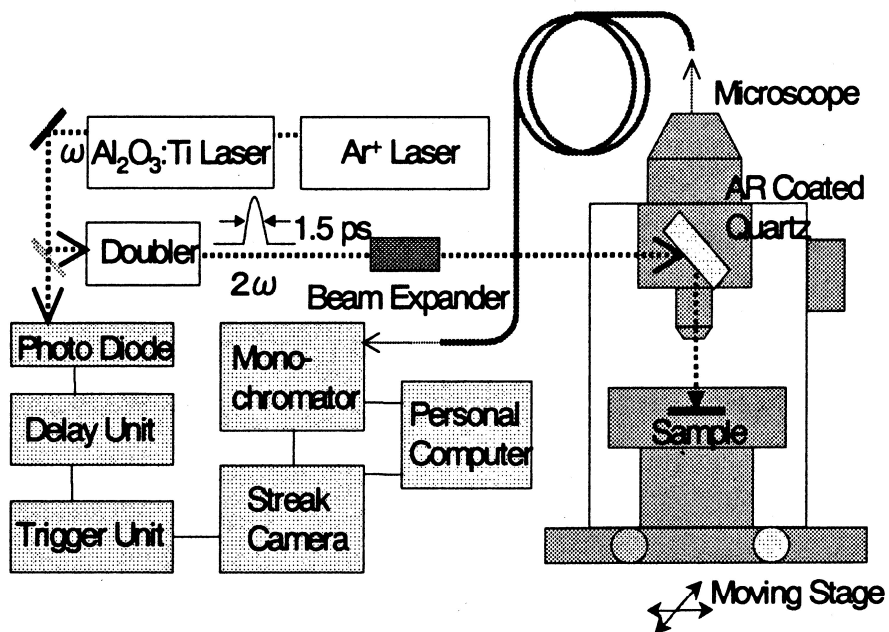Fig. 3.29. Schematic cross sectional structure of ABLEG-GaN (sample (a)).

Fig. 3.30. Time-resolved PL measurement system in conjunction with UV-optical microscope.

TDD (10^9 cm^{-2}) and another is the wing region having low TDD (10^6 cm^{-2}), schematically depicted in Fig. 3.29. Another sample is InGaN (3.5 nm)/GaN (10.5 nm) triple quantum well [sample (b)] which is grown on the ABLEG-GaN.

For PL and TRPL measurements, the pulsed excitation source was second or third harmonic generation (SHG or THG) of a mode-locked Al$_2$O$_3$:Ti laser which was pumped by Ar$^+$ laser. The pulse width and the repetition rate were 1.5 ps and 80.0 MHz, respectively. The excitation wavelength was selected as 266 nm (THG) or 353 nm (SHG) for sample (a) and 370 nm (SHG) for sample (b) in order to excite only InGaN QW layers. Photoluminescence detection was carried out using a multi-channel analyzer and TRPL detection system was composed of a streak camera in conjunction with a 25 cm monochromator. In order to avoid the multi-excitation for sample (b), repetition rate of the source (80.0 MHz) was selected to 4.0 MHz by the acoustic-optic modulator. Figure 3.30 shows the TRPL measurement system whose spatial resolution of less than 1 µm has been achieved by using air-gapped objective lens.

Results and discussion

Figure 3.31 shows PL spectra of two samples at room temperature (RT). The PL main peak of sample (a) is located at 3.41 eV. The PL spectrum of sample (b) is oscillated owing to the effect of thin layer interference.

Therefore, the real PL main peak energy without this effect would be between the energies of two peaks (2.918 and 2.962 eV) suiting to 2.940 eV. From this PL peak energy, we calculated the In mole fraction of InGaN QW layers of sample (b) using following equation:

$$E_{InGaN} = E_{GaN}(1-X) + E_{InN}X - bX(1-X), \tag{3.3}$$

where X is the In mole fraction and E_{InGaN}, E_{GaN} and E_{InN} are the bandgap of InGaN, GaN and InN, respectively. And b is the bowing parameter. Furthermore, we considered the effect of blue shift due to quantum confinement, as well as the effect of the red shift due to the piezo-electric field in the QW layers. Using the reported value of $b = 2.0$ eV the In mole fraction of sample (b) was estimated to be 17%.

Figure 3.32 shows PL decay spectra of ABLEG-GaN [sample (a)] monitored at A free exciton (E_{XA}) from a seed region (TDD = 10^9 cm^{-2}) (a) and a wing region (TDD = 10^6 cm^{-2}) (b) at RT. Both decay spectra showed double exponential curves. Both first component (τ_1) and
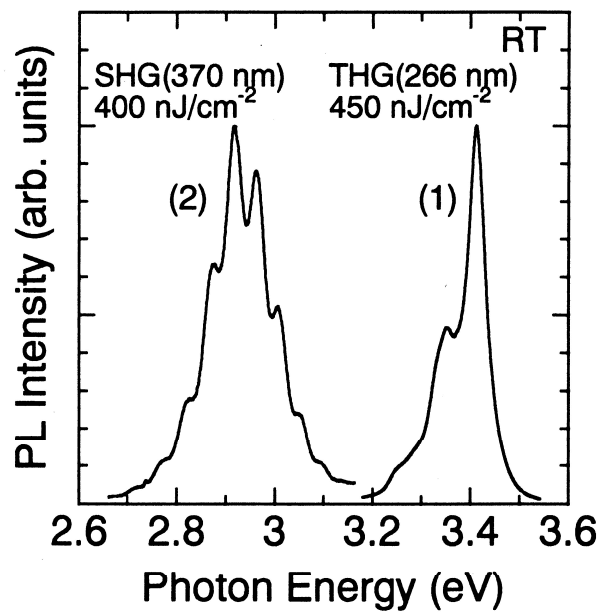
130

Fig. 3.31. Photoluminescence spectra of (1) sample (a) and (2) sample (b) at RT. The excitation source was THG (266 nm) for sample (a) and SHG (370 nm) for sample (b).
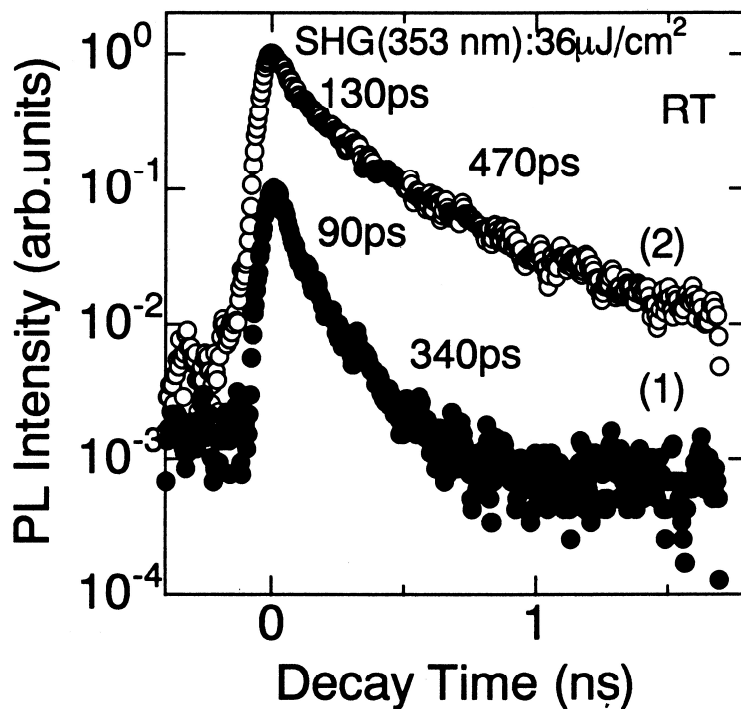

Fig. 3.32. Photoluminescence decay spectra of sample (a) (1) at a seed region (TDD = 10^9 cm^{-2}) and (2) at a wing region (TDD = 10^6 cm^{-2}).

second component (τ_2) are limited by the channel of nonradiative recombination [5]. Therefore, we discuss how τ_1 value changes with regions in a sample because the fast process limits the PL decay process compared with the slow one. It was found that PL lifetime (τ_{PL}) measured at a wing region is 130 ps which is larger than the value monitored at a seed region (90 ps) whose TDD is three orders of magnitude larger than that in the wing region. This indicates that the larger TDD makes τ_{PL} shorter, but τ_{PL} did not differ so largely between two regions having the TDD difference of three orders of magnitude, as suggested previously [5]. It is noted that the double exponential behavior in PL decay is changed to single exponential one as a result of the elimination of the first component (τ_1) if a small amount of In (less than a few % in mole fraction) is added to the layer.

Figure 3.33 shows PL decay spectra of sample (b) at RT. It was found that τ_{PL} values measured at a wing region and at a seed region were 1.74 ns and 1.60 ns, respectively. The tendency that the larger TDD makes τ_{PL} shorter is similar to the result for sample (a). Therefore, threading dislocation affects emission efficiency in InGaN as well as in GaN. Figure 3.34 shows the fluorescence micro-image of sample (b) through the 420 nm band pass filter. In fact, the intensity of blue emission in the wing region is more intense than that in the window region. Comparing the ratio of the difference between τ_{PL} at the wing and the seed regions, however, the values for sample (a) and (b) are 40% and 8%, respectively. Considering that internal quantum efficiencies of luminescence measured in macroscopic photo-excitation were 2% and 9% for ABLEG-GaN and ABLEG-InGaN/GaN MQW at RT, threading dislocation is not major NRC at RT and this tendency is more clearly in sample (b) than in sample (a).

These phenomena can be understood in terms of the model of carrier localization depicted in Fig. 3.35. The potential fluctuation in GaN is so small that carriers can diffuse easily, so that the carriers are captured at NRC and recombine nonradiatively. On the other hand, in InGaN QW layers the potential fluctuation is too large for carriers to diffuse over the potential barriers. Therefore, it is difficult for carriers to be captured at NRC caused by threading dislocations. The origin of localization in InGaN QW layers is considered to be the fluctuation of well width and In mole fraction. The effect of potential fluctuation on the recombination pathway seems to be generally applied independent on the growth technology because the results obtained at ABLEG samples do not conflict with those at LEO samples [4,5].
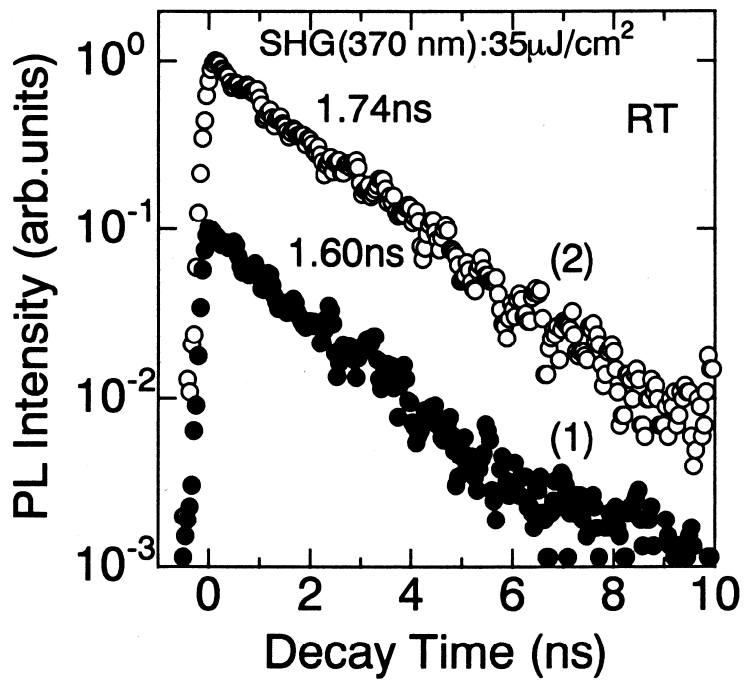
Fig. 3.33. Photoluminescence decay spectra of sample (b) (1) at a seed region (TDD = 10^9 cm^{-2}) and (2) at a wing region (TDD = 10^6 cm^{-2}).
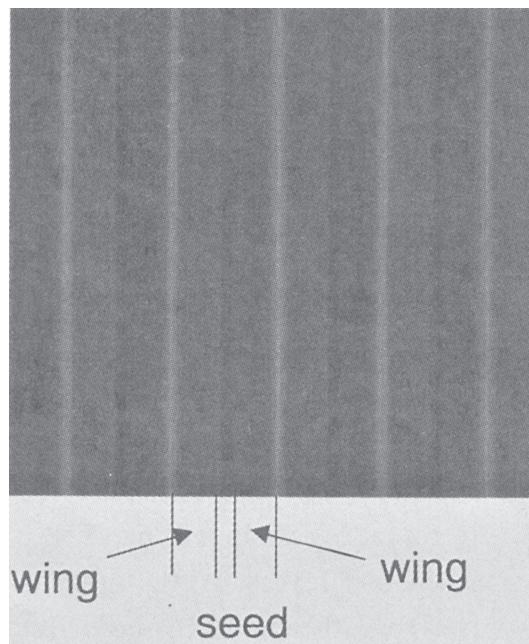

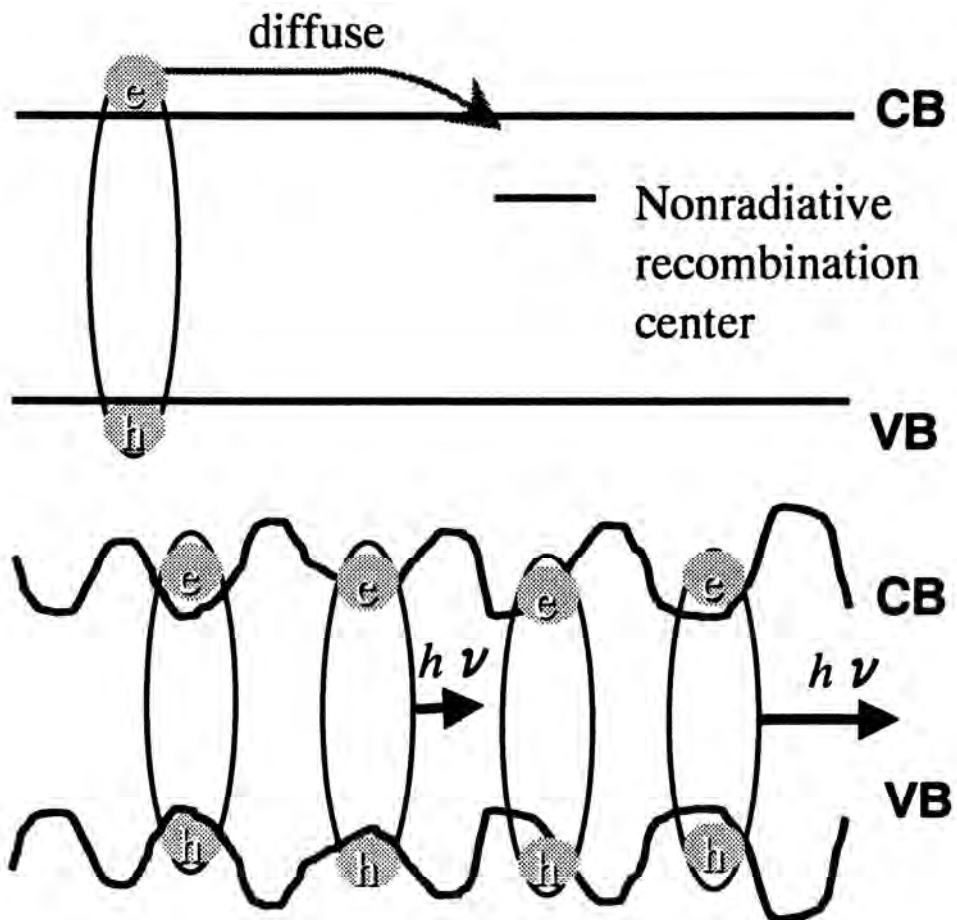Fig. 3.34. Fluorescence micro-image of sample (b).

Fig. 3.35. Model of the carrier (a) in GaN and (b) in InGaN QW layers. (a) In GaN, the potential fluctuation is so small that carriers can diffuse easily, so that the carriers are captured at nonradiative recombination centers. (b) In InGaN QW layers, the potential fluctuation is too large for carriers to diffuse over the potential barriers, therefore it is difficult for carriers to be captured at nonradiative recombination centers.

Conclusion

Recombination dynamics in GaN and InGaN/GaN MQW fabricated by ABLEG technique was studied by employing spatial and time-resolved PL spectroscopy. The spatial resolution of less than 1 µm was achieved by using air-gapped objective lens. It was found that threading dislocations are not major NRC in either ABLEG-GaN or InGaN/GaN MQW on ABLEG-GaN at room temperature. However, comparing the ratio of the difference between PL lifetime at the wing and the seed regions in ABLEG-InGaN/GaN MQW (8%) and ABLEG-GaN (40%) indicated that threading dislocations affected less carrier recombination process in InGaN MQW than in GaN. Furthermore, it was found that these phenomena could be understood in terms of the model of carrier localization in InGaN QW layers. It was also found that the effect of potential fluctuation on the recombination pathway found in the LEO-grown samples could be also applied to the layers grown by the ABLEG technique.

References in 3.2.2

[1] I. Kidoguchi, A. Ishibashi, G. Sugahara, A Tsujimura, and Y. Ban, *Jpn. J. Appl. Phys.* **39**, L453 (2000).

[2] T. Sugahara, H. Sato, M. Hao, Y. Naoi, S. Kurai, S. Tottori, K. Yamashita, K. Nishino, L. Romano, and S. Sakai, *Jpn. J. Appl. Phys.* **37**, L398 (1998).

[3] T. Mukai, K. Takekawa, and S. Nakamura, *Jpn. J. Appl. Phys.* **37**, L839 (1998).

[4] S. Chichibu, T. Azuhata, T. Sota, and S. Nakamura, *Appl. Phys. Lett.* **74**, 1460 (1999).

[5] T. Izumi, Y. Narukawa, K. Okamoto, Y. Kawakami, Sg. Fujita, and S. Nakamura, *J. Lumin.* **87-89**, 1196 (2000).

[6] S. Nakamura, *JSAP International* **1**, 5 (2000).

3.2.3. Nonradiative recombination processes of carriers in InGaN/GaN probed by the microscopic transient lens spectroscopy

Introduction

GaN-based optical devices such as light-emitting diodes and laser diodes have very strong emissions in spite of high threading dislocation density (TDD) of 10^8-10^{10} cm^{-2} [1]. For a wider application of GaN-based optical devices, the development of the emission efficiency has been expected. A nonradiative recombination (NR) process of carrier in a material is one of the most important processes to control the optical property because a great numbers of carriers decay by the NR process at room temperature. It had been reported that the threading dislocation (TD) in GaN might act as the nonradiative recombination centers (NRC) [2]. In order to reduce the TDD in GaN and InGaN, the growth technique has been developed rapidly. Recently, low dislocated GaN (TDD = 10^6 cm^{-2}) have been achieved by using the lateral epitaxial overgrowth (LEO) technique [3]. However, remarkable enhancement of emission efficiencies of low dislocated GaN and InGaN has so far not been found [3–6]. The actual correlation between the NR process and the TDD is still unknown because the direct observation of the NR process has been very difficult. Recently, Okamoto *et al.* succeeded in the direct detection of the heat generation of the NR process probed by the transient grating (TG) technique [7,8]. In this section, NR processes of carriers in GaN and InGaN/GaN QW have been studied by the selective time-resolved measurement of the heat generation and conduction probed by newly developed microscopic transient lens (MTL) spectroscopy.

Experimental procedure

A frequency-tripled beam of a Nd:YAG laser (355 nm) and a He-Ne laser (633 nm) were used as a pump and a probe beam, respectively, as shown in Fig. 3.36. Both beams were focused at a sample by an objective lens ($\times$100). Spot sizes of both beams were about 3 µm in diameter. By the excitation with a Gaussian spatially distributed pump beam, refractive index n in the sample is also spatially modulated by the modulation of the carrier density change δN and the temperature change δT. Such modulations act as transient lenses. Focus and defocus of the probe beam at the transient lens was detected by a photomultiplier tube with an optical fiber. All
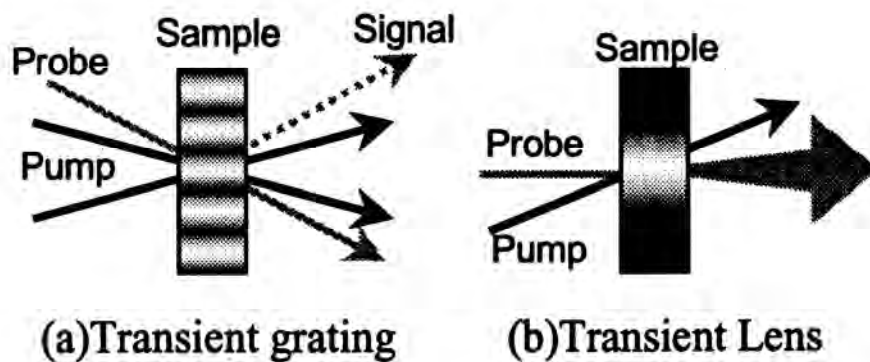
Fig. 3.36. Optical arrangement of pump beam, probe beam and signal for (a) transient grating

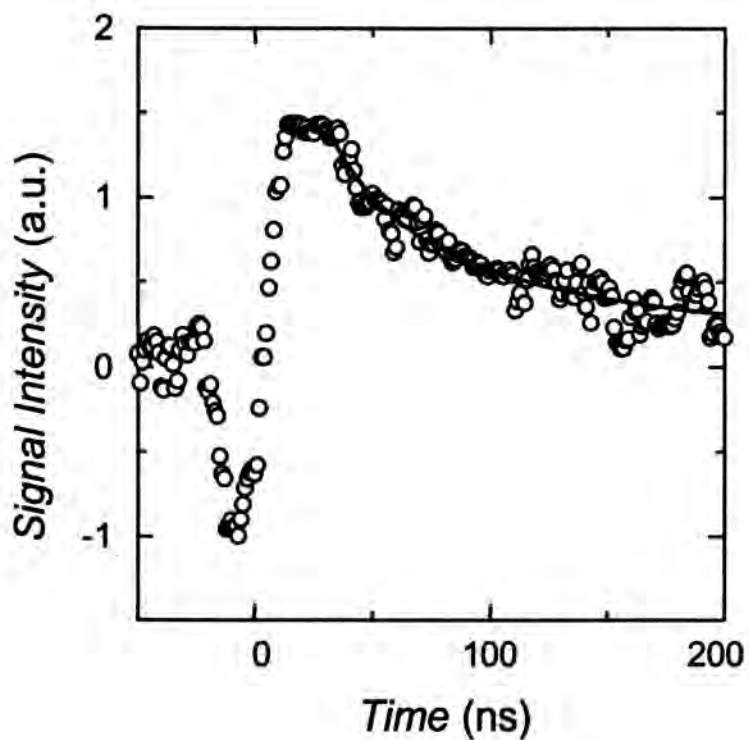spectroscopy and (b) transient lens spectroscopy.

Fig. 3.37. Time profile of the microscopic transient lens spectroscopy taken for bulk GaN.

Curved line is the fitting line by Eq. (3.5).

measurements were carried out at room temperature (23°C).

The samples used in this study were grown by MOVPE. Recently, Kidoguchi *et al.* accomplished air-bridged lateral epitaxial growth (ABLEG) [9]. ABLEG-GaN has two regions, one is a seed region having high TDD (1-2 × 10^9 cm^{-2}) and another is a wing region having low TDD (1-2 × 10^6 cm^{-2}). The sample structure of ABLEG-GaN was shown in Fig. 3.29. Three samples were prepared; bulk GaN, ABLEG-GaN and InGaN (3.5 nm)/GaN (10.5 nm) triple quantum well (3QW) structure grown on ABLEG-GaN.

Results and discussion

The time profile of the MTL signal taken for the bulk GaN was shown in Fig. 3.37. This signal has two components; the spike-like dip component just after photoexcitation and the slow decay component. The fast component and the slow component are due to the defocus and focus of the probe beam at the transient concave and convex lens effects in the sample, respectively. From $\partial n/\partial N > 0$ and $\partial n/\partial T < 0$, we assigned the fast and slow components to the modulations of the carrier density and the temperature, respectively. The signal intensity and decay of the fast component represents the created carrier density and the carrier recombination/diffusion, respectively. The signal intensity and decay of the slow component represent the amount of the generated heat by the NR process and the thermal conductivity of materials, respectively. Time and spatial dynamics of δn and δT can be described by the rate equation including the diffusion/recombination of carriers and the generation/conduction of heat with cylindrical coordinates. By solving this rate equation, time and spatial dependence of δT can be written by

$$\delta T(r,t) = \frac{\tau_{\text{rad}}}{\tau_{\text{rad}} + \tau_{\text{nonrad}}} \frac{QN_0}{\rho C_{\text{p}}} \left\{ -\exp\left[-\frac{r^2}{w_0^2} \left(\frac{1}{\tau_{\text{rad}}} + \frac{1}{\tau_{\text{nonrad}}} \right) t \right] \right.$$

$$\left. + \frac{w_0^2}{4D_{\text{th}}t + w_0^2} \exp\left(-\frac{r^2}{4D_{\text{th}}t + w_0^2} \right) \right\}, \tag{3.4}$$

where w_0 and r are the pump beam width and the distance from the beam center, respectively. N_0 is the initial density of carriers just after the excitation ($t = 0$). D and D_{th} are the diffusion coefficient of carriers and heat in GaN, respectively. Thermal conductivity κ of GaN can be
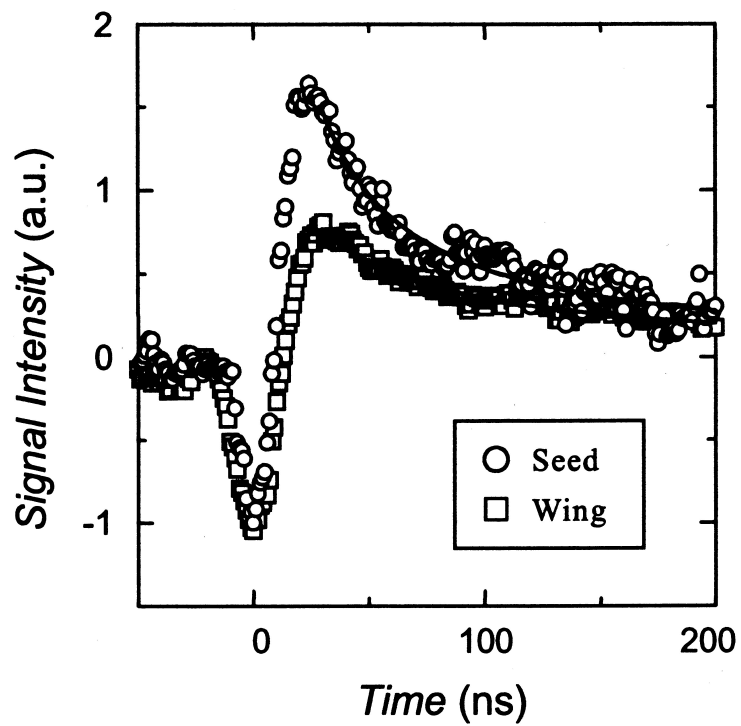
Fig. 3.38. Time profiles of the suite selective microscopic transient lens spectroscopy taken for ABLEG-GaN at the seed region (open circles) and the wing region (open squares). Curved lines are the fitting lines by Eq. (3.5).

obtained by $\kappa = D_{th}\rho C_p$ with the density ($\rho = 6.095$ gcm^{-3}) and the heat capacity ($C_p = 9.745$ cal/molK). τ_{rad} and τ_{nonrad} are the radiative and nonradiative recombination lifetime, respectively. Q is the heat amount generated by the NR process. The optical pass of the probe beam at the transient lens is given by the ABCD law of Gaussian beam. In this experimental condition, the time profile of the signal intensity of MTL [$S(t)$] is proportional to δT ($t, r = 0$). Therefore, the decay component of the thermal signal can be described as

$$S(t) = \frac{I(t) - I(0)}{I(0)} \propto \frac{w_0^2}{4D_{th}t + w_0^2}. \tag{3.5}$$

We could fit the slow decay component of Fig. 3.37 by using this equation and a value for D_{th}/w_0^2 was obtained. To obtain a value of D_{th}, a value of w_0^2 is needed. The value of w_0 was estimated to be 2.6 µm by using the D_{th} value for this sample obtained by the TG measurement [$D_{th} = 0.77$ cm^2/s ($\kappa = 2.3$ W/cmK)] [10]. We can use this w_0 value for the measurement of ABLEG-GaN. The time profiles of the selective MTL signals at the seed and the wing regions in ABLEG-GaN were shown in Fig. 3.38. These decays were fitted by using Eq. (3.5) and the D_{th} values were obtained at each region. The calculated κ obtained from D_{th} were $\kappa = 2.2$ W/cmK at the seed region and $\kappa = 2.0$ W/cmK at the wing region. The obtained values of each region were not so different and close to $\kappa = 2.3$ W/cmK of bulk GaN. The value of κ of GaN had been measured as 1.3 W/cmK by Sichel and Pankove in 1977 [11]. Recently, Luo *et al.* reported that κ of GaN grown by the LEO with TDD = 5×10^6 cm^{-2} is 1.55 W/cmK though κ of GaN with TDD = 10^{10} cm^{-2} is 1.35 W/cmK as probed by the scanning thermal microscope (STM) [12]. In a similar way, Asnin *et al.* reported κ of GaN-LEO with TDD > 10^5 cm^{-2} as 1.7-1.8 W/cmK [13]. Florescu *et al.* reported that the κ values of GaN depend on the carrier concentration and thickness between 0.5 and 1.95 W/cmK [14]. They also developed the STM with spatial resolutions and reported that the κ values of GaN is 2.00 W/cmK $< \kappa <$ 2.10 W/cmK on the partially overgrown regions [15]. Obtained κ values of bulk GaN and ABLEG-GaN in this study are close to the maximum value which has ever been measured. This fact suggests both bulk GaN and ABLEG-GaN should have the highest crystallinity.

Although the difference of the κ values was small between the seed region and the wing region, a remarkable difference of the thermal signal intensity was found at each region. We could compare the thermal signal intensities by the NR processes of unit carrier density at each
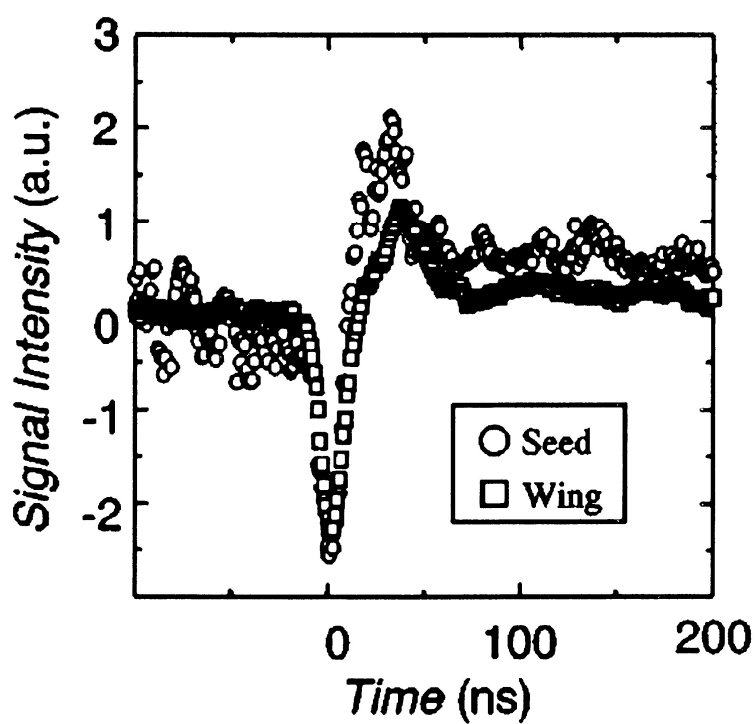
Fig. 3.39. Time profiles of the suite selective microscopic transient lens spectroscopy taken for InGaN/GaN 3QW grown on ABLEG-GaN at the seed region (open circles) and the wing region (open squares).

region by normalization of the carrier signal intensities. It was found that the heat generation at the wing region was much smaller than that at the seed region. At the wing region, low TDD should reduce the NR processes of carriers. A similar result was obtained for the InGaN/GaN 3QW structure grown on ABLEG-GaN as shown in Fig. 3.39. These facts suggest that the TD in GaN and InGaN QW must act as the NRC.

Detecting the heat generation from the TD and clarifying the relationship between the NR process and TD in GaN and InGaN QW have been succeeded for the first time by the selective observation of the thermal signals. However, one question has remained: Why were optical properties at each region not different in spite of the three-order difference of TDD? From the measurement of photoluminescence spectra, the emissions of these samples are dominantly attributed to free excitons and the internal efficiency of emission of each region is 0.6% at room temperature [10]. This fact means that the 99.4% of free excitons contribute to the heat generation. If internal emission efficiencies are decided only by the ratio between the radiative and nonradiative recombination processes of excitons, emission efficiency should be dramatically different at each region. It is considered that the NR processes of excitons should not be a dominant path way of the thermalization in GaN and InGaN QW. Another process must be the dominant thermalization path way, for example, slow thermalization processes after the thermal dissociation of excitons to electrons and holes, or trapping into the deep energy level in the crystals. This is the possible reason that TD is not effective for the emission efficiency of GaN and InGaN/GaN QW though it acts as the NRC.

Conclusion

Microscopic transient lens spectroscopy is a powerful tool for the time and spatially resolved detection of the NR processes of carriers in GaN and InGaN/GaN QW. It was found that the TD in GaN actually acts as the NRC of created free excitons. However, TD should not be effective for the emission efficiency because another slow thermalization processes due to the thermal dissociation or the trapping in the deep level of excitons should be the dominant process for thermalization in GaN and InGaN/GaN QW.

References in 3.2.3

[1] For example, in *Introduction to Nitride Semiconductor Blue Laser and Light Emitting Diode*, edited by S. Nakamura and S. F. Chichibu (Taylor and Francis, London, 2000).

[2] T. Sugahara, M. Hao, T. Wang, D. Nakagawa, Y. Naoi, K. Nishino, and S. Sakai, *Jpn. J. Appl. Phys.* **37**, L1195 (1998).

[3] T. Mukai, K. Takekawa, and S. Nakamura, *Jpn. J. Appl. Phys.* **37**, L839 (1998).

[4] S. Chichibu, T. Azuhata, T. Sota, and S. Nakamura, *Appl. Phys. Lett.* **74**, 1460 (1999).

[5] T. Izumi, Y. Narukawa, K. Okamoto, Y. Kawakami, Sg. Fujita, and S. Nakamura, *J. Lumin.* **87-89**, 1196 (2000).

[6] T. Izumi, K. Inoue, Y. Narukawa, K. Okamoto, Y. Kawakami, Sg. Fujita, A. Tsujimura, I. Kidoguchi, and Y. Ban, *IPAP Conf. Series* **1**, 599 (2000).

[7] K. Okamoto, A. Kaneta, K. Inoue, Y. Kawakami, M. Terazima, T. Mukai, G. Shinomiya, and Sg. Fujita, *Phys. Status Solidi B* **228**, 81 (2001).

[8] K. Okamoto, Y. Kawakami, Sg. Fujita, and M. Terazima, *Anal. Sci.* **17**, s312 (2001).

[9] I. Kidoguchi, A. Ishibashi, G. Sugahara, A. Tsujimura, and Y. Ban, *Jpn. J. Appl. Phys.* **39**, L453 (2000).

[10] K. Inoue, K. Okamoto, Y. Kawakami, Sg. Fujita, M. Terazima, A. Tsujimura, and I. Kidoguchi (unpublished).

[11] E. K. Sichel and J. I. Pankove, *J. Phys. Chem. Solids* **38**, 330 (1977).

[12] C.-Y. Luo, H. Marchand, D. R. Clarke, and S. P. DenBaars, *Appl. Phys. Lett.* **75**, 4151 (1999).

[13] V. M. Asnin, F. H. Pollak, J. Ramer, M. Schurman, and I. Ferguson, *Appl. Phys. Lett.* **75**, 1240 (1999).

[14] D. I. Florescu, V. M. Asnin, F. H. Pollak, R. J. Molnar, and C. E. C. Wood, *J. Appl. Phys.* **88**, 3295 (2000).

[15] D. I. Florescu, V. M. Asnin, F. H. Pollak, A. M. Jones, J. C. Ramer, M. J. Schurman, and I. Ferguson, *Appl. Phys. Lett.* **77**, 1464 (2000).

Concluding Remarks

Impact of the present dissertation is the developments of novel epitaxial growth methods to fabricate wide bandgap laser diodes (LDs) such as compound source molecular beam epitaxy (CSMBE) for ZnMgSSe quaternary alloy and air-bridged lateral epitaxial growth (ABLEG) of GaN free-standing substrate with low dislocation density as well as low tilt of c-axis orientation. Contribution of the ABLEG technology to commercially available III-nitride LDs and guiding principles to solve the remaining issues on II-VI and III-nitride green LDs are described as follows.

The threading dislocation density and the tilt angle of ABLEG-GaN substrate are $1 \times 10^6 \, \mathrm{cm}^{-2}$ and less than 0.1°, respectively, in the wing region. The tilt angle is relatively small compared with other lateral epitaxial overgrown GaN because the air-gap between the wing and the mask material is effective in making the ABLEG-GaN free from the strain. ABLEG-GaN substrates contributed to improve the operation lifetime of InGaN-based violet LDs. The lifetime of LDs on ABLEG-GaN substrates was 10-30 times longer than the identical structure LDs on sapphire substrates under a constant output power of 30 mW continuous-wave (CW) operation. The lifetime of LDs on ABLEG-GaN substrates exceeded 1000 h under 30 mW CW operation at 25°C, until bulk GaN substrates grown by hydride vapor phase epitaxy with extremely low dislocation density [1] had been available to fabricate LDs on them. InGaN-based LDs in the violet-to-blue region are nearing maturity with high output powers and long lifetimes, leading to commercialization for Blu-ray Discs and laser projectors.

Recently, green LDs have been attracting much attention for their potential application as light sources in full-color display devices installed in consumer products such as pocket-sized pico-projectors. Blue LDs and red LDs are commercially available; however, only second harmonic generation (SHG) lasers have been practically used as green source. Direct emission green LDs are expected to achieve practical application because of their lower form factor, higher efficiency and lower cost than that of SHG lasers. Green LDs emitting over 500 nm have been reported with InGaN-based material system [2-4] as well as violet and blue LDs. However, as the lasing wavelength becomes longer to the pure green region, the threshold current density increases especially in the wavelength range over 530 nm. Higher In content of InGaN quantum

wells (QWs) strengthens the internal electric fields due to piezoelectric polarization and makes homogeneous growth of InGaN alloy difficult. To reduce the piezoelectric polarization and to improve the compositional homogeneity, non-polar and semi-polar plane GaN substrates have been applied to grow In-rich InGaN QWs alternatively [5]. Although this approach will lead to improve the internal quantum efficiency and differential optical gain in the green region, one of the most critical issues is to overcome a large miscibility gap between InN and GaN. Furthermore, the ABLEG technology might be useful for the development of lattice-matched InGaN substrates which reduce the large compressive strain in InGaN QWs [6]. Further material and growth studies should continue to achieve commercial green LDs.

In contrast to InGaN-based LDs, a lifetime of over 500 h has not been realized in ZnCdSe-based LDs because the defects easily propagate and degrade the active region due to strong ionicity that is characteristic of II-VI compounds [7]. However, ZnSe-based alloy containing beryllium has a considerably higher degree of covalency than other II-VI alloys. Therefore, this material system is expected to have longer lifetime [8]. Recently, room-temperature CW operations of BeZnCdSe QW LDs in the green-to-yellow region have been reported [9,10]. The threshold current density has been obtained less than 1 kA/cm^2 for a 10-μm-wide gain-guided LD lasing at 543 nm. This value is 5 times as low as the InGaN-based LD lasing at 534 nm with similar device structure [4]. Therefore, BeZnSe-based material is advantageous for realizing green LDs with high wall-plug efficiency. On the other hand, the BeZnCdSe QW LD structure involves three kinds of quaternary alloy layers such as BeZnMgSe n-cladding layer, BeZnCdSe active layer and BeZnMgSe/ZnSe short-period superlattice p-cladding layer. Conventional elemental source MBE method requires a careful control of the beam fluxes to grow these quaternary alloys. Since the CSMBE that I described in the present dissertation is able to reduce the number of source materials and to stabilize the VI/II beam flux ratio around unity, the application of the CSMBE method might be useful to achieve the uniformity and reproducibility of these quaternary LDs. I believe that the CSMBE method contributes to realize II-VI green LDs in the near future.

References

[1] K. Motoki, T. Okahisa, R. Hirota, S. Nakahata, K. Uematsu, and N. Matsumoto, *J. Cryst. Growth* **305**, 377 (2007).

[2] T. Miyoshi, S. Masui, T. Okada, T. Yanamoto, T. Kozaki, S. Nagahama, and T. Mukai, *Appl. Phys. Express* **2**, 062201 (2009).

[3] A. Avramescu, T. Lermer, J. Muller, C. Eichler, G. Bruederl, M. Sabathil, S. Lutgen, and U. Strauss, *Appl. Phys. Express* **3**, 061003 (2010).

[4] M. Adachi, Y. Yoshizumi, Y. Enya, T. Kyono, T. Sumitomo, S. Tokuyama, S. Takagi, K. Sumiyoshi, N. Saga, T. Ikegami, M. Ueno, K. Katayama, and T. Nakamura, *Appl. Phys. Express* **3**, 121001 (2010).

[5] H. Ohta, S. P. DenBaars, and S. Nakamura, *J. Opt. Soc. Am. B* **27**, 45 (2010).

[6] J. Zhang and N. Tansu, *J. Appl. Phys.* **110**, 113110 (2011).

[7] S. Itoh, K. Nakano, and A. Ishibashi, *J. Cryst. Growth* **214/215**, 1029 (2000).

[8] C. Vèrié, *J. Cryst. Growth* **184/185**, 1061 (1998).

[9] J. Kasai, R. Akimoto, T. Hasama, H. Ishikawa, S. Fujisaki, S. Tanaka, and S. Tsuji, *Appl. Phys. Express* **4**, 082102 (2011).

[10] S. Fujisaki, J. Kasai, R. Akimoto, S. Tanaka, S. Tsuji, T. Hasama, and H. Ishikawa, *Appl. Phys. Express* **5**, 062101 (2012).

List of Publications

Chapter 1

"$Zn_{1-X}Cd_XSe$ (X = 0.2-0.3) single-quantum-well laser diodes without GaAs buffer layers",
Shigeo Hayashi, <u>Ayumu Tsujimura</u>, Shigeo Yoshii, Kazuhiro Ohkawa, and Tsuneo Mitsuyu,
Japanese Journal of Applied Physics, Vol. 31, pp. L1478-L1480 (1992).

"ZnSe-based laser diodes and p-type doping of ZnSe",
Kazuhiro Ohkawa, <u>Ayumu Tsujimura</u>, Shigeo Hayashi, Shigeo Yoshii, and Tsuneo Mitsuyu,
Physica B, Vol. 185, pp. 112-117 (1993).

"Characteristics of ZnCdSe single-quantum-well laser diodes",
<u>Ayumu Tsujimura</u>, Shigeo Yoshii, Shigeo Hayashi, Kazuhiro Ohkawa, Tsuneo Mitsuyu, and
Hidemi Takeishi,
Physica B, Vol. 191, pp. 130-132 (1993).

"Fabrication and characterization of ZnSe-based blue/green laser diodes",
<u>Ayumu Tsujimura</u>, Shigeo Yoshii, Shigeo Hayashi, Kazuhiro Ohkawa, and Tsuneo Mitsuyu,
Proceedings of the Society of Photo-Optical Instrumentation Engineers, Vol. 1985, pp. 468-475
(1993).

"Cavity parameters of ZnCdSe/ZnSe single-quantum-well separate-confinement-heterostructure
laser diodes",
<u>Ayumu Tsujimura</u>, Shigeo Yoshii, Shigeo Hayashi, Kazuhiro Ohkawa, and Tsuneo Mitsuyu,
Japanese Journal of Applied Physics, Vol. 32, pp. L1570-L1572 (1993).

"Optical gain in an inhomogeneously broadened exciton system",
Teruya Ishihara, Yuka Ikemoto, Takeo Goto, <u>Ayumu Tsujimura</u>, Kazuhiro Ohkawa, and Tsuneo
Mitsuyu,
Journal of Luminescence, Vol. 58, pp. 241-243 (1994).

"Electrically pumped CdZnSe/ZnSe blue-green vertical-cavity surface-emitting lasers",
Toshiya Yokogawa, Shigeo Yoshii, <u>Ayumu Tsujimura</u>, Yoichi Sasai, and James Merz,
Japanese Journal of Applied Physics, Vol. 34, pp. L751-L753 (1995).

"Real-index guided blue-green laser diode with small beam astigmatism fabricated using ZnO buried structure",
Toshiya Yokogawa, Satoshi Kamiyama, Shigeo Yoshii, Kazuhiro Ohkawa, Ayumu Tsujimura, and Yoichi Sasai,
Japanese Journal of Applied Physics, Vol. 35, pp. L314-L316 (1996).

"Electron cyclotron resonance plasma etching of ZnSe-based II-VI compounds",
Toshiya Yokogawa, Shigeo Yoshii, Kazuhiro Ohkawa, Ayumu Tsujimura, and Yoichi Sasai,
Blue Laser and Light Emitting Diodes, pp. 441-444 (1996).

Chapter 2
"Complex flow and gas-phase reactions in a horizontal reactor for GaN metalorganic vapor phase epitaxy",
Kenji Harafuji, Yoshiaki Hasegawa, Akihiko Ishibashi, Ayumu Tsujimura, Isao Kidoguchi, Yuzaburoh Ban, and Kiyoshi Ohnaka,
Japanese Journal of Applied Physics, Vol. 39, pp. 6180-6190 (2000).

"Complex flow and gas phase chemical reactions in GaN MOVPE reactor",
Kenji Harafuji, Yoshiaki Hasegawa, Akihiko Ishibashi, Ayumu Tsujimura, Nobuyuki Otsuka, Isao Kidoguchi, and Yuzaburoh Ban,
Institute of Pure and Applied Physics Conference Series, Vol. 1, pp. 101-104 (2000).

"Room-temperature continuous-wave operation of GaInN multiquantum well laser diodes with low indium content",
Ayumu Tsujimura, Yoshiaki Hasegawa, Akihiko Ishibashi, Satoshi Kamiyama, Isao Kidoguchi, Ryoko Miyanaga, Masakatsu Suzuki, Masahiro Kume, Kenji Harafuji, and Yuzaburoh Ban,
Electronics Letters, Vol. 35, pp. 998-999 (1999).

"Room-temperature CW operation of GaInN multiple quantum well laser diodes with optimized indium content",
Ayumu Tsujimura, Akihiko Ishibashi, Yoshiaki Hasegawa, Satoshi Kamiyama, Isao Kidoguchi, Nobuyuki Otsuka, Ryoko Miyanaga, Gaku Sugahara, Masakatsu Suzuki, Masahiro Kume, Kenji Harafuji, and Yuzaburoh Ban,
Physica Status Solidi A, Vol. 176, pp. 53-57 (1999).

"Systematic studies on optical gain spectra in GaInN/GaN-MQWs",

Akihiko Ishibashi, Isao Kidoguchi, <u>Ayumu Tsujimura</u>, Yoshiaki Hasegawa, Yuzaburoh Ban, Tokiko Ohata, Masayuki Watanabe, and Tetsusuke Hayashi,
Journal of Luminescence, Vol. 87-89, pp. 1271-1273 (2000).

"Room temperature 339 nm emission from $Al_{0.13}Ga_{0.87}N/Al_{0.10}Ga_{0.90}N$ double heterostructure light-emitting diode on sapphire substrate",
Nobuyuki Otsuka, <u>Ayumu Tsujimura</u>, Yoshiaki Hasegawa, Gaku Sugahara, Masahiro Kume, and Yuzaburoh Ban,
Japanese Journal of Applied Physics, Vol. 39, pp. L445-L448 (2000).

"339 nm deep-UV emission from $Al_{0.13}Ga_{0.87}N/Al_{0.10}Ga_{0.90}N$ double heterostructure light-emitting diode on sapphire substrate",
Nobuyuki Otsuka, <u>Ayumu Tsujimura</u>, Yoshiaki Hasegawa, Gaku Sugahara, Masahiro Kume, and Yuzaburoh Ban,
Institute of Pure and Applied Physics Conference Series, Vol. 1, pp. 837-840 (2000).

Chapter 3
"Compound-source molecular beam epitaxy for ZnCdSe/ZnSSe/ZnMgSSe laser structure",
Kazuhiro Ohkawa, Shigeo Yoshii, Hidemi Takeishi, <u>Ayumu Tsujimura</u>, Shigeo Hayashi, Takeshi Karasawa, and Tsuneo Mitsuyu,
Japanese Journal of Applied Physics, Vol. 33, pp. L1673-L1675 (1994).

"Compound-source MBE for ZnSe-based lasers",
Kazuhiro Ohkawa, Hidemi Takeishi, Shigeo Hayashi, Shigeo Yoshii, <u>Ayumu Tsujimura</u>, Takeshi Karasawa, and Tsuneo Mitsuyu,
Physica Status Solidi B, Vol. 187, pp. 291-296 (1995).

"Compound source molecular beam epitaxy for II-VI laser structures",
Kazuhiro Ohkawa, <u>Ayumu Tsujimura</u>, Takashi Nishikawa, Shigeo Yoshii, Toshiya Yokogawa, Minoru Kubo, and Yoichi Sasai,
Journal of Crystal Growth, Vol. 159, pp. 632-635 (1996).

"Rapid growth of II-VI laser structures by compound-source molecular beam epitaxy",
<u>Ayumu Tsujimura</u>, Takashi Nishikawa, Kazuhiro Ohkawa, and Yoichi Sasai,
Proceedings of the Society of Photo-Optical Instrumentation Engineers, Vol. 2693, pp. 2-9 (1996).

"Improvement of crystalline quality in GaN films by air-bridged lateral epitaxial growth",
Isao Kidoguchi, Akihiko Ishibashi, Gaku Sugahara, <u>Ayumu Tsujimura</u>, and Yuzaburoh Ban,
Japanese Journal of Applied Physics, Vol. 39, pp. L453-L456 (2000).

"Recombination dynamics in GaN and InGaN/GaN multiple quantum wells on air-bridged lateral epitaxial grown GaN layers",
Tomoaki Izumi, Kenichi Inoue, Yukio Narukawa, Koichi Okamoto, Yoichi Kawakami, Shigeo Fujita, <u>Ayumu Tsujimura</u>, Isao Kidoguchi, and Yuzaburoh Ban,
Institute of Pure and Applied Physics Conference Series, Vol. 1, pp. 599-602 (2000).

"Nonradiative recombination processes of carriers in InGaN/GaN probed by the microscopic transient lens spectroscopy",
Koichi Okamoto, Kenichi Inoue, Yoichi Kawakami, Shigeo Fujita, Masahide Terazima, <u>Ayumu Tsujimura</u>, and Isao Kidoguchi,
Review of Scientific Instruments, Vol. 74, pp. 575-577 (2003).

Other Publications

"Ionic motion and molecular-dynamics simulation of oxyfluoride glass",
Kazuyuki Hirao, <u>Ayumu Tsujimura</u>, Setsuhisa Tanabe, and Naohiro Soga,
Materials Science Forum, Vol. 32, pp. 415-420 (1988).

"Optical-properties of CdS microcrystallite-doped SiO_2 glass thin-films",
Ichiro Tanahashi, <u>Ayumu Tsujimura</u>, Tsuneo Mitsuyu, and Atsushi Nishino,
Japanese Journal of Applied Physics, Vol. 29, pp. 2111-2115 (1990).

"ZnSe-based diode lasers with stripe-geometry fabricated by ion-bombardment",
Shigeo Yoshii, Shigeo Hayashi, <u>Ayumu Tsujimura</u>, Kazuhiro Ohkawa, Tsuneo Mitsuyu, Hidemi Takeishi, Yasuhito Takahashi, and Tadashi Narusawa,
Japanese Journal of Applied Physics, Vol. 32, pp. L1753-L1755 (1993).

"Surface migration of ZnSe during compound-source MBE growth",
Takashi Nishikawa, <u>Ayumu Tsujimura</u>, Tohru Saitoh, Kazuhiro Ohkawa, Minoru Kubo, and Yoichi Sasai,
Blue Laser and Light Emitting Diodes, pp. 70-73 (1996).

"Growth of ZnSe-based compounds on Ge-terminated GaAs surface",

Tohru Saitoh, <u>Ayumu Tsujimura</u>, Takashi Nishikawa, Akio Watakabe, and Yoichi Sasai,

Materials Research Society Symposium proceedings, Vol. 448, pp. 141-146 (1997).

"Suppression of inhomogeneous segregation in graphene growth on epitaxial metal films",

Shigeo Yoshii, Katsuya Nozawa, Kenji Toyoda, Nozomu Matsukawa, Akihiro Odagawa, and <u>Ayumu Tsujimura</u>,

Nano Letters, Vol. 11, pp. 2628-2633 (2011).

"GaN-based light-emitting diodes integrated with zinc oxide photonic crystals",

Kenji Orita, Takahiro Hamada, Akihiro Itoh, Nobuyasu Suzuki, and <u>Ayumu Tsujimura</u>,

IEEE Transaction on Electron Devices, Vol. 59, in press (2012).

Acknowledgements